PUBLISHED BY INSTITUTE OF PHYSICS PUBLISHING AND SISSA
RECEIVED: *March 18, 2008*
REVISED: *May 29, 2008*
ACCEPTED: *July 7, 2008*
PUBLISHED: *August 8, 2008*

Combined performance tests before installation of the ATLAS Semiconductor and Transition Radiation Tracking Detectors

E. Abat,[e,†] A. Abdesselam,[am] T.N. Addy,[s] T.P.A. Åkesson,[ab] P.P. Allport,[y] L. Andricek,[ah] F. Anghinolfi,[i] R. Apsimon,[as] E. Arik,[e,†] M. Arik,[e] N. Austin,[y] O.K. Baker,[bb] E. Banas,[l] A. Bangert,[ah] G. Barbier,[o] S. Baron,[i] A.J. Barr,[am] S. Basiladze,[ag] L.E. Batchelor,[as] R.L. Bates,[q] J.R. Batley,[h] M. Battistin,[i] G.A. Beck,[aa] A. Beddall,[e,1] A.J. Beddall,[e,1] P.J. Bell,[ac] W.H. Bell,[q] A. Belymam,[aa] D.P. Benjamin,[m] J. Bernabeu,[ay] H. Bertelsen,[j] S. Bethke,[ah] A. Bingul,[e,1] A. Bitadze,[i] J.P. Bizzell,[as] J. Blocki,[l] A. Bocci,[m] M. Bochenek,[k] J. Bohm,[ap] V.G. Bondarenko,[af] P. Bonneau,[i] C.N. Booth,[au] O. Brandt,[am] F.M. Brochu,[h] Z. Broklova,[aq] J. Broz,[aq] P.A. Bruckman de Renstrom,[am,3] S. Burdin,[y] C.M. Buttar,[q] M. Capeáns Garrido,[i] L. Cardiel Sas,[i] C. Carpentieri,[n] A.A. Carter,[aa] J.R. Carter,[h] A. Catinaccio,[i] S.A. Cetin,[e,2] M. Chamizo llatas,[o] D.G. Charlton,[d] A. Cheplakov,[q] S. Chouridou,[at] M.L. Chu,[av] V. Cindro,[z] A. Ciocio,[c] J.V. Civera,[ay] A. Clark,[o] A.P. Colijn,[ai] T. Cornelissen,[i] M.J. Costa,[ay] D. Costanzo,[au] J. Cox,[am] P. Cwetanski,[t] W. Dabrowski,[k] J. Dalmau,[aa] M. Dam,[j] K.M. Danielsen,[al] H. Danielsson,[i] S. D'Auria,[q] I. Dawson,[au] P. de Jong,[ai] M.D. Dehchar,[am] B. Demirkoz,[i] P. Dervan,[y] B. Di Girolamo,[i] S. Diez Cornell,[ay] F. Dittus,[i] S.D. Dixon,[au] E. Dobson,[am] O.B. Dogan,[e,†] Z. Dolezal,[aq] B.A. Dolgoshein,[af] M. Donega,[i] M. D'Onofrio,[o] T. Donszelmann,[au] O. Dorholt,[al] J.D. Dowell,[d] Z. Drasal,[aq] N. Dressnandt,[an] C. Driouchi,[j] R. Duxfield,[au] M. Dwuznik,[k] W.L. Ebenstein,[m] S. Eckert,[n] P. Eerola,[ab] U. Egede,[ab] K. Egorov,[t] L.M. Eklund,[i] M. Elsing,[i] R. Ely,[c] V. Eremin,[ag] C. Escobar,[ay] H. Evans,[t] P. Farthouat,[i] D. Fasching,[ba] O.L. Fedin,[ao] L. Feld,[n] D. Ferguson,[ba] P. Ferrari,[i] D. Ferrere,[o] L. Fiorini,[h] J. Fopma,[am] A.J. Fowler,[m] H. Fox,[n] R.S. French,[au] D. Froidevaux,[i] J.A. Frost,[h] J. Fuster,[ay] S. Gadomski,[o,2] P. Gagnon,[t] B.J. Gallop,[as] F.C. Gannaway,[aa] C. Garcia,[ay] J.E. Garcia Navarro,[ay] I.L. Gavrilenko,[ae] C. Gay,[az] N. Ghodbane,[ah] M.D. Gibson,[as] S.M. Gibson,[am] K.G. Gnanvo,[aa] J. Godlewski,[i] T. Göttfert,[ah] S. Gonzalez,[ba] S. Gonzalez-Sevilla,[ay] M.J. Goodrick,[h] A. Gorišek,[z] E. Gornicki,[l] M. Goulette,[i] Y. Grishkevich,[ag] J. Grognuz,[i] J. Grosse-Knetter,[f] C. Haber,[c] R. Härtel,[ah] Z. Hajduk,[l] M. Hance,[an] F.H. Hansen,[j] J.B. Hansen,[j] J.D. Hansen,[j] P.H. Hansen,[j] K. Hara,[aw] A. Harvey Jr.,[s]

**M. Hauschild,[i] C. Hauviller,[i] B.M. Hawes,[am] R.J. Hawkings,[i] H.S. Hayward,[y]
S.J. Haywood,[as] F.E.W. Heinemann,[am] N.P. Hessey,[ai] J.C. Hill,[h] M.C. Hodgkinson,[au]
P. Hodgson,[au] T.I. Hollins,[d] A. Holmes,[am] R. Holt,[as] S. Hou,[av] D.F. Howell,[am]
W. Hulsbergen,[i] T. Huse,[al] Y. Ikegami,[w] Y. Ilyushenka,[v] C. Issever,[am] J.N. Jackson,[y]
V. Jain,[t] K. Jakobs,[n] R.C. Jared,[ba] G. Jarlskog,[ab] P. Jarron,[i] L.G. Johansen,[b]
P. Johansson,[au] M. Jones,[am] T.J. Jones,[y] D. Joos,[n] J. Joseph,[ba] P. Jovanovic,[d]
V.A. Kantserov,[af] J. Kaplon,[i] M. Karagoz Unel,[am] F. Kayumov,[ae] P.T. Keener,[an]
G.D. Kekelidze,[v] N. Kerschen,[au] C. Ketterer,[n] S.H. Kim,[aw] D. Kisielewska,[k]
B. Kisielewski,[l] T. Kittelmann,[j] E.B. Klinkby,[j] P. Kluit,[ai] S. Kluth,[ah] B.R. Ko,[m]
P. Kodys,[aq] T. Koffas,[i] E. Koffeman,[ai] T. Kohriki,[w] T. Kondo,[w] N.V. Kondratieva,[af]
S.P. Konovalov,[ae] S. Koperny,[k] H. Korsmo,[ab] S. Kovalenko,[ao] T.Z. Kowalski,[k]
K. Krüger,[i] V. Kramarenko,[ag] G. Kramberger,[z] M. Kruse,[m] P. Kubik,[aq] L.G. Kudin,[ao]
N. Kundu,[am] C. Lacasta,[ay] V.R. Lacuesta,[ay] W. Lau,[am] A-C. Le Bihan,[i] S.-C. Lee,[av]
R.P. Lefevre,[o] B.C. LeGeyt,[an] K.J.C. Leney,[y] C.G. Lester,[h] Z. Liang,[av] P. Lichard,[i]
W. Liebig,[ai] M. Limper,[ai] A. Lindahl,[j] S.W. Lindsay,[y] A. Lipniacka,[b] G. Llosa Llacer,[ay]
S. Lloyd,[aa] A. Loginov,[bb] C.W. Loh,[az] M. Lozano Fantoba,[ay] S. Lucas,[i] A. Lucotte,[r]
I. Ludwig,[n] J. Ludwig,[n] F. Luehring,[t] L. Luisa,[ax] J. Lynn,[am] M. Maaßen,[n] D. Macina,[o]
R. Mackeprang,[j] A. Macpherson,[a] C.A. Magrath,[ai] P. Majewski,[au] P. Malecki,[l]
V.P. Maleev,[ao] I. Mandić,[z] M. Mandl,[i] M. Mangin-Brinet,[o] S. Marti i Garcia,[ay]
A.J. Martin,[bb] F.F. Martin,[an] T. Maruyama,[aw] R. Mashinistov,[af] A. Mayne,[au]
K.W. McFarlane,[s] S.J. McMahon,[as] T.J. McMahon,[d] J. Meinhardt,[n] B.R. Mellado
Garcia,[ba] C. Menot,[i] I. Messmer,[n] B. Mikulec,[o] M. Mikuž,[z] S. Mima,[aj] M. Minano,[ay]
B. Mindur,[k] V.A. Mitsou,[ay] P. Modesto,[ay] S. Moed,[o] B. Mohn,[b] R.M. Moles Valls,[ay]
J. Morin,[aa] M-C. Morone,[o] S.V. Morozov,[af] J. Morris,[aa] H.G. Moser,[ah]
A. Moszczynski,[l] S.V. Mouraviev,[ae] A. Munar,[an] W.J. Murray,[as] K. Nagai,[aa] Y. Nagai,[aw]
D. Naito,[aj] K. Nakamura,[aw] I. Nakano,[aj] S.Y. Nesterov,[ao] F.M. Newcomer,[an]
R. Nicholson,[au] R.B. Nickerson,[am] T. Niinikoski,[i] N. Nikitin,[ag] R. Nisius,[ah] H. Ogren,[t]
S.H. Oh,[m] M. Olcese,[p] J. Olszowska,[l] M. Orphanides,[au] V. O'Shea,[q] W. Ostrowicz,[l]
B. Ottewell,[am] O. Oye,[b] E. Paganis,[au] M.J. Palmer,[h] M.A. Parker,[h] U. Parzefall,[n]
M.S. Passmore,[i] S. Pataraia,[ah] G. Pellegrini,[ay] H. Pernegger,[i,*]E. Perrin,[o]
V.D. Peshekhonov,[v] T.C. Petersen,[i] R. Petti,[g] A.W. Phillips,[h] P.W. Phillips,[as]
A. Placci,[i] K. Poltorak,[k] A. Poppleton,[i] M.J. Price,[i] K. Prokofiev,[au] O. Røhne,[al]
C. Rembser,[i] P. Reznicek,[aq] R.H. Richter,[ah] A. Robichaud-Veronneau,[o]
D. Robinson,[h] S. Roe,[i] O. Rohne,[al] A. Romaniouk,[af] L.P. Rossi,[p] D. Rousseau,[ak]
G. Ruggiero,[i] K. Runge,[n] Y.F. Ryabov,[ao] A. Salzburger,[u] J. Sanchez,[ay] H. Sandaker,[b]
J. Santander,[ay] V.A. Schegelsky,[ao] D. Scheirich,[aq] J. Schieck,[ah] M.P. Schmidt,[bb,†]
C. Schmitt,[i] E. Sedykh,[ao] D.M. Seliverstov,[ao] A. Sfyrla,[o] T. Shin,[s] A. Shmeleva,[ae]
S. Sivoklokov,[ag] S.Yu. Smirnov,[af] L. Smirnova,[ag] O. Smirnova,[ab] M. Söderberg,[ab]
A.O. Solberg,[b] V.V. Sosnovtsev,[af] L. Sospedra Suay,[ay] H. Spieler,[c] G. Sprachmann,[i]
E. Stanecka,[l] S. Stapnes,[al] J. Stastny,[ap] M. Stodulski,[l] A. Stradling,[ba] B. Stugu,[b]
S. Subramania,[t] S.I. Suchkov,[af] V.V. Sulin,[ae] R.R. Szczygiel,[l] R. Takashima,[x]
R. Tanaka,[aj] G. Tartarelli,[ad] P.K. Teng,[av] S. Terada,[w] V.O. Tikhomirov,[ae] P. Tipton,[bb]**

M. Titov,[n] **K. Toms,**[ag] **A. Tonoyan,**[b] **D.R. Tovey,**[au] **A. Tricoli,**[as] **M. Turala,**[l] **M. Tyndel,**[as] **F. Ukegawa,**[aw] **M. Ullan Comes,**[ay] **Y. Unno,**[w] **V. Vacek,**[ar] **S. Valkar,**[aq] **J.A. Valls Ferrer,**[ay] **E. van der Kraaij,**[ai] **R. VanBerg,**[an] **V.I. Vassilakopoulos,**[s] **L. Vassilieva,**[ae] **T. Vickey,**[ba] **G.H.A. Viehhauser,**[am] **E.G. Villani,**[as] **J.H. Vossebeld,**[y] **T. Vu Anh,**[o] **R. Wall,**[bb] **R.S. Wallny,**[i] **C. Wang,**[m] **C.P. Ward,**[h] **R. Wastie,**[am] **M. Webel,**[n] **M. Weber,**[as] **A.R. Weidberg,**[am] **P.M. Weilhammer,**[i] **C. Weiser,**[n] **P.S. Wells,**[i] **P. Werneke,**[ai] **M.J. White,**[h] **D. Whittington,**[t] **A. Wildauer,**[i] **I. Wilhelm,**[aq] **H.H. Williams,**[an] **J.A. Wilson,**[d] **M.W. Wolter,**[l] **S.L. Wu,**[ba] **A. Zhelezko,**[af] **H.Z. Zhu**[au] **and A. Zsenei**[o]

[a]*Centre for Particle Physics, Department of Physics, University of Alberta,*
Edmonton, AB T6G 2G7, Canada
[b]*University of Bergen, Department for Physics and Technology,*
Allegaten 55, NO - 5007 Bergen, Norway
[c]*Lawrence Berkeley National Laboratory and University of California, Physics Division,*
MS50B-6227, 1 Cyclotron Road, Berkeley, CA 94720, United States of America
[d]*School of Physics and Astronomy, University of Birmingham,*
Edgbaston, Birmingham B15 2TT, United Kingdom
[e]*Faculty of Sciences, Department of Physics, Bogazici University,*
TR - 80815 Bebek-Istanbul, Turkey
[f]*Physikalisches Institut der Universitaet Bonn, Nussallee 12, D - 53115 Bonn, Germany*
[g]*Brookhaven National Laboratory, Physics Department,*
Bldg. 510A, Upton, NY 11973, United States of America
[h]*Cavendish Laboratory, University of Cambridge,*
J J Thomson Avenue, Cambridge CB3 0HE, United Kingdom
[i]*CERN, CH - 1211 Geneva 23, Switzerland, Switzerland*
[j]*Niels Bohr Institute, University of Copenhagen,*
Blegdamsvej 17, DK - 2100 Kobenhavn 0, Denmark
[k]*Faculty of Physics and Applied Computer Science of the AGH-University of Science and*
Technology, (FPACS, AGH-UST), al. Mickiewicza 30, PL-30059 Cracow, Poland
[l]*The Henryk Niewodniczanski Institute of Nuclear Physics, Polish Academy of Sciences,*
ul. Radzikowskiego 152, PL - 31342 Krakow, Poland
[m]*Duke University, Department of Physics, Durham, NC 27708, United States of America*
[n]*Physikalisches Institut, Universitaet Freiburg,*
Hermann-Herder Str. 3, D - 79104 Freiburg i.Br., Germany
[o]*Universite de Geneve, Section de Physique,*
24 rue Ernest Ansermet, CH - 1211 Geneve 4, Switzerland
[p]*INFN Genova and Università di Genova, Dipartimento di Fisica,*
via Dodecaneso 33, IT - 16146 Genova, Italy
[q]*University of Glasgow, Department of Physics and Astronomy,*
UK - Glasgow G12 8QQ, United Kingdom
[r]*Laboratoire de Physique Subatomique et de Cosmologie, CNRS-IN2P3, Universite Joseph*
Fourier, INPG, 53 avenue des Martyrs, FR - 38026 Grenoble Cedex, France
[s]*Hampton University, Department of Physics, Hampton, VA 23668, United States of America*
[t]*Indiana University, Department of Physics, Swain Hall West,*
Room 117, 727 East Third St., Bloomington, IN 47405-7105, United States of America
[u]*Institut fuer Astro- und Teilchenphysik, Technikerstrasse 25, A - 6020 Innsbruck, Austria*

[v]Joint Institute for Nuclear Research, JINR Dubna, RU - 141 980 Moscow, Russia
[w]KEK, High Energy Accelerator Research Organization, 1-1 Oho,
Tsukuba-shi, Ibaraki-ken 305-0801, Japan
[x]Kyoto University of Education, 1 Fukakusa, Fujimori,
fushimi-ku, Kyoto-shi, JP - Kyoto 612-8522, Japan
[y]Oliver Lodge Laboratory, University of Liverpool,
P.O. Box 147, Oxford Street, UK - Liverpool L69 3BX, United Kingdom
[z]Jožef Stefan Institute and Department of Physics, University of Ljubljana,
SI-1001 Ljubljana, Slovenia
[aa]Department of Physics, Queen Mary, University of London,
Mile End Road, UK - London E1 4NS, United Kingdom
[ab]Lunds Universitet, Fysiska Institutionen, Box 118, SE - 221 00 Lund, Sweden
[ac]School of Physics and Astronomy, University of Manchester,
UK - Manchester M13 9PL, United Kingdom
[ad]INFN Milano and Università di Milano, Dipartimento di Fisica,
via Celoria 16, IT - 20133 Milano, Italy
[ae]P.N. Lebedev Institute of Physics, Academy of Sciences,
Leninsky pr. 53, RU - 117 924 Moscow, Russia
[af]Moscow Engineering & Physics Institute (MEPhI),
Kashirskoe Shosse 31, RU - 115409 Moscow, Russia
[ag]Lomonosov Moscow State University, Skobeltsyn Institute of Nuclear Physics,
RU - 119 992 Moscow Lenskie gory 1, Russia
[ah]Max-Planck-Institut für Physik, (Werner-Heisenberg-Institut),
Föhringer Ring 6, 80805 München, Germany
[ai]Nikhef National Institute for Subatomic Physics,
Kruislaan 409, P.O. Box 41882, NL - 1009 DB Amsterdam, Netherlands
[aj]Okayama University, Faculty of Science, Tsushimanaka 3-1-1, Okayama 700-8530, Japan
[ak]LAL, Univ. Paris-Sud, IN2P3/CNRS, Orsay, France
[al]Department of Physics, University of Oslo, Blindern, NO - 0316 Oslo 3, Norway
[am]Department of Physics, Oxford University, Denys Wilkinson Building,
Keble Road, Oxford OX1 3RH, United Kingdom
[an]University of Pennsylvania, Department of Physics & Astronomy, 209 S. 33rd Street,
Philadelphia, PA 19104, United States of America
[ao]Petersburg Nuclear Physics Institute, RU - 188 300 Gatchina, Russia
[ap]Institute of Physics, Academy of Sciences of the Czech Republic,
Na Slovance 2, CZ - 18221 Praha 8, Czech Republic
[aq]Charles University in Prague, Faculty of Mathematics and Physics, Institute of Particle and
Nuclear Physics, V Holesovickach 2, CZ - 18000 Praha 8, Czech Republic
[ar]Czech Technical University in Prague, Zikova 4, CZ - 166 35 Praha 6, Czech Republic
[as]Rutherford Appleton Laboratory, Science and Technology Facilities Council, Harwell Science
and Innovation Campus, Didcot OX11 0QX, United Kingdom
[at]University of California Santa Cruz, Santa Cruz Institute for Particle Physics (SCIPP),
Santa Cruz, CA 95064, United States of America
[au]University of Sheffield, Department of Physics & Astronomy,
Hounsfield Road, UK - Sheffield S3 7RH, United Kingdom
[av]Insitute of Physics, Academia Sinica, TW - Taipei 11529, Taiwan
[aw]University of Tsukuba, Institute of Pure and Applied Sciences,
1-1-1 Tennoudai, Tsukuba-shi, JP - Ibaraki 305-8571, Japan

[ax]*INFN Gruppo Collegato di Udine and Università di Udine, Dipartimento di Fisica,*
via delle Scienze 208, IT - 33100 Udine and
INFN Gruppo Collegato di Udine and ICTP, Strada Costiera 11, IT - 34014 Trieste, Italy
[ay]*Instituto de Física Corpuscular (IFIC), Centro Mixto UVEG-CSIC, Apdo. 22085, ES-46071*
Valencia; Dept. Física At., Mol. y Nuclear, Univ. of Valencia and Instituto de Microelectrónica
de Barcelona (IMB-CNM-CSIC), 08193 Bellaterra, Barcelona, Spain
[az]*University of British Columbia, Dept of Physics,*
6224 Agricultural Road, CA - Vancouver, B.C. V6T 1Z1, Canada
[ba]*University of Wisconsin, Department of Physics, Madison, WI 53706, United States of America*
[bb]*Yale University, Department of Physics,*
PO Box 208121, New Haven CT, 06520-8121 , United States of America
[1]*Currently at Gaziantep University, Turkey*
[2]*Currently at Dogus University, Istanbul*
[3]*also at H. Niewodniczanski Institute of Nuclear Physics PAN, Cracow, Poland*
[†]*Deceased*
E-mail: `heinz.pernegger@cern.ch`

ABSTRACT: The ATLAS (*A Toroidal LHC ApparatuS*) Inner Detector provides charged particle tracking in the centre of the ATLAS experiment at the Large Hadron Collider (LHC). The Inner Detector consists of three subdetectors: the Pixel Detector, the Semiconductor Tracker (SCT), and the Transition Radiation Tracker (TRT). This paper summarizes the tests that were carried out at the final stage of SCT+TRT integration prior to their installation in ATLAS. The combined operation and performance of the SCT and TRT barrel and endcap detectors was investigated through a series of noise tests, and by recording the tracks of cosmic rays. This was a crucial test of hardware and software of the combined tracker detector systems. The results of noise and cross-talk tests on the SCT and TRT in their final assembled configuration, using final readout and supply hardware and software, are reported. The reconstruction and analysis of the recorded cosmic tracks allowed testing of the offline analysis chain and verification of basic tracker performance parameters, such as efficiency and spatial resolution, in combined operation before installation.

KEYWORDS: Particle tracking detectors; Solid state detectors; Transition radiation detectors; Large detector systems for particle and astroparticle physics.

---

[*] Corresponding Author.

Contents

1. Introduction

The ATLAS [1] tracking system, the Inner Detector (ID) [2], consists of three separate subdetectors: the Pixel Detector, the Semiconductor Tracker (SCT), and the Transition Radiation Tracker (TRT). Together they provide tracking of charged particles for momentum measurement as well as primary and secondary vertex reconstruction in a pseudorapidity range of $|\eta| < 2.5$.[1] The left-handed coordinate system is defined with $+x$ pointing horizontally to the LHC centre, $+y$ vertically up, and the z-axis along the LHC beam line. The Pixel Detector and the SCT are based on silicon pixel and strip detectors as active elements. The TRT consists of many layers of gaseous straw tubes which are interleaved with transition radiation foils. The layout of the Inner Detector is shown in figure 1. The figure shows one quadrant of the Inner Detector, in this case one quadrant of the barrel and the top half of Endcap A. Detector elements in the ATLAS experiment are identified as “A” for sections on the $+z$ side of the interaction point and as “C” for sections on the $-z$ side of the the interaction point. Each of the subdetectors consists of a barrel section and two endcap sections. The radial and longitudinal envelopes are summarized in table 1. The entire tracker is surrounded by a solenoid, which provides a magnetic field of 2 T with the field direction parallel to the beam axis. A typical track generates three space points in the pixel detector, traverses eight silicon strip detectors (to give four space points) and 36 straw tubes.

The SCT consists of four concentric barrels for tracking at mid-pseudorapidity and two endcaps which extend tracking to the forward regions. Each endcap is comprised of nine disks surrounding the beam axis. The overall layout parameters are summarised in table 2. The basic building blocks of the SCT are the silicon strip modules for barrels and endcaps [3, 4]. In the barrel the strip direction is approximately parallel to the solenoid field and beam axis; in the endcap the strip direction is radially outwards and perpendicular to the magnetic field direction. The barrel sensors have a constant strip pitch of 80 μm, the endcap modules sensors are wedge-shaped and have variable pitch, which widens towards larger radii. Most modules consist of four silicon sensors [5]: two sensors on each side are daisy-chained to give 768 strips of approximately 12 centimetres in length. A second pair of identical sensors is glued back-to-back with the first pair

---

[1] The pseudorapidity is defined as $\eta = -\ln[\tan(\theta/2)]$, where θ is the relative angle to the $+z$ LHC beam axis.

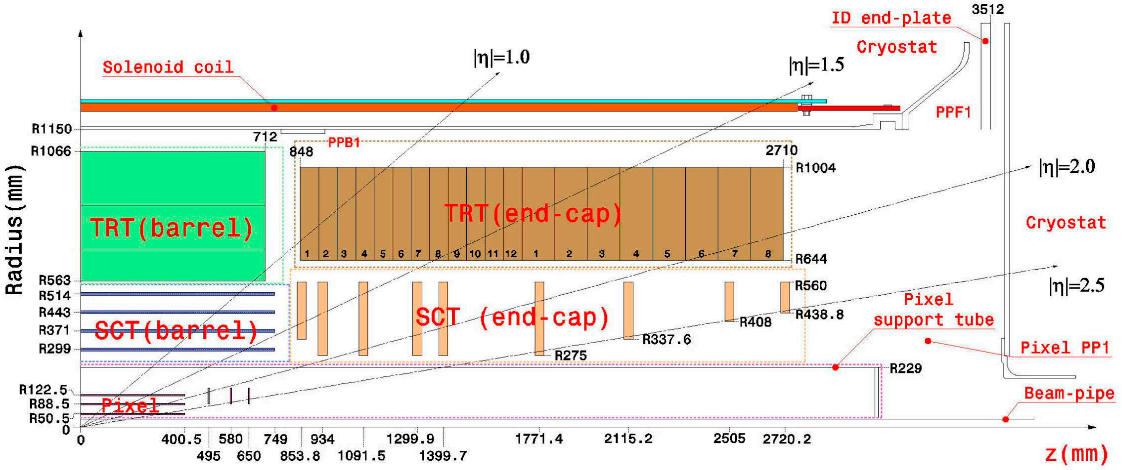

Figure 1. Schematic drawing of one quadrant of the ATLAS Inner Detector.

Table 1. Radial and longitudinal envelopes of the Pixel, SCT and TRT detector sections.

Pixel	$45.5 < r < 242$ mm $\lvert z\rvert < 3092$ mm
SCT Barrel	$255 < r < 549$ mm $\lvert z\rvert < 805$ mm
SCT Endcap	$251 < r < 610$ mm $810 < \lvert z\rvert < 2797$ mm
TRT Barrel	$554 < r < 1082$ mm $\lvert z\rvert < 780$ mm
TRT Endcap	$617 < r < 1106$ mm $827 < \lvert z\rvert < 2744$ mm

at a stereo angle of 40 mrad to provide space points. The inner modules of the endcap disks are shorter and consist of just two sensors with the same stereo angle. The module strips are read out by 12 radiation-hard ABCD3TA frontend readout chips [6]. The readout ASICs are integrated on a multi-layer Kapton-Cu flex circuit and are connected to the silicon strips by wire bonds. The flex circuit is mounted above the silicon sensors in the barrel modules and at the end of the silicon sensors in the endcap modules. The hit information is “binary”: only the channel address of a hit strip is read out optically from each module side to the counting room; no analogue information of the signal is provided during normal running.

The TRT barrel contains up to 73 layers of straws interleaved with polypropylene fibres and the TRT endcap consists of 160 straw planes interleaved with polypropylene foils, which provide transition radiation for electron identification. In the TRT barrel the straw direction is parallel to the beam direction, in the endcap the straw direction is radially outwards. The barrel TRT [7] is divided into three rings of 32 modules each, supported at each end by a space frame, which is the main component of the barrel support structure. Each TRT endcap [8] consists of 20 wheels with eight straw layers per wheel. In the endcap, the straw axis is radial and the anode wire is

Table 2. Layout parameters of the SCT Barrel and Endcap detectors.

	SCT Barrel	SCT Endcaps
silicon area [m^2]	34.4	26.7
number of layers	4 barrels	9 disks/endcap
number of channels [10^6]	3.2	3.0
number of modules	2112	1976
rϕ resolution [μm]	17	17
z resolution [μm]	580	580
pseudorapidity coverage	$\|\eta\| \lesssim 1.2$	$1.2 \lesssim \|\eta\| < 2.5$
radial coverage [mm]	$299 < r < 514$	$300 < r < 520$

Table 3. Layout parameters of the TRT Barrel and Endcap detectors.

	TRT Barrel	TRT Endcaps
number of straw layers	73	2× 160
number of readout channel	105088	2×122880
drift time resolution Xe [μm]	130	130
drift time resolution Ar [μm]	190	190
pseudorapidity coverage	$\|\eta\| \lesssim 1.0$	$1.0 \lesssim \|\eta\| < 2.0$
radial coverage [mm]	$563 < r < 1066$	$644 < r < 1004$

read out at the endcap's outer circumference. Layout parameters of the TRT barrel and endcaps are summarised in table 3. Each straw is based on a 4 mm diameter polyimide drift (straw) tube, the cathode, and a 31 μm diameter tungsten anode wire plated with 0.5-0.7 μm gold. The wire is supported at both straw ends by end-plugs. In the barrel the anode wire is electrically split in two halves by an insulator in the wire middle. In the barrel both ends of the anode wire are directly connected to the frontend electronics and kept at ground potential, while the cathode tube is operated at ≈ -1500 V. In the two endcaps only one end is read out. The TRT will operate in the experiment at a gain of 2.5×10^4 with a gas mixture of 70% Xe + 27% CO_2 + 3% O_2. For the purpose of this test, the TRT was operated with argon instead of xenon as the active gas, due to the high costs of xenon and complexity of recirculation and filtration of the active gas system. The readout electronics [9] will measure the drift time of the primary ionization clusters to the anode wire and, by applying two thresholds, allow the separation of signals originating from electrons.

This paper describes the final tests which were carried out on the assembled SCT and TRT, after they were integrated together to form the SCT+TRT barrel and endcap sections of the ID, and before they were installed in the ATLAS experimental cavern. The combined tests reported here were carried out from April to June 2006 for the Barrel detectors and from October to December 2006 for Endcap C detectors. The tests mark the end of the integration process for the SCT and TRT in the Inner Detector Integration facility at the ATLAS SR1 surface building. The pixel detector followed a separate integration path in SR1, where the pixel barrels and endcaps were integrated with the beam pipe and its support structure. The completed pixel detector was installed in the ATLAS cavern after the mechanical installation of the SCT and TRT in ATLAS was completed.

Due to the integration and installation requirements for the ID, the pixel detector did not participate in the tests reported here.

The goals of the combined tests with the SCT and TRT were to test the noise performance of the combined detectors, to verify the absence of cross-talk, and to obtain experience in combined detector operation in preparation for pit commissioning activities. The performance checks consisted of a series of noise tests with random triggers and calibration-mode noise tests, followed by data taking to record cosmic ray tracks in the SCT and TRT. The detector sections used for the tests were limited by the size of the test system available on the surface integration facility. In the tests approximately one quarter of both the SCT Barrel and Endcap C were powered and read out together with one-eighth of the TRT Barrel and one-sixteenth of the TRT Endcap C. Other sections of the detectors were not cooled, powered, or read out.

The full ATLAS offline software was used to analyze the cosmic ray data. Key parts of the software were tested during the combined operation. These software packages, such as the monitoring, the reconstruction chain, and the calibration and alignment algorithms, will also be used for data taken with colliding beams. The reconstruction and analysis of the recorded tracks allowed us to test the software chain and correct inconsistencies (e.g., in the detector description). The offline software was also used to check if the performance of the detector (efficiencies and resolutions) are within specifications.

2. Experimental setup

The tests described in this note were performed at the CERN Inner Detector Integration facility at the ATLAS SR1 with the fully assembled SCT and TRT barrel and with one of the two SCT and TRT endcaps. Specifically, the endcap which is now installed on “Side C” of the ATLAS experiment was used.

Each SCT and TRT barrel or endcap was first assembled independently. For the SCT this process was carried out at different assembly sites, while for the TRT the entire process was undertaken at SR1. The completed SCT barrel and endcaps were then inserted into the corresponding TRT subdetectors.

For the insertion of the SCT into the TRT, the SCT was supported on a cantilever frame as shown in the foreground of figure 2 (left) for the barrel. Meanwhile the completed TRT was transferred into the final support and lifting frame, which was also used for the transport to the pit, and which can be seen in the background of figure 2 (left). The TRT was then guided on rails over the SCT (shown in figure 2 (right) for the endcap). During the movement the alignment and concentricity of the subdetectors were repeatedly verified, as was the electrical isolation of the SCT, TRT and support tooling. The clearance between the barrel portions of the SCT and the TRT is typically 1 mm. After the insertion was completed, the SCT was positioned on rails inside the TRT with a mechanical precision of $\approx$250 μm and a survey was carried out. The mechanical survey of the SCT and TRT barrel shows a horizontal displacement of Δx=0.3 mm and a rotation around the y-axis of 0.221 mrad of the SCT with respect to the TRT barrel.

For the final tests on the completed barrel, two opposite sectors of the SCT and TRT were cabled and tested. The connected sectors comprised 1/8 of the TRT and 468 modules, equivalent to approximately one quarter, of the SCT barrel as shown on the right side of figure 3. For Endcap C

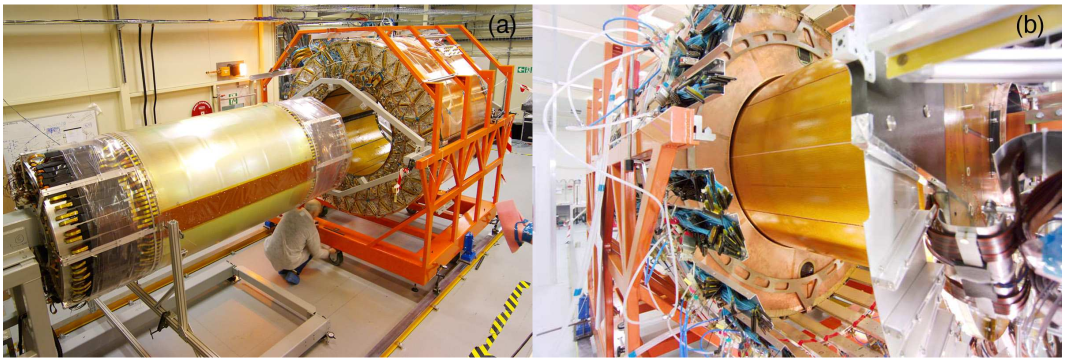

Figure 2. Insertion of the SCT barrel into the TRT barrel (left) prior to their combined test in SR1. The right photograph shows the insertion of the SCT endcap into the TRT endcap before the SCT+TRT endcap were tested together.

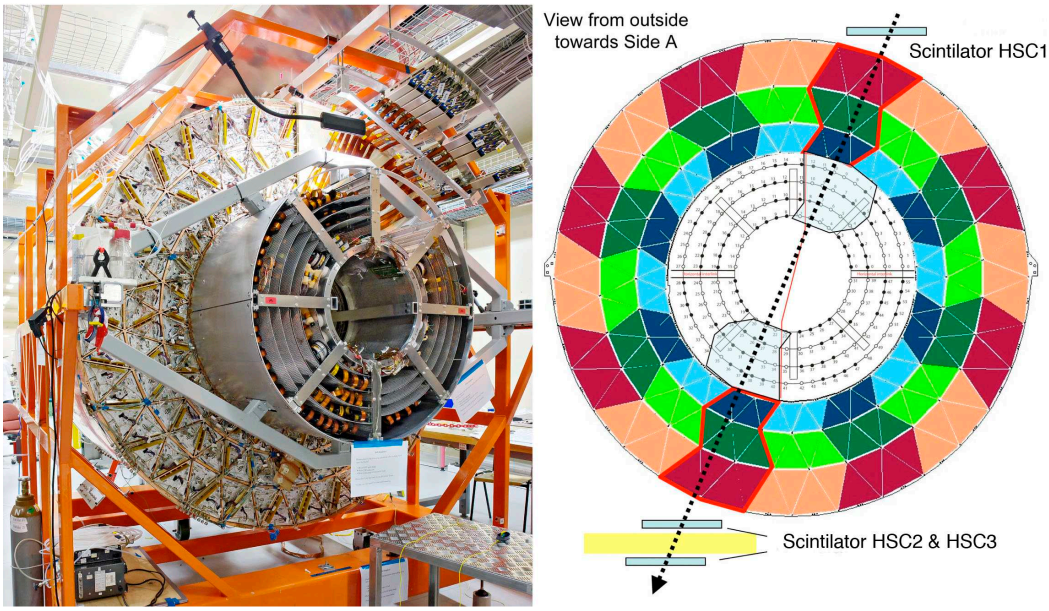

Figure 3. Left: photo of the ID Barrel setup for the cosmic test; right: the configuration of module groups chosen for this test.

one quadrant of the SCT, consisting of 247 endcap modules, and 1/16 of the TRT Endcap Wheels A and B were connected to the supply and readout system. “Wheel A” denotes the twelve 8-plane straw wheels closest to the barrel (labelled 1 to 12 in figure 1) and “Wheel B” the eight 8-plane straw wheels farthest from the barrel (labelled 1 to 8 in figure 1). Care was taken to emulate the final setup in the pit, in particular for the service routing and detector grounding. Detectors and support structures were electrically isolated from each other. The detector grounds were connected together in a star-point configuration similar to the one in the final configuration.

After the completion of the combined test of the SCT+TRT barrel detectors, they were installed as one package in the ATLAS cavern in August 2006. The SCT+TRT sections of endcap A were installed in the ATLAS cavern in May 2007 and the SCT+TRT sections of endcap C in June 2007.

2.1 Trigger

The following scintillator setups were implemented to record cosmic rays in the active barrel and endcap portions of the SCT and TRT.

2.1.1 Barrel trigger setup

For the barrel setup, cosmic rays were triggered using three layers of Eljen EJ-200 scintillators[2] of dimension 144 cm × 40 cm × 2.5 cm, as shown in figure 4.

The three scintillators were arranged so that a wide angular distribution of the cosmic ray muons would hit the scintillators as well as the instrumented sectors of the TRT and SCT. One of the scintillators was placed above the detector (HSC1), one of them below (HSC2), and another under the concrete floor (HSC3). The cosmic trigger was formed by looking for coincident hits in the top and middle layers. The output of the third scintillator was also recorded to allow for an optional offline energy cutoff of around 170 MeV (corresponding to a 15 cm thickness of concrete) by requiring an additional coincidence with the third scintillator.

The time of an output pulse emerging from one of the two Hamamatsu R2150 phototubes attached to both ends of the scintillators may differ from the other by a few nanoseconds depending on where the particle intersects the scintillator. Therefore, a LeCroy Model 624 Octal Meantimer was used to equalize the photon transit time by providing an output pulse at a fixed time, independent of where the impact occurred. In this way a 0.5 ns time resolution was achieved in the time-of-flight measurement. The scintillator coincidence rate, which was used to trigger the detector readout, was 2.4 Hz. A total of 450000 events were recorded for the barrel test.

Figure 5 shows that the time-of-flight is independent of the energy of the cosmic muon for energies above 600 MeV. The time-of-flight from the top scintillator (HSC1) to the bottom scintillator (HSC3) was used to cut away noise events (i.e., fake triggers) which can be recognized by an unphysical value for the computed time-of-flight. Other than in the rejection of noise triggers, the scintillator data were not used to select specific event samples. No momentum selection, based on scintillator data, was carried out during the offline analysis.

In addition, the charge deposited can be measured. This is important for ensuring that the event has been triggered by a charged particle. The charge resolution is on the order of 100 fC.

2.1.2 Endcap trigger setup

For the endcap setup, two of the three scintillators from the barrel setup were reused and placed on top of the endcap while a third scintillator of size 50 cm × 60 cm was placed vertically in front of the endcap as shown in figure 6. This layout balances the competing demands of selecting long tracks in the endcaps and having an acceptable rate of tracks. Information about the time-of-flight was not available in this setup. The trigger rate for coincidence of the endcap trigger scintillators was 0.7 Hz. Due to the low scintillator trigger rate additional data samples were recorded using TRT endcap frontend signals to enhance the track sample in the SCT for SCT studies at a trigger rate of 25 Hz. The scintillator trigger resulted in a rate of reconstructed tracks of 0.17 tracks/s, the TRT frontend trigger in a rate of 1.38 tracks/s. A total of 2.5 million events were recorded for the endcap test.

---

[2] Eljen Technology, PO Box 870, 300 Crane Street, Sweetwater TX 79556, USA

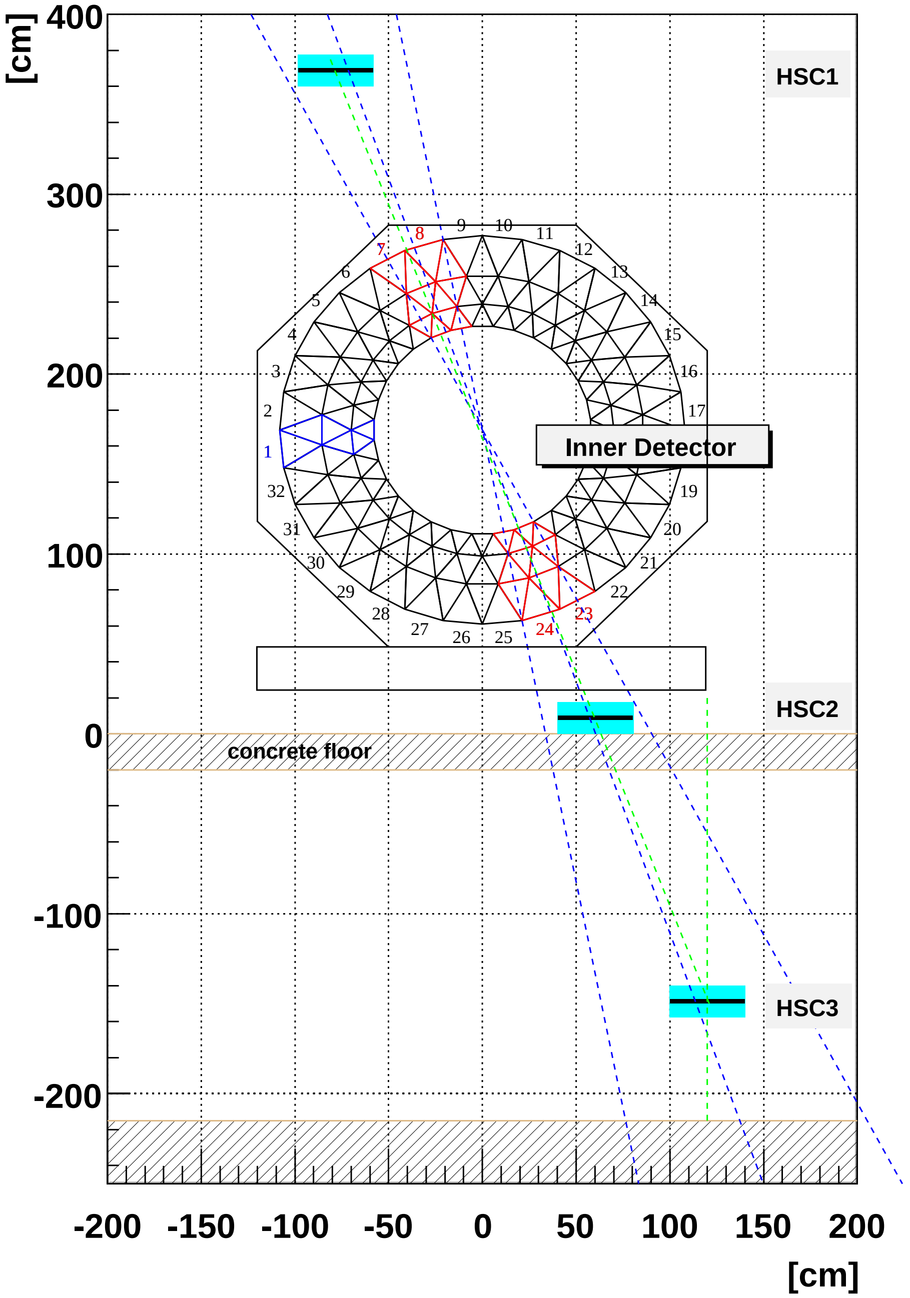

Figure 4. The boxes marked as “HSC1”, “HSC2”, “HSC3”, one above the Inner Detector and two below, represent the scintillators used for trigging on cosmic rays in the barrel region. Each scintillator was read out with two photomultipliers, one at each end. The hatched box just below HSC2 represents the concrete floor.

3. Detector readout and event reconstruction

3.1 Detector control system

The Detector Control System (DCS) serves two purposes during detector operation. It allows

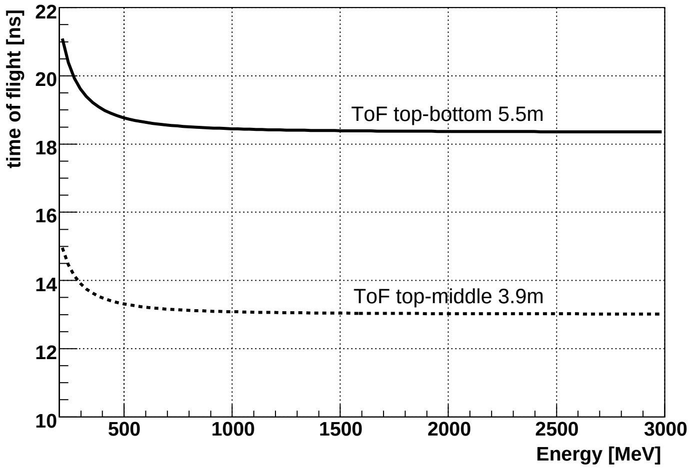

Figure 5. Theoretical time-of-flight for a muon from top to middle (dashed line) and bottom (solid line) scintillators.

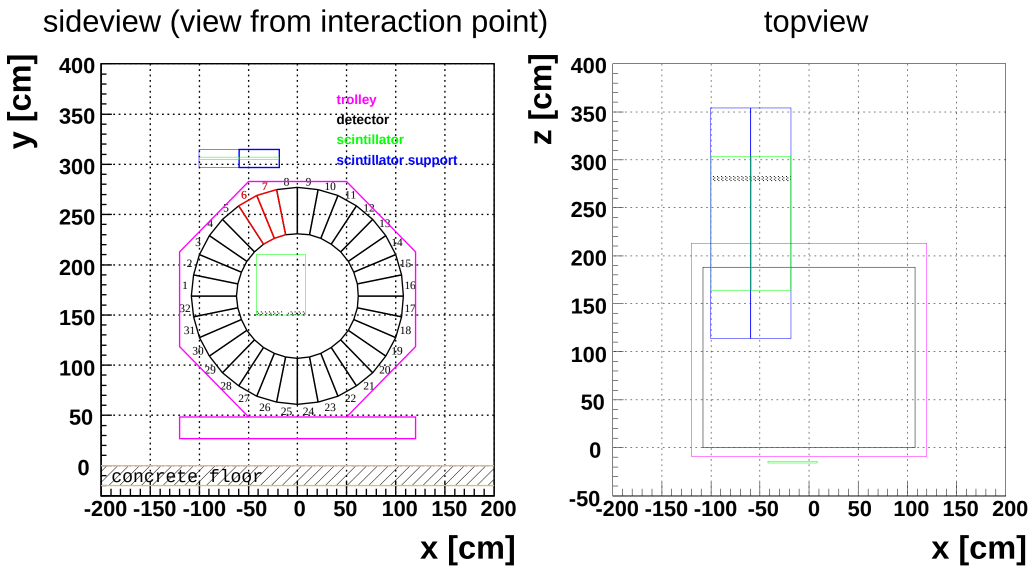

Figure 6. The green boxes show the top two scintillators with their corresponding support structures (blue) and the vertical scintillator.

control of the powering of the detector and ensures detector safety by monitoring several parameters and taking action based on their values.

3.1.1 SCT DCS

For the SCT tests in SR1, the DCS system was divided into two main parts: the Power Supply Control and the Environmental Monitoring System.

The largest part of the SCT DCS [12] was the power supply system. Each detector module was powered and controlled by two independent and floating low voltage (LV) power supplies. These were used to power the readout chips and the opto-communication circuits. The high voltage (HV) supplies provided the depletion voltage for the sensors. Figure 7 shows the digital and analogue

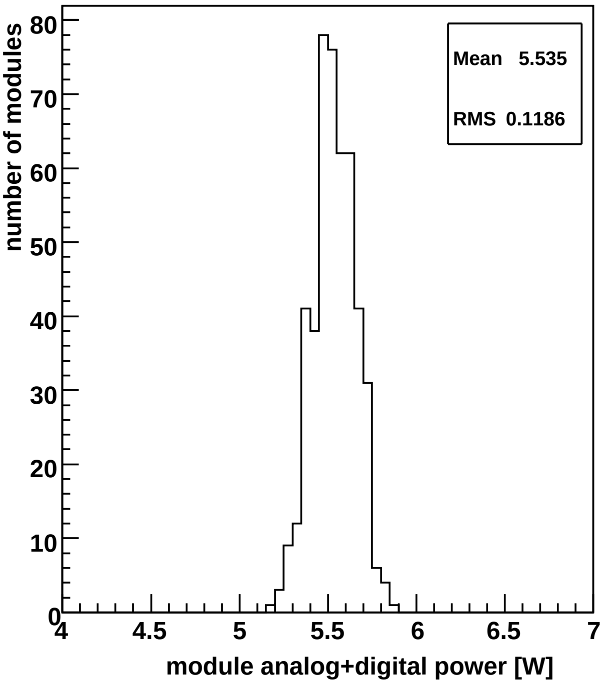

Figure 7. Electrical power consumption for the active SCT barrel modules during the combined test.

power consumption for the barrel SCT modules. In addition, the LV supply took care of powering and reading out Negative Thermal Coefficient (NTC) temperature sensors located on the hybrid (two sensors, one on each side of the module, for the barrel and one sensor per module for the endcap). These parameters were read out using a CAN bus [13] by a DCS computer running a PVSS project [14]. The Power Supply DCS also used a Distribution Information Management (DIM) [15] system to allow a direct communication between DAQ and DCS systems (DDC). The DAQ could then operate the power supply system and receive information about the actual state of the system. The full data set available from the DCS systems was recorded and a subset of those data, the one related to module operation, were transfered into the ATLAS database system used by DCS (Oracle and COOL). From there the module-operation related data (e.g. voltages, currents, temperatures) is available for checks of the detector operation status and for offline analysis.

The second part of the SCT DCS was the environmental monitoring system. This measured the value of temperature and humidity sensors distributed in the detector. Three types of temperatures were measured with NTC-type temperature sensors, which are permanently mounted on the detector. Two sensors are located at the exhaust of each cooling pipe of the whole detector. Other sensors are attached to the mechanical structure of the detector to monitor the possible deformation due to temperature changes. Finally, temperature sensors are located next to the Frequency Scanning Interferometer (FSI) [16] on-detector components to measure the gas temperature inside of the detector volume. In addition, radiation-hard Xeritron[3] humidity probes are installed on the barrel and endcaps. Combined with a temperature measurement, they are used to calculate the dew point inside of the thermal enclosure. Condensation on the silicon modules was avoided by actively

---

[3] XN1018 Xeritron series, Hygrometrix Inc. Alpine CA 91903, USA.

monitoring the dewpoint of the SCT environmental gas. We used dry-air as environmental gas during the tests reported here, which was supplied through filtration and de-humidification stages with a dewpoint of about -45 °C.[4] The gas was supplied at room temperature (typically around 19 °C), without pre-cooling and at a flow rate of 30 l/min to the detector. The environmental gas is then distributed uniformly inside the active detector volume by ducts or pipes in the vicinity of the (cold) cooling pipes.

The SCT detector was cooled using an evaporative C_3F_8 cooling cycle [17]. The cooling plant was constructed as a prototype system for the final Pixel and SCT cooling system and used during the macro-assembly and integration of the SCT detector in SR1. For the combined test described here, a total of twelve cooling loops were operated simultaneously in the barrel and nine cooling loops in the endcap. The cooling temperature was higher than the final operation cooling temperature (approximately -25 °C) due to the constraints of the environmental dewpoint near the pipes leading from the detector to the cooling regulation rack in the test setup. Cooling pipe temperatures were approximately +12 °C during the barrel tests and approximately +5 °C during the endcap tests. This results in hybrid temperatures of +24 °C to +28 °C. The temperature sensors, which measure these hybrid temperatures, are mounted close to the hottest point of the module. Sensor temperatures are not directly measured, however FEA simulations and measurements suggest that the hottest point on the unirradiated sensors is approximately 6 °C warmer than the cooling temperature for barrel modules [3] and approximately 8 °C warmer than the cooling temperature for endcap modules [4].

The cooling pipe temperatures, as measured by the environmental system, are also used to trigger the interlock system. The main purpose of the interlock system is to protect the silicon detector modules from overheating if the cooling stops. The system is fully implemented in hardware for maximum reliability. An Interlock Box (IBOX) [18] compares the temperature sensor value to a threshold and sends a signal to the appropriate power supply crate to turn it off in less than one second if the threshold is reached. The mapping of the sensors to the power supply crates is made through an interlock matrix, which maps the temperature sensor to the relevant power supply channels.

Since the beginning of the macro-assembly activities, the DCS system has evolved to cope with changing requirements from the different detector testing phases. The system showed good performance and stability and, in cases, protected the detector during failures of supply systems or operational errors. The final SCT DCS also has a Finite State Machine (FSM) which handles the transmission of state information, adds high level safety checks, and oversees the passing of commands to the hardware from the ATLAS central DCS.

3.1.2 TRT DCS

The DCS of the TRT was set up to control and monitor the hardware components that are essential for correct operation of the detector. There are five basic groups of such components:

- Low Voltage power supplies - to feed the frontend and active patch panels electronics
- High Voltage power supplies - to bias the gaseous detectors

---

[4] During operation in the experiment the SCT will be supplied with nitrogen as environmental gas.

- Temperature sensor - for checks of the FE electronics operation temperature
- Cooling system - C_6F_{14} cooling of the FE electronics
- Active gas system

Only the temperature sensors mounted on the detector parts (cooling plates, electronics boards, modules shells) were of the final type. All other systems consisted of the hardware available at the time. While the interfaces to the hardware were specifically built for the SR1 setup, the higher layers of control software were prototypes of the final ATLAS system, hence the setup was used to qualify the different procedures and actions of the final system. The TRT was operated during the tests in SR1 with an active gas mix of $Ar:CO_2$ in the ratio of 70%:30%.

Three PL500 power crates manufactured by Wiener Plein & Baus Electronics[5] were used to provide low voltage to the TRT. They contained eight channels each allowing us to create an LV partitioning similar to the final architecture planned for the experiment. The control of the crates was done using the CAN bus as the physical layer and using the OPC server as a higher-level control. The output of the power supplies (analogue positive/negative and digital voltages) fed the LV patch panels (LVPP), which in turn distributed voltage lines to the individual electronic boards on the detector. The LVPP boards are controlled remotely via another CANbus branch and the CANOpen OPC protocol. The LVPP boards contain a standard ATLAS control module, ELMB [20], which serves as the measuring instrument for currents and voltages in individual lines with its analogue segment, and as the communication driver, allowing the setting of the DACs for voltage adjustment and a way to switch the regulators on or off via digital ports.

A CAEN 1527 system along with four 1833 boards[6] was used to provide high voltage to the TRT straws. The software was built with the use of the CERN JCOP FrameWork toolkits [19]. The setup allowed for the control and monitoring of voltages and currents and was also capable of performing predefined actions on HV channels or modules consisting of several consecutive operations. For operation in SR1 we used a typical HV of -1500 V applied to the straw tubes.

The TRT detector is equipped with several temperature sensors that monitored sensitive points of the apparatus. The temperatures of frontend electronics boards are monitored by NTC sensors, while cooling elements and detector mechanics are monitored with PT1000 probes. The signals are fed to the ELMB module, which is read out via the CANbus and CANOpen OPC server. Limits are set on the temperature values, with the system configured to give a warning after crossing the first threshold and to switch the low voltage power supplies off when a dangerous temperature limit is reached.

For the TRT setup in SR1 the cooling unit was controlled via the local programmable logic controller (PLC) and the control DCS software had only monitoring functions. However the status of the unit was coupled to the low voltage system through a hardware-based interlock system, allowing the powering down of the detector in the case of a cooling failure. For the barrel a temporary interlock system using several NTC temperature sensors, which monitored on-barrel electronic temperatures, was connected to special comparator logic which switches the power supplies off when the temperature threshold is exceeded.

---

[5] W-IE-NE-R, Plein & Baus GmbH, Müllersbaum 20, D - 51399 Burscheid, Germany

[6] CAEN S.p.A., Via Vetraia, 11, I-55049 Viareggio (LU), Italy

3.2 Data acquisition

3.2.1 SCT DAQ

Control, readout, and online calibration of the SCT were performed using the SctRodDaq [21], which was developed within the ATLAS TDAQ software framework [23]. Multiple c++ and Java applications can communicate across multiple processors using CORBA.[7] The hardware part of the SctRodDaq system in SR1 was comprised of several PCs, a 6U VME crate for Trigger Timing Control (TTC) specific modules, and a 9U VME64x crate housing 12 Readout Driver Modules (RODs) [25], 12 Back of Crate cards (BOCs), and a Timing Interface Module (TIM). The RODs are used for the main control and data handling, whereas the BOCs provide the ROD interface to the frontend modules and to the rest of the ATLAS DAQ chain. The TIM provides the interface to the ATLAS TTC system. Each ROD/BOC pair is connected optically to up to 48 SCT modules, and to a single Readout Supervisor (ROS) PC.

The SCT uses a binary readout architecture based on the ABCD3TA chip [6] whereby a hit is registered if a pulse height from the silicon microstrip detector channel exceeds a preset threshold. SctRodDaq operates in two modes. For calibration of the SCT modules, triggers are generated internally by the RODs or by the TIM and sent to the modules. Known test charges are injected by the frontend chips and the occupancy (the fraction of triggered events for which the pulse height exceeds the threshold) is determined as a function of threshold. The resulting threshold scan data are extracted from the RODs via VME readout and analysed online to generate an optimised calibration, which is then applied for cosmics or physics data taking. For running in physics or cosmics mode, the triggers (originating from collisions or cosmics) are sent to the frontend chips via the TTC system. Hit information arising from noise or cosmics are channeled event-by-event to the ROS for subsequent event building. The data are then analysed offline or online for track reconstruction and tracking efficiency. For the tests presented here, we recorded for each hit the information in the triggered bunch-crossing cycle plus the hit information of the bunch-crossing cycle prior to and immediately after the trigger bunch crossing cycle. This “hit pattern” is then presented in its binary form as e.g., “011” for a signal recorded in the trigger time bin (second bit), none in its preceding clock cycle, and a signal above threshold in the cycle after the triggered time bin.

3.2.2 TRT DAQ

The TRT data acquisition system was composed of two software tools: XTRT [24] for calibration and parameter tuning, and the TRT DAQ for the collection and storage of data generated by an external trigger source. Each tool was responsible for coordinating the actions of the frontend electronics, which are mounted at the end of the straw chambers, and the “backend” electronics, prototypes of two different 9U VME modules located off-detector. A series of patch panels mediated the communcation between the frontend and the backend. They provided signal compensation and replication for signals going to the frontend, and further compensation for signals returning to the backend.

The TRT makes use of two custom ASICs on the frontend electronics to detect both minimum ionizing particles (low threshold) as well as transition radiation (high threshold). The analogue

---

[7] Common Object Request Broker Architecture define by the Object Management Group enables software components written in multiple computer languages and running on multiple computers to work together.

ASDBLR chip [26] provides a ternary output corresponding to three states: below threshold, low threshold crossed, low and high threshold crossed. The analogue output currents are sent to a companion DTMROC chip [27], which digitizes the analogue data and, upon receipt of a trigger, returns the data for 16 straws to a ROD backend module.

The XTRT program was used extensively for testing of prototype and production frontend electronics. The tests included scans of timing and threshold parameters, the injection of test pulses to test the response of the frontend to known signal shapes and amplitudes, and the use of an "accumulate mode" in the digitizing chips to test the integration of the electronics with the gas and high voltage systems. The results of all tests, as well as a record of the hardware used in each test, were stored in a MySQL database, which provided read-only access to a web interface for easy browsing of the results.

While XTRT was designed to track the response of the hardware as various parameters were scanned, the TRT DAQ was designed to take data at a fixed point in parameter space. The TRT DAQ is a collection of c++ libraries and database objects, which are used to initialize and run an instance of the ATLAS TDAQ software framework [23]. The TRT DAQ is configured via a database, which contains instructions for all of the necessary ATLAS DAQ infrastructure as well as specific parameters used for running the TRT back- and frontend electronics. The TRT specific parameters were extracted from the database which held the results of the XTRT scans.

Because the TRT DAQ was an instance of the ATLAS TDAQ framework, it scaled easily to cope with the amount of readout hardware available. For the barrel and endcap tests, the system was composed of two 9U VME crates for TRT backend hardware, one 6U VME crate for ATLAS TTC hardware, a PC dedicated for event building and storage, and a PC used to control the TDAQ infrastructure.

2008 JINST 3 P08003

3.2.3 Trigger and synchronization

The trigger system used for both noise tests and cosmic ray tests was based on the ATLAS TTC system hardware. This hardware facilitates the distribution of clock, reset, and trigger signals to one or more subsystems via fibreoptic links between a TTC Crate and a Readout Driver Crate. Each TTC "partition" contains hardware sufficient to trigger some subset of a single subsystem. Different partitions can be daisy-chained together by connecting the master components of each partition, called the Local Trigger Processors. In the SR1 system tests, there were separate partitions for the TRT and for the SCT. In this case, one partition acted as the master, and the other as the slave. The distinction between master and slave was made in software, so the same cable connections could be used in either configuration.

To test systematic noise effects introduced by either subsystem on the other, two different noise triggers were used. The first was a trigger at a fixed frequency (variable from a fraction of a Hz to several MHz), while the second was a pseudo-random pulser, the average frequency of which was tunable between several Hz and several kHz. Neither trigger was synchronous with the 40 MHz clock used by the subsystems, so a synchronization of the trigger signal was performed in the TTC crate. For noise data, the phase of the trigger with respect to the clock was not monitored.

For tests with cosmic rays, the trigger was generated in one of two different ways. For the barrel tests, the scintillators described in section 2 provided a coincidence trigger designed to illuminate the active readout regions. For the endcap, in addition to the scintillator trigger, the TRT self-trigger functionality was exploited. In this mode, the digital chips on the TRT frontend provided a trigger if any of their associated straw channels went over threshold. These triggers were collected by the TRT-TTC module, and used to create a multiplicity based trigger for the two subsystems. The efficiency and fake rates were almost entirely determined by the selection of frontend thresholds, so that it was possible to obtain a reasonably pure and efficient trigger.

In the case of cosmic ray triggers, unlike the case of noise triggers, the phase of the asynchronous trigger signal with respect to the clock plays a crucial role. The trigger must be synchronized with the 40 MHz clock before it reaches the frontend electronics, so a measurement of this phase must be made before the data are collected. To determine this phase, two methods were employed. In the first, the TRT-TTC module was given a trigger delay measurement (TDM) module, which received an asynchronous trigger signal and stored the resulting measurement in the TRT event fragment written to disk. In the second method, a TDC was used to measure the phase of the scintillator trigger, the results of which were stored in an independent event fragment. Both methods were limited to scintillator triggers; no phase measurement was possible for the TRT self-trigger.

3.3 Simulation and reconstruction software

The offline software infrastructure developed in ATLAS to simulate and reconstruct the LHC data was used for the first data taken by the Inner Detector in SR1. Thanks to the very flexible underlying ATHENA [28] framework, the necessary adaptations in the algorithms could be easily integrated. These adaptations were required in order to take into account the fact that particles are not produced in the middle of the detector and that they are not synchronized with the readout clock, but randomly generated.

3.3.1 Detector description

The detector description is a common service that provides the geometry (including alignment corrections) and material information. It is used in the simulation to create the Geant4 [29, 30] geometry and to emulate the response of the electronics. In addition, it is used by the different steps of the reconstruction. A specific detector description was created for the SR1 setup with no magnetic field.

For track fitting purposes, a simplified version of the geometry was created from the same service. This tracking geometry, which is the result of simplifying the material description into layers and volumes, allows for fast navigation. However, no direct measurement of the momentum can be done from the SR1 reconstructed tracks due to the lack of a magnetic field and therefore material effects cannot be taken into account during tracking, leading to an underestimation of the uncertainty of the measured track quantities.

3.3.2 Simulation

A simulation of cosmic ray events for the detectors as set up in SR1 was provided in order to first test the full reconstruction chain before data taking started and later to compare the data with simulated events.

The data flow of the simulation (figure 8) contained the following steps:

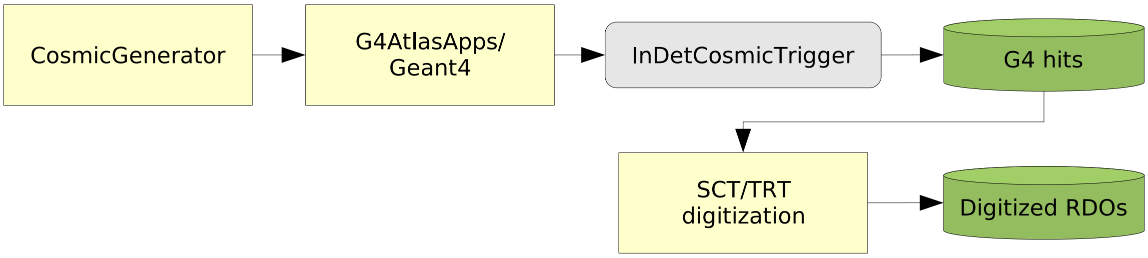

Figure 8. Cosmic ray simulation data flow.

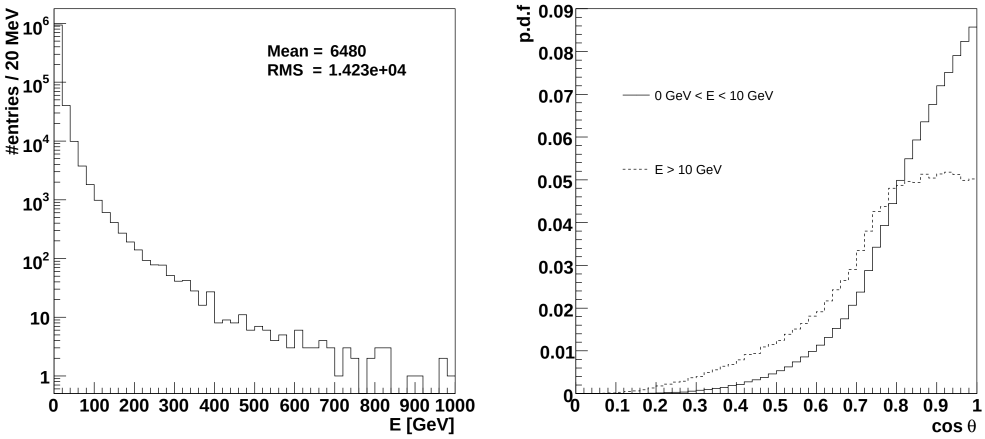

Figure 9. Energy and angular distributions of the generated muons.

- **Generator**

  A cosmic Monte Carlo generator was used for generating the incoming muons from cosmic ray events in the simulation. It generates single muons with a position and momentum vector from a user-defined spatial horizontal window. The generated muons have energy and polar-angle θ distributed as shown in figure 9. These are based on measurements of the differential vertical muon cross section [31] and analytical calculation ([32] and references therein) extrapolated to low muon energy. The cosmic generator used for this simulation generates single muons but no showers. No corrections were made for the test location on the surface (elevation, latitude, or building roof). The concrete floor below the detector and above trigger scintillator HSC3 was however included in the simulation.

  The generator was set up to generate muons in a window right above the upper scintillator. To improve simulation speed, their direction was restricted so that they would go through the acceptance of the middle or vertical scintillator, for the respective barrel and endcap setups.

- **Simulation**

  The simulation toolkit Geant4 was used in order to simulate the passage of particles through the detector. Geant4 receives the muon position and momentum vectors from the generator and propagates the particle through a very detailed three-dimensional model of the detector, simulating the energy depositions throughout the detector.

- **Trigger**

  A trigger algorithm was used to select those events which generated hits in both upper and middle scintillators (Barrel setup) or vertical scintillator (Endcap setup), respectively, and only those were written to disk.

- **Digitization**

  The digitization converts the simulated deposited energy to the Raw Data Objects (RDOs), which form the input objects to the reconstruction. It simulates effects such as the finite readout resolution of the detectors and the electronic response. During this process the detector elements which were not read out were masked.

  The SCT digitization algorithm is described in ref. [33]. The algorithm loops over the deposited energy in the detector elements and determines if the collected charge would pass the comparator threshold of 1 fC. During the digitization a uniform noise level of 1500 electrons ENC is added to the simulated signal data of all individual channels. It is also time-aware, in the sense that it integrates charge collection over one bunch crossing. Charges deposited after this are not taken into account for the hit decision procedure.

  The SCT digitization is interfaced to the conditions database for determining which modules, chips, and channels should be enabled for a given run number. Measured detector characteristics like channel specific noise and gain as well as configuration parameters such as applied bias voltages and thresholds are also available from the conditions database, but those were not used in this test.

  Concerning the TRT, the digitization process simulates the drift of charges from ionization of the gas to the central wire, and records the drift time and time over threshold. It also adds the additional time introduced by the propagation from the impact point on the straw to the readout at the end of the straw. In addition, it simulates noise modeled from ATLAS Combined Test Beam (CTB) data [34]. To account for the use of argon instead of xenon in the combined tests, drift times were reduced by a factor of two-thirds and the detection of high-signal hits was disabled.

  The default ATLAS TRT digitization assumes that the particles originate from the interaction point, and for each straw there is a time offset T_0 taking this into account. However, in cosmic ray events, the particles enter the top of TRT and leave through the bottom, so a different timing scheme was applied.

3.3.3 Reconstruction

A diagram representing the data flow of the reconstruction chain is shown in figure 10. It is designed to work with both simulated and real data provided that for the real case the data given out by the detectors are decoded and the corresponding RDOs created. The different steps of the chain are described below in more detail. The inner detector and tracking Event Data Model classes are described in more detail in [35] and [36].

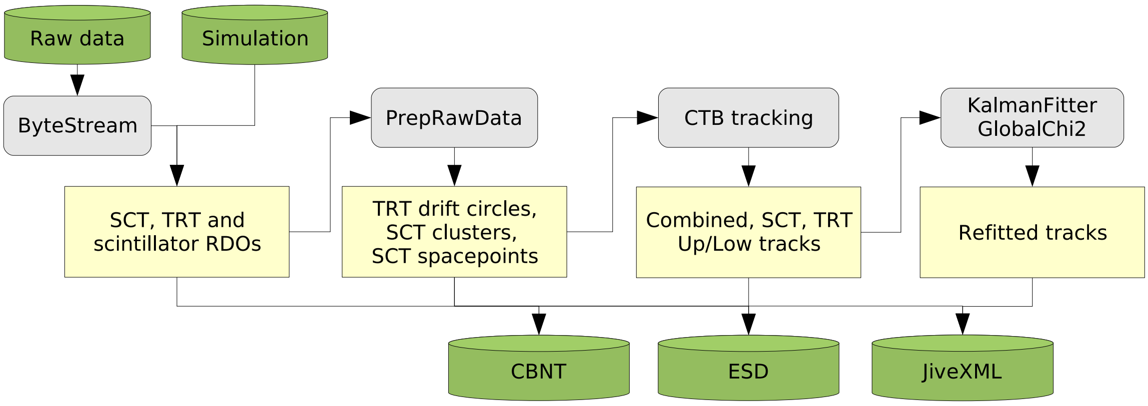

Figure 10. Cosmic ray reconstruction data flow.

- **Byte Stream converters**

  The byte stream converters are responsible for decoding the different ROD event fragments and creating a raw data object (RDO) for each recorded signal. The result is an SCT RDO per consecutive group of strips or an individual strip that had a signal (depending on whether the ROD is configured to run in "condensed" or "expanded" mode), and a TRT RDO per hit straw. All the information written by the different detectors describing the signal is stored in the RDO objects.

  The converters use the ATHENA cabling service to map the ROD channel numbers to the corresponding detector elements.

  Since the cosmic trigger was not synchronized with the 40 MHz readout clock the time difference between the trigger and the next clock edge is also stored in the TRT RDO in the case of the barrel setup to allow for a drift time correction.

  Specific converters and RDO classes were developed in the same framework in order to store the ADC and TDC information produced in the different scintillator photomultipliers.

- **Data preparation**

  The raw data objects created by either the simulation or the real detectors are translated into positions in space using the detector geometry information and calibrations.

  For the SCT, clusters containing one-dimensional measurements in the sensor plane are produced. The stereo angle between the two different sides of a layer is used to form two-dimensional measurements, which combined with the known radial positions of the layers determine space points.

  For the TRT, the drift time information is translated into the corresponding radius using the R-t calibration curves, parametrized by a third degree polynomial. For simulations, the parametrization is an integrated part of the reconstruction software and depends on the T_0 configuration used in digitization. For real data the calibration constants are provided by the procedure described in section 5.1.7.

- **Track finding and fitting in the barrel setup**
  Since there was no magnetic field in the cosmic setup, the muons moved in straight lines through the detector. Also, the tracks do not originate at the centre of the detector. For the barrel test, the CTB tracking program [33], which was developed with such scenarios in mind, was used as default track finder. Straight line tracks are used as the fit model, meaning four track parameters to fit: ϕ, the angle in the transverse plane, θ, the angle with the z axis, d_0, the point of closest approach to origin in the transverse plane, and z_0, the intersection point with the z axis.

  CTB tracking consists of a pattern recognition part, which is possible to seed from either SCT or TRT hits, and a track fit part based on a χ^2 minimization method.

  The pattern recognition in the SCT works with space points, and in the cosmic rays configuration it looks for at least three space points on a line. If a good combination is found, the track is extrapolated to modules with no space points, and eventual clusters close to the track in these modules are added. The track can then optionally be extrapolated to the TRT, where hits close to the track are added. The pattern recognition can also work in standalone TRT mode without an SCT seed. The number of hits on a line is then required to be at least 20.

  By default, tracks provided by the CTB tracking are fitted by a global χ^2 fitter, and can optionally be refitted by a Kalman filter technique that is being used by default in the Inner Detector reconstruction. Since the momentum of the incoming muons cannot be measured with the SR1 setup, material effects are not taken into account in the fit.

- **Track finding and fitting in the endcap setup**
  The CTB tracking was developed specifically for a barrel-like geometry. It was extended to deal with hits in the SCT endcap but not with hits in the TRT endcap. A different track finding strategy was therefore used for the endcap setup, where the CTB tracking was only used to find SCT only tracks.

  For the TRT endcap, a dedicated pattern recognition algorithm had to be developed as the ATLAS default pattern recognition assumes that tracks originate from the interaction point, which is in general not the case for the cosmic muons. As the TRT endcap does not provide a measurement of the radial position of a hit, the pattern recognition only provides TRT segments within the $z-\phi$ plane. These TRT segments are then fitted with a Kalman filter assuming the direction as given by the scintillator layout in order to provide full tracks.

  In a second step, the TRT-only tracks are then fed into a backtracking algorithm that starts with the TRT track and tries to extend it into the SCT and collect all matching hits. In addition, another algorithm combines SCT-only tracks found by the CTB tracking and the TRT-only tracks.

  In the final step, ambiguities that arise due to the different ways a track can be found are resolved and only the best candidate is kept.

- **Output data**
  The output of the reconstruction can be stored in several formats: An ntuple containing information from tracks, SCT clusters, TRT drift circles, raw data from detectors, and TDC

and ADC data from the scintillators. The data can also be stored in an ESD (Event Summary Data) format, where the full objects (TrackParticles [35], Tracks and associated hits) are stored. A third option is to write data in an XML [38] format used by the standard ATLAS event display Atlantis [37].

3.3.4 Conditions database

In this context, *Conditions* are those factors which will influence the datastream interpretation. The ATLAS standard database for the storage of conditions is the COOL database, which represents a technology independent schema for the storage of conditions. This permits their retrieval by run/event number or by timestamp during the analysis. The various conditions data used are described below:

- **DCS Conditions**

  DCS conditions are measurements made of the temperatures, voltages, and currents by the ATLAS DCS system PVSS [14]. Environmental factors such as temperature, humidity, and module power parameters were recorded in PVSS at regular intervals and subsequently uploaded to the COOL database to be made available to the offline analysis.

- **Configuration**

  The SCT is configured from an XML file containing all the data acquisition configuration (including cabling), the power supply configuration, and the individual module and chip configurations. The configuration files for each run were transformed via XSLT [39] to a form appropriate for uploading to the COOL database, and were subsequently used in the analysis to identify, for example, masked channels.

- **Calibrations**

  The calibration data are taken as part of a dedicated calibration run and used to determine the noise levels of the modules and optimal noise settings. The calibration is “published” to the online information service and subsequently uploaded to COOL using the Conditions Database Interface (CDI). For the TRT, calibration data includes the drift $R-t$ relationships for the straws.

- **Data Stream Conditions**

  The data stream itself contains information about errors arising from the modules or their RODs. This can reveal a faulty communication channel and thus determine whether the data stream itself is trustworthy.

- **Data Quality**

  As a result of analysis, online or offline, it may be determined (by recording the channel efficiency) that a channel or module has become noisy during the run, or is no longer giving data. The data monitoring algorithms write this information to a local database for use during the interpretation of the data. This local database can subsequently be merged with the main COOL database for use in all further analyses.

- **Alignment**

  The alignment data were stored using a different schema and allow precise location of the space points from hits. This subject is treated more fully in the Alignment sections.

3.4 Monitoring

3.4.1 Event filter monitoring

A monitoring system is needed in the data acquisition system to assess the quality of the data sent to permanent storage. In the ATLAS Data Acquisition and Data Flow system, the Event Filter (EF) is the third level of the trigger process, receiving completely assembled physics events from the Sub-Farm Input (SFI). Data are transmitted by the Event Filter Data Flow (EFD) to the Processing Task (PT), where the trigger algorithms run.

The EF is therefore the natural place to perform the monitoring of high level physics quantities, and cross-checks among different detectors. A key feature of the EF monitoring is its capability of providing data quality checks even before data is stored to disk.

The EF monitoring is based on a monitoring framework [40] that is provided by the ATLAS Trigger and Data Acquisition (TDAQ) system. Fundamental services provided by the monitoring framework [41] are:

- **Event Monitoring (Emon)**

  Emon provides event sampling. User programs can request event fragments from a specific sampling source.

- **Online Histogram Service (OHS)**

  The OHS handles histogram objects and in particular ROOT [42] histograms. It is used to share information among histogram providers and subscribers. The functionalities for providers are: create, update, and delete. Subscribers can subscribe to a particular histogram in OHS and be notified about a change in its state.

- **HistoSender**

  HistoSender is a service of the High Level Trigger (HLT) infrastructure that collects histograms from the ATHENA histogram service and publishes them in the OHS.

- **Online Histogram Present (OHP)**

  OHP [43] is the ATLAS histogram presenter based on QT [44] and ROOT. It can browse histograms published in OHS and display them in automatically updating tabs with user-defined graphical options.

The EF segment, controlled remotely by the DAQ system, runs on a dedicated server so that PT processes do not share resources with other DAQ subsystems. The server also hosts a replica of the offline, online, and HLT software in order to reduce as much as possible the startup time of the EF segment.

During SR1 commissioning, only a part of the ATLAS TDAQ system was in place, as shown in figure 11. In particular, there was no SFI during SR1 data taking, so that event data were passed

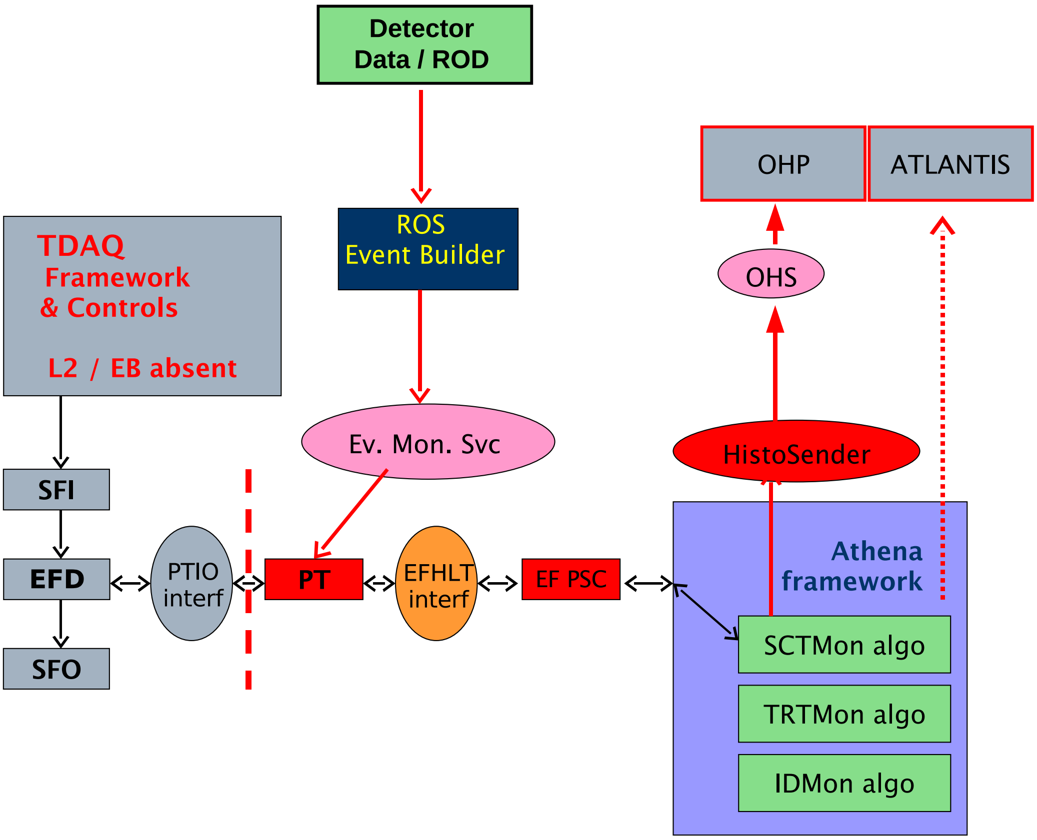

Figure 11. Schematic description of the EF segment as used during SR1 tests.

to the PT not by the EFD, but via the Emon service from the Event Builder (EB). The PT is synchronised with the DAQ transition states via the EF Process Steering Control (EF PSC), part of the HLT interface.

Subdetector and global monitoring. The inner detector monitoring tools are all implemented as ATHENA algorithms, and hence are run offline and as online Athena PT processes, as described above. There are separate SCT and TRT packages, and a global tool that aims to examine issues of synchronization.

The SCT Monitoring tool plots hit maps at both the module and strip level as well as monitors module and track efficiencies, cluster sizes, hit correlations between module sides and between layers, track residuals and pulls, tracking hit information (such as number of hits on a track, track χ^2, etc), byte stream errors, and noise occupancies. The software provides a number of algorithms for monitoring detailed detector information, and is commonly configured to produce a subset of the total information for online use due to the more limited resources in the online environment. Full details of the package development are contained in Reference [45].

The TRT monitoring tool produces histograms that show timing-related information for the straws like the measured drift time in the straws or the time-over-threshold for low level and high level hits. Further histograms include plots of the $R-t$ relation (drift distance versus drift time

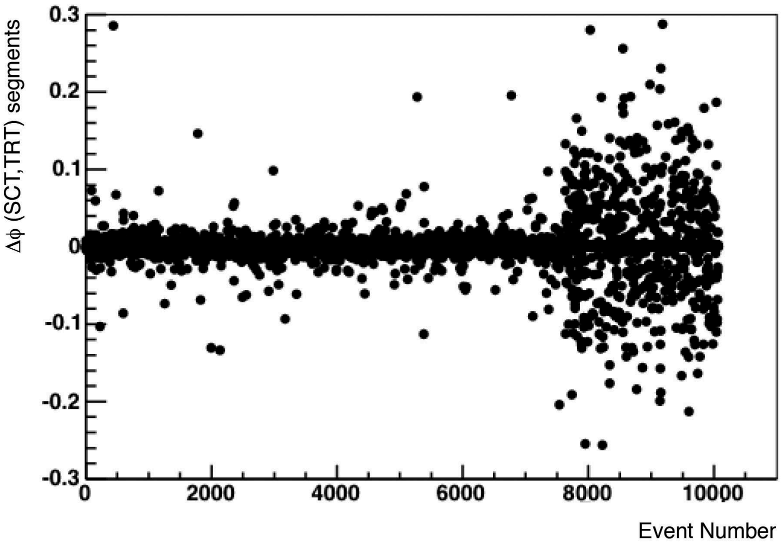

Figure 12. Difference between the SCT and TRT reconstructed track ϕ parameter as a function of the event number for one run of the combined barrel test. The synchronization between the readout of SCT and TRT subdetectors was lost at event ≈7600 and the run was stopped.

in the straw) for track hits, number of low-level and high level hits on a track as well as the track residual, which is the difference between measured and predicted hit positions. Another set of histograms monitors geometric quantities like the track's impact parameter or its azimuthal angle. Additionally, various straw, noise, and track hitmaps are available.

The list of histograms produced by the global monitoring tool includes the synchronization between the SCT and TRT readout, the $\Delta\phi$ of the perigee parameters of the SCT and TRT versus event number (see, for example, figure 12), the mean number of SCT and TRT segments, the noise occupancy of the SCT and TRT, and the number of hits found on global tracks. Figure 12 shows the difference of azimuth angle of track segments in the SCT and TRT versus event number, which is used to monitor the synchronization of readout between the subdetectors. It is clearly visible that the synchronization between the readout of SCT and TRT subdetectors was lost around event 7600 and the run was stopped. The example shown in figure 13 gives the variation of the noise occupancy on the TRT Endcap C with the event number. In this case, the noise occupancy increased from around 2% to 6% due to a trip of the analogue low voltage regulators. The global monitoring is also capable of extrapolating tracks from the SCT to the TRT in order to examine the TRT straw efficiencies.

3.4.2 SCT specialized monitoring

Most of the low level information about the SCT modules can be extracted directly from the byte stream file using an SCT standalone, monitoring program (sctComTool) with an event stream decoder which unpacks the ROD fragments. As a result the hit strip numbers, trigger delay, and readout errors are available. The byte stream has enough information to assign a hit to a module.

The low level monitoring includes occupancies at strip, chip, and module levels; dependencies

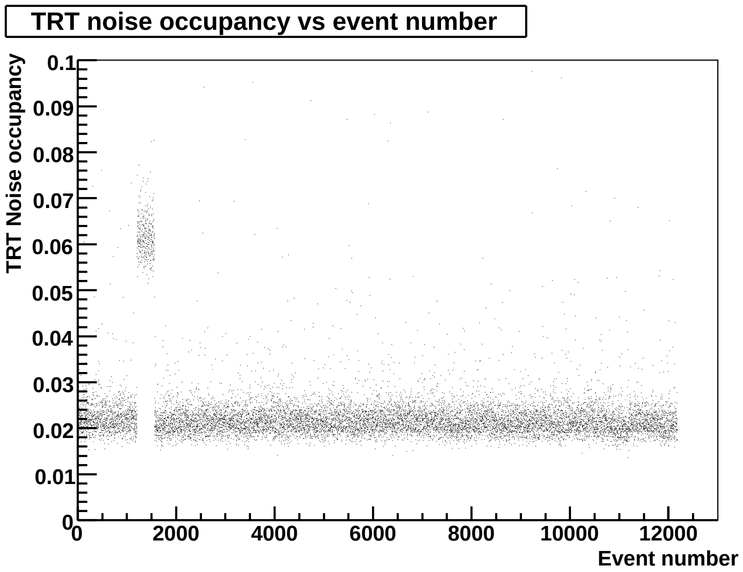

Figure 13. TRT Endcap C noise occupancy as a function of the event number. A LV trip occurred around event 1100.

of single and double hit[8] occupancies on the trigger delay; and readout errors. A study of the occupancy dependence on the trigger delay provides two types of results:

- If the trigger is random then the only recorded signals are due to noise. Different occupancies at different trigger delays can indicate the presence of correlated noise with other subsystems.
- If the readout is triggered by real particles passing through the detector then the maximum occupancy at certain trigger delay will indicate the right time for readout. The double hit occupancy takes into account the position correlation between hits at both sides of a module and therefore such occupancy should give better noise background rejection. This leads to more pronounced dependence of the double hit occupancy from the trigger delay.

The hits from tracks in the SCT will strongly bias the measured noise occupancy if these hits are not subtracted. Therefore a special procedure was developed which determines the occupancy at module level on an event-by-event basis and subtracts the hits which were identified as belonging to space points.

3.4.3 TRT specialized monitoring

During the SR1 tests a TRT standalone monitoring tool (TRTViewer) was extensively used. TRTViewer runs at the ROD-Crate-DAQ (RCD) level and is a detector oriented tool which was specially developed as a flexible debugging and a fast diagnostics instrument. It is based on a ROOT framework and contains some primitive tracking based on the least squares method, which is necessary for the time tuning of the TRT parts and checks of the TRT basic functions.

The TRTViewer concept is based on the visualization of the basic detector characteristics according to the physical location of the elements: straws, chips, electronics boards, and detector

---

[8] A double hit is a coincidence between two sides of a module.

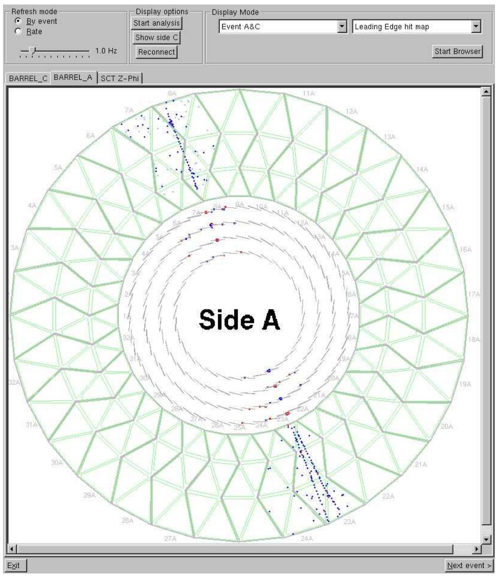

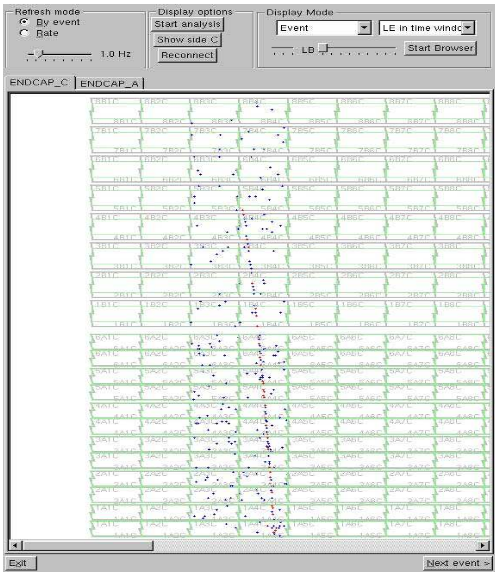

Figure 14. Cosmic muon event in the barrel ID visualized with TRTViewer.

Figure 15. Cosmic muon event in the EC-TRT visualized with TRTViewer.

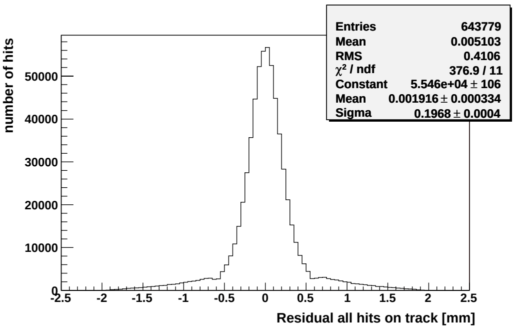

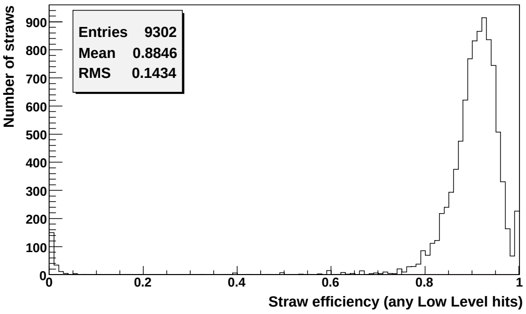

Figure 16. Online histogram of the distance between a track and a reconstructed hit in the TRT.

Figure 17. Online histogram of the straw efficiency for the cosmic tracks.

modules. It includes the presentation of DCS and DB parameters, raw data for each channel, noise characteristics, TRT performance parameters like straw particle efficiency, and tracking performance statistics. The tool can work directly online, either with received data from the sampler during DAQ operation or with recorded data. It allows the evaluation of the performance of all of the hundreds of thousands of detector channels practically at the same time, thus allowing one to examine the misbehaviour of the detector components. Raw data presented by the TRTViewer as an Event Display for the Barrel ID and EC TRT during the SR1 tests are shown in figure 14 and figure 15. The barrel picture shows a cosmic muon event detected during a combined TRT/SCT cosmic run and contains TRT and SCT information. Blue points for the TRT correspond to the straws which have the hits. Blue and red points for SCT correspond to the stereo strips which have the hits.

Examples from the online monitoring results of the TRT tracking properties during a combined cosmic run are shown in figure 16 and figure 17. For these the internal tracking code was used as described above. The tests were performed with an Ar/CO_2 gas mixture. Figure 16 shows the distribution of residuals between reconstructed track positions and straw space points. The precision of the drift time measurement achieved by the online monitoring tool is about 200 μm. This is close to the value obtained for a single straw with a silicon microstrip telescope in the test beam for the Ar/CO_2 mixture [46]. Figure 17 shows the straw hit efficiency. The low efficiency tail comes from straws with limited statistics. All parameters are within the TRT specification.

4. Tests with random triggers and calibration runs

4.1 SCT noise performance

The electrical performance of the SCT was monitored through all stages of construction and integration. The main test points were

- During module construction
- After mounting of modules to complete single barrels and disks
- Assembly of disks in the endcap cylinder
- After final assembly of the SCT and TRT

The test procedure and results of these tests are described in detail in references [3, 4], and [47]. Results presented here will focus only on the tests done at SR1 after the final SCT and TRT assembly. The aim was to examine the noise performance of the combined system and check for cross-talk. The noise can be measured either through module calibration or by running the DAQ system in physics mode using a random trigger.

4.1.1 Results from module calibration

The tests perfomed in calibration mode consisted of a full characterization of the analogue performance using the built-in calibration circuitry. Two main parameters were verified in these tests: the number of defective channels and the noise performance (as equivalent-noise-charge *ENC* or noise occupancy). Defective channels with different fault signatures were categorized using these test results. These and further calibration tests are described in more detail in reference [17].

In the setup phase of the module readout, each module was configured and triggers were sent to it. The correct communication was verified by sending, reading back, and comparing a known test pattern of varying length to the ABCD3TA mask registers [21].

After module setup the digital function of the module was verified. First, the proper function of the digital pipeline of the ABCD3TA chip was checked by issuing a “Level 1 Accept” (L1A) trigger after a chip reset. The delay between trigger and reset was varied to scan all pipeline cells. The hybrid of the SCT modules has the capability of by-passing the readout of a chip in case it is faulty. The functioning of this bypass scheme was checked by bypassing each chip of the module one at a time.

Following the successful completion of digital tests the analogue performance was tested for each channel. In the “3-point-gain” test, three test charges (1.5 fC, 2.0 fC, and 2.5 fC) were injected in each channel and its gain was measured by a threshold scan for each test charge. From the curve

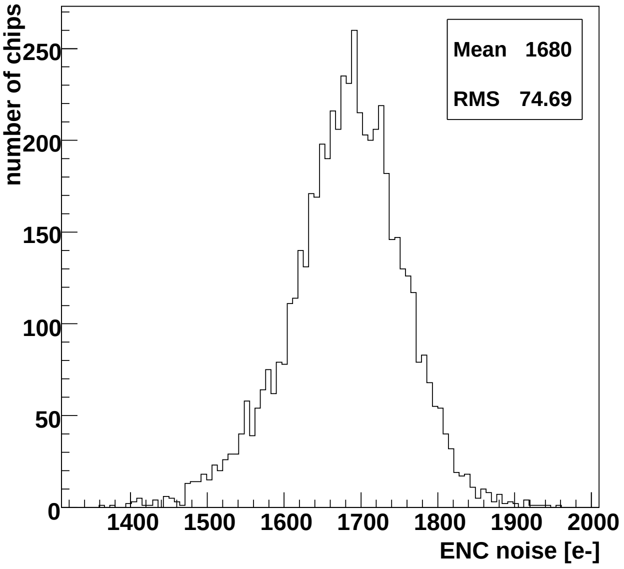

Figure 18. Distribution of average equivalent noise charge (ENC) per readout chip for the SCT barrel sector during combined testing as measured by the SCT calibration.

of the threshold scan data, the gain was extracted as the threshold for 50% efficiency. A fit of a complementary error function to the threshold scan yields the output noise at 2.0 fC, which was used to extract the equivalent noise charge (ENC) as output noise divided by the channel gain. Figure 18 shows the average ENC noise per chip of the two sectors used in the combined tests. The ENC was measured at a hybrid operation temperature of around 28 °C. The choice of temperature was driven by practical constraints of the test setup for dew point control. For final operation in the experiment we envisage a hybrid temperature of ≈0 °C, which will reduce the ENC noise [17].

With this noise test it was possible to identify defective channels (noisy or dead) as well as bonding defects (noise too high or low). The tests also allowed a comparison of the number of defective channels with results from earlier integration studies. No significant increase in the number of bad channels was observed. From measurements carried out on single barrels and disks during the previous integration stage, we determined the percentage of defective channels as 0.2% in the SCT barrel and 0.3% in the SCT endcaps [17, 22].

The noise occupancy was measured with a threshold scan without charge injection. We define the noise occupancy as the single channel noise occupancy per bunch-crossing. This strip noise occupancy is usually averaged over a readout chip (128 channels), or a module side (768 channels), or a full module (1536 channels). We quote the noise occupancy (number of noise hits per channel and L1A trigger) for a threshold of 1 fC, which will be the operational threshold in the experiment. The goal for the SCT is to have a noise occupancy of less than 5×10^{-4}. Figure 19 shows the noise occupancy averaged over each chip of the two sectors used in the combined tests.

4.1.2 Results from random triggers

The noise tests performed in SR1 included runs at high trigger rates, tests of different grounding schemes, and tests of FE noise pickup during the active readout cycle of the TRT. In these tests the

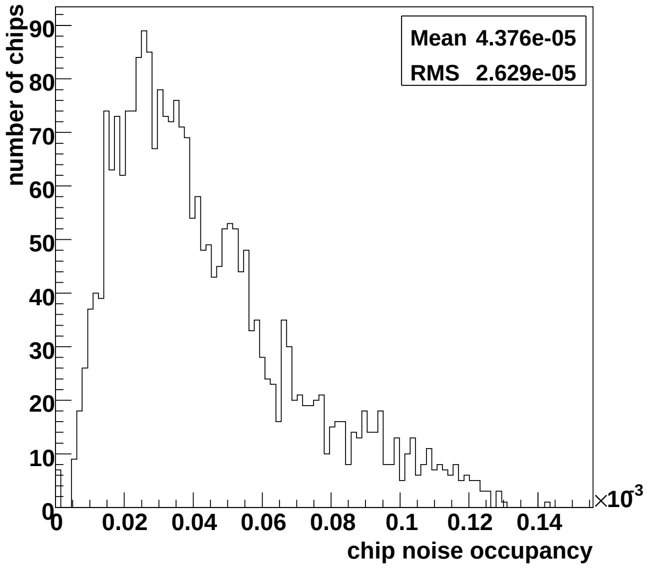

Figure 19. Distribution of average noise occupancy per readout chip for the SCT barrel sector during combined testing as measured by the SCT calibration.

readout of the detectors was triggered by a pulser at fixed frequency or a pseudo-random trigger. Unless otherwise stated, the results shown here were obtained by running the ATHENA offline code on data that were taken with the SCT module thresholds set to 1.0 fC as given by the response curve calibration.

A simple illustration of the noise behaviour of the barrel SCT can be seen in figure 20, which shows the strip number for all hits in the first 10000 events of a run in which both the SCT and TRT were powered and read out. The strip channel number goes from 0 to 767, covering all strips on one side of a module. Hits from both sides of the module are therefore superimposed on the plot. The spikes represent the noisy strips present in the fraction of the SCT that was read out. They appear on a background of uniform noise.[9] These nine noisy channels (out of a total of 718848) match those identified as problems in the calibration. Both subdetectors were triggered using a pulse of 50 Hz and the thresholds of the SCT modules were set to 1 fC. The expected modulation of the noise occupancy within a chip (128 channels) is also apparent in figure 20. The higher noise toward the middle of the chip is due to power distribution inside the chip.

Several tests were performed in SR1 in order to investigate specific noise effects. These are summarised below, and the results of the noise are given for each.

Trigger rate scan. For both the barrel and the endcap, physics mode runs were taken with different trigger rates in order to check if this has any effect on the noise occupancy. The module thresholds were set to 1 fC, and all other settings, such as the presence or absence of the TRT, were not changed between runs.

Tables 4 and 5 contain a summary of the averaged noise occupancies measured for each layer

---

[9] In this sense, the plot shows the typical behaviour of a module side, with some smearing due to the cumulative effect of superimposing all module sides on the same plot.

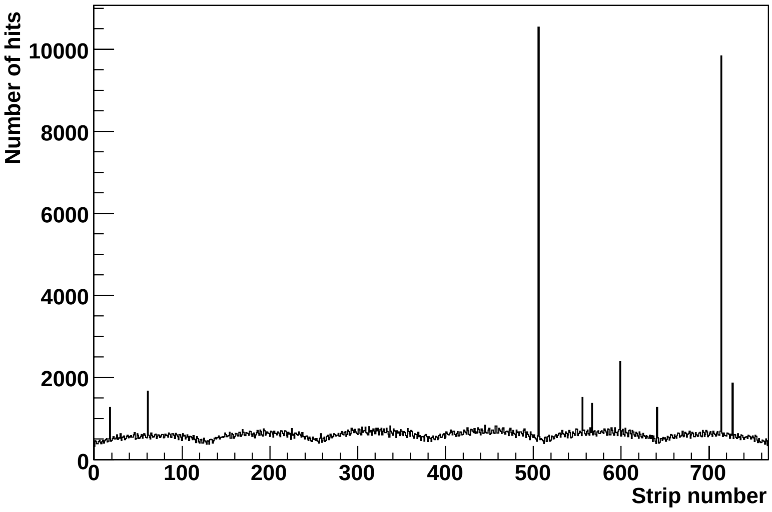

Figure 20. The strip number distribution for all hits in the SCT.

Table 4. The mean (RMS) barrel noise occupancy (scaled by 10^5) for runs taken with different trigger rates.

	500 Hz	5 kHz	50 kHz
Layer 0 Side 0	4.87 (3.13)	4.94 (3.14)	4.92 (3.17)
Layer 0 Side 1	4.94 (3.28)	5.01 (3.28)	4.97 (3.23)
Layer 1 Side 0	4.36 (1.83)	4.33 (1.81)	4.33 (1.80)
Layer 1 Side 1	4.92 (2.39)	4.89 (2.37)	4.84 (2.33)
Layer 2 Side 0	4.26 (2.16)	4.26 (2.12)	4.22 (2.15)
Layer 2 Side 1	4.89 (2.51)	4.90 (2.49)	4.88 (2.44)
Layer 3 Side 0	4.90 (3.34)	4.89 (3.31)	4.86 (3.30)
Layer 3 Side 1	4.75 (2.93)	4.78 (2.96)	4.78 (2.98)

(disk) side of the barrel (endcap). Layers are numbered in the barrel starting with “0” for the innermost barrel, Barrel 3, to Layer 3 for the outermost barrel, Barrel 6. The trigger rate does not appear to affect the noise occupancy. The two sides or each module are denoted as “Side 0”, the top side of the module, and “Side 1”, the module side which faces the support structure.

Noise threshold scan. An important test of module behaviour is the noise occupancy as a function of threshold. In the low noise regime, occupancy is related to the threshold by the following empirical description [48]:

$$N \propto \exp\left[-\frac{t^2}{2\sigma^2}\right] \tag{4.1}$$

where t is the module threshold, N is the noise occupancy, and σ is the equivalent noise charge of the module.

Physics mode runs were taken with different thresholds for both the barrel and the endcap. The barrel runs were triggered from a pulse at a frequency of approximately 500 Hz, with the TRT clocked but not read out.

Table 5. The mean (RMS) endcap noise occupancy (scaled by 10^5) for runs taken at different trigger rates.

	1 kHz	10 kHz	50 kHz	100 kHz
Layer 0 Side 0	3.78 (1.87)	3.58 (1.76)	3.57 (1.75)	3.41 (1.69)
Layer 1 Side 1	3.87 (2.21)	3.86 (2.15)	3.87 (2.19)	3.78 (2.09)
Layer 2 Side 0	5.04 (2.53)	4.76 (2.35)	4.74 (2.37)	4.73 (2.37)
Layer 3 Side 1	4.49 (3.12)	4.17 (3.04)	4.48 (2.87)	4.23 (2.92)
Layer 4 Side 0	4.50 (2.84)	4.46 (2.49)	4.11 (2.59)	4.09 (2.68)
Layer 5 Side 1	4.16 (2.77)	4.16 (2.63)	3.92 (2.68)	4.12 (2.61)
Layer 6 Side 0	5.53 (3.46)	5.29 (3.24)	5.33 (3.37)	5.25 (3.30)
Layer 7 Side 1	5.47 (2.47)	5.47 (2.72)	5.40 (2.71)	5.31 (2.73)
Layer 8 Side 1	3.66 (2.04)	3.69 (2.01)	3.60 (1.96)	3.58 (1.88)

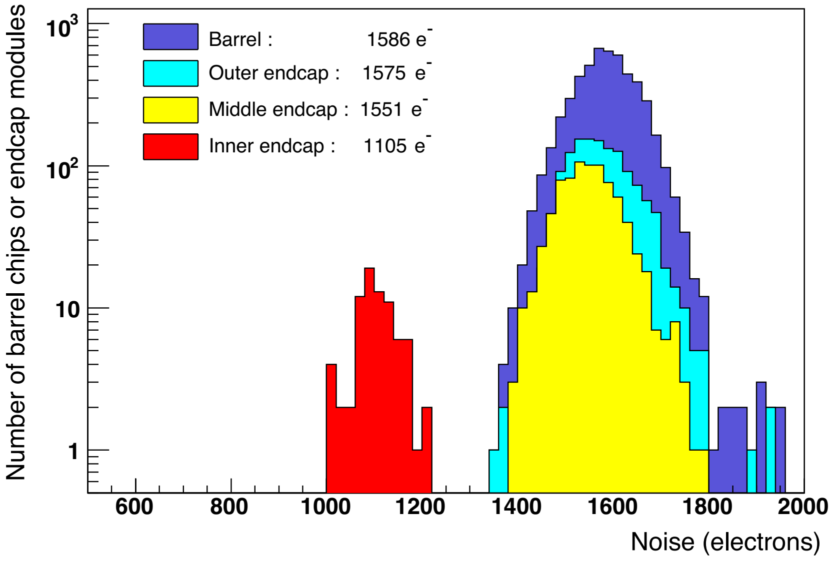

Figure 21. Distribution of the ENC values (in number of electrons) for all module sides obtained in noise threshold scan.

Equation 4.1 indicates that a plot of $\ln(N)$ versus t^2 should be a straight line, and its slope allows the equivalent noise charge for each module to be extracted. The distribution of the averaged ENC values obtained for all module sides of the SCT barrel and endcap modules is given in figure 21. Barrel modules and outer and middle endcap modules have approximately 12 centimeter long strips, where the strips on two wafers are bonded together. Endcap inner modules have about 6 centimeter long strips on one wafer. The shorter strip length implies a smaller load capacitance on the frontend input, which in turn implies lower noise. An example of one of the straight line fits is given in figure 22. The ENC values obtained are roughly equivalent to those reported from calibration runs, though an exact comparison is difficult to make due to differences in the way the data were analysed.

The noise occupancy specification limit of 5×10^{-4} demands that the total equivalent noise charge should not exceed 1900 e^- [49]. All of the ENC values presented here are within this

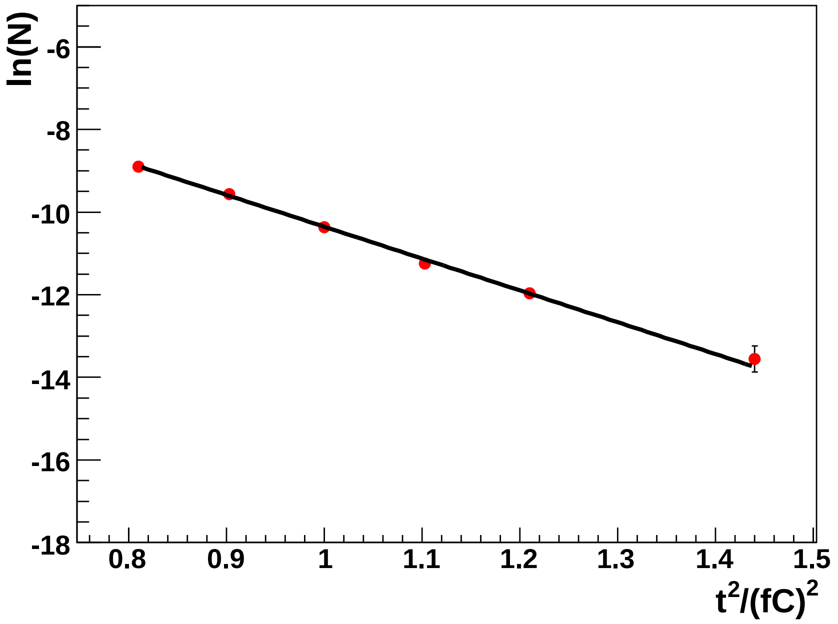

Figure 22. A plot of $\ln N$ versus t^2 for one module side of the barrel SCT. A straight line has been fitted (see equation 4.1), with a slope $p_0 = -2.6 \pm 0.2$ (fC)$^{-2}$ and intercept on the y-axis $p_1 = -7.7 \pm 0.2$.

limit once a small number of known noisy strips with a noise occupancy greater than 5×10^{-3} are masked off.

For the barrel, two different grounding schemes were investigated with the above method, and it was found that these did not affect the noise occupancy. A similar test was not performed on the endcap.

Trigger timing delay scan. Since the TRT and SCT were operated together for the first time, an important point to investigate was whether the TRT induces any noise in the SCT. The TRT starts reading out about 3.25 μs after a trigger. The SCT was therefore triggered about 3 μs after triggering the TRT to search for pickup induced in the SCT by the TRT readout cycle. The BOC Tx coarse delay, which is the delay between incoming trigger and SCT L1A, was then scanned in steps of 75 ns in order to add extra delay between the triggering of the SCT and the TRT, and the time delay was written into the byte stream. If no noise pickup occurs, the noise occupancy should be flat when plotted against time delay, as no extra noise occupancy is observed when the TRT is read out.

Plots of the barrel noise occupancy versus time delay are given in figure 23 for a run in which the TRT was off, with its FE electronics unpowered, and for a run in which the TRT FE electronics was clocked and read out. The analysis was performed with strips masked off if their noise occupancy was greater than 5×10^{-3}. In the analysis we required the hits to be recorded in the correct middle time bin, denoted by the “X1X” hit-time pattern. The noise occupancy is flat in each plot, and thus it is concluded that there is no evidence for noise pickup from the TRT. Furthermore, no dependance on the bit pattern of the hits was observed. Plots of the endcap noise occupancy are given in figure 24. Again, there is no evidence of noise pickup resulting from the TRT. Also, there was no dependance on the bit pattern of the hits for the endcap.

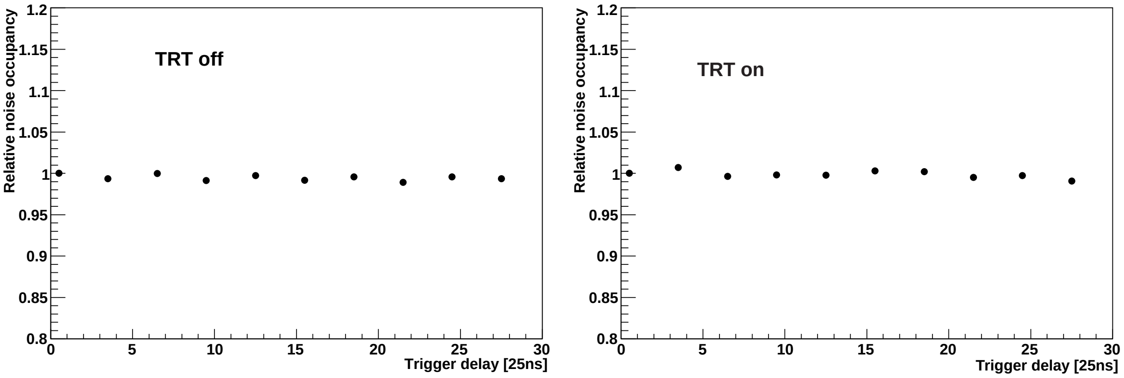

Figure 23. Noise occupancy (normalised to the first bin) versus time delay for the SCT barrel. The TRT was off for the plot on the left, and thus the data provide a calibration plot with no noise pickup from the TRT. The right-side plot was obtained from a run with the TRT on.

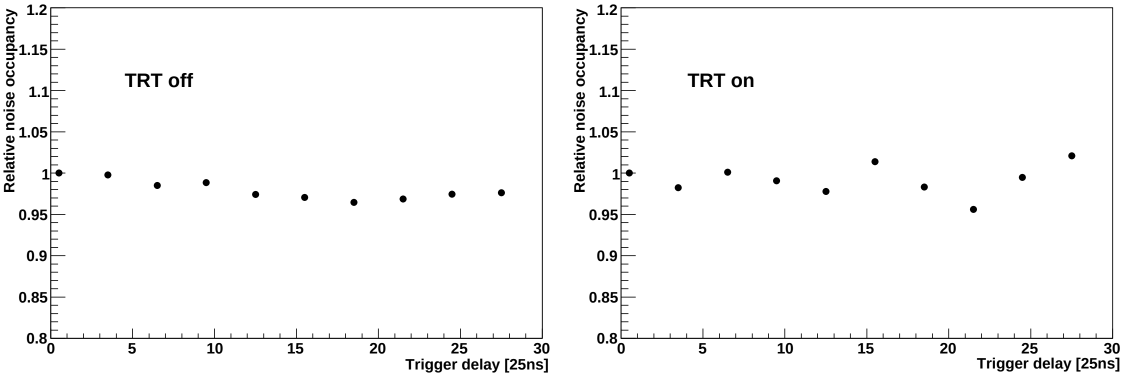

Figure 24. Noise occupancy (normalised to the first bin) versus time delay for the SCT endcap. The left-side plot represents a run when the TRT was off, the right-side plot represents a run when the TRT was on.

Final noise occupancies. The distribution of noise occupancies for all module sides is shown in figure 25, excluding, for reasons of scale, the inner endcap modules, which were found to have a mean noise occupancy of 1.6×10^{-7}. The module thresholds were set to 1 fC and the analysis was performed with strips with an occupancy greater than 5×10^{-3} masked off.

All occupancies are below the design specification of 5×10^{-4}, though for the barrel data there is a slight increase from previous tests, where barrels were operated individually (a mean of 4.5×10^{-5} is quoted in reference [3], compared to 4.76×10^{-5} here). Although it is possible in principle that this small increase will scale with the number of modules that are connected, previous noise tests performed with differing numbers of modules on the final SCT barrels showed no evidence that the performance degrades in the large system [3]. It would thus appear that the SCT is running comfortably within its design specification.

Channels on Side 1 show slightly higher noise occupancy than Side 0, as seen in figure 26 for barrel data. The plots show data with the module thresholds set to 1 fC as obtained from the

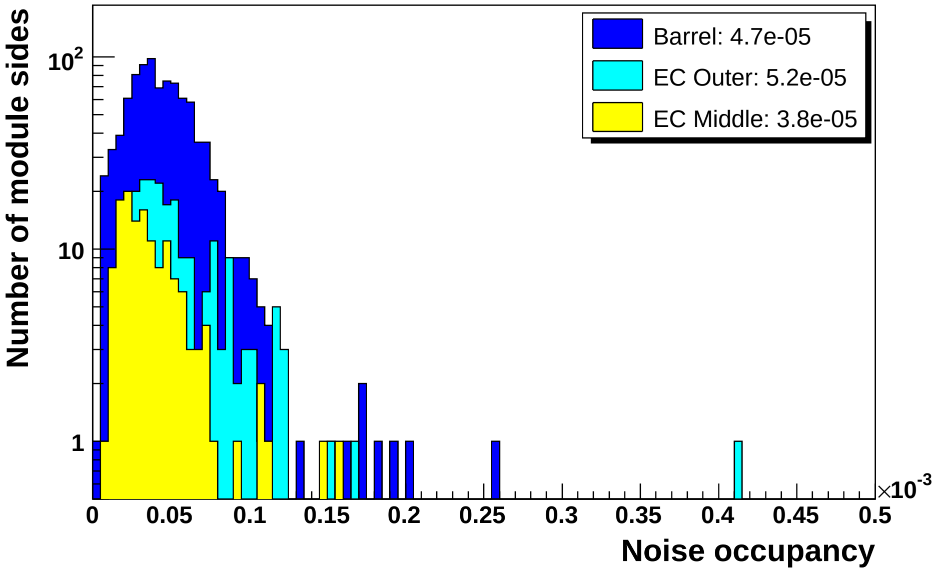

Figure 25. The distribution of noise occupancies for all module sides of the SCT detector, excluding the inner endcap modules.

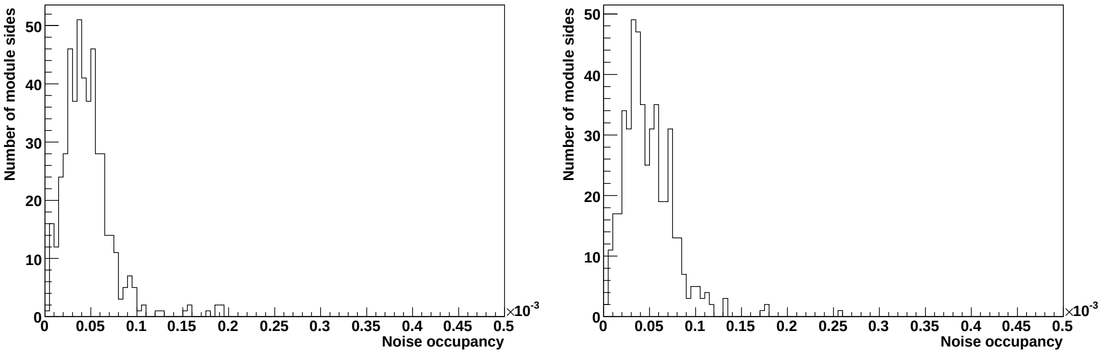

Figure 26. The distribution of noise occupancies for the active modules of the SCT barrel detector for Side 0 (left) and for Side 1 (right).

response curve calibration. The Side 0 distribution has a mean of 4.62×10^{-5} and an RMS of 2.70×10^{-5}, while the Side 1 distribution has a mean of 4.90×10^{-5} and an RMS of 2.80×10^{-5}. This is consistent with results obtained during module production.

4.2 TRT noise studies

Some of the most important issues during the combined tests were noise studies for different detector configurations and different grounding schemes. Particular attention was given to the possibility of inducing noise in the TRT from the SCT during combined operation.

TRT grounding and Faraday cage efficiency issues were addressed during standalone tests. It was found that a proper ground connection between the frontend boards and the Faraday cage is an important factor for the suppression of clock pickup noise. These connections must be made

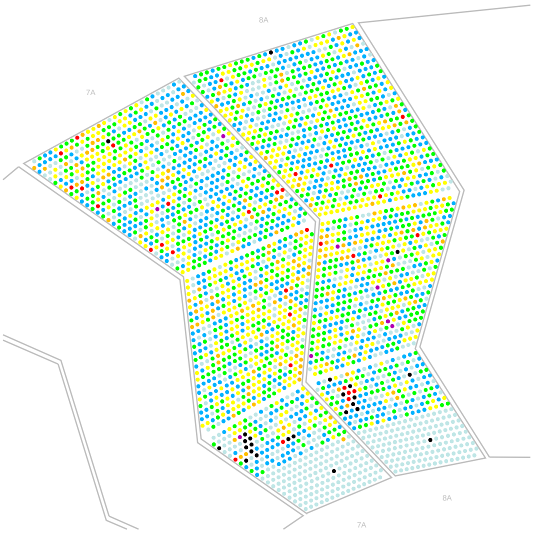

Figure 27. Noise occupancy map for the Barrel TRT sectors participating in the noise tests. Yellow coloured straws have noise occupancies about 1.3% and black coloured straws have noise occupancy above 4%.

with a spacing of not more than 3 cm to make a frequency cut at the level of above 100 MHz. After the implementation of this system, the noise level for most of the TRT channels was close to that defined by thermal fluctuations. A typical picture of the TRT noise hit map for the modules participating in the test is shown in figure 27. Yellow coloured straws have a noise occupancy of about 1.3% and black coloured straw have a noise occupancy above 4%. One finds a group of straws in the TRT module Type 1,[10] which can be associated with one DTMROC chip with a systematically large noise occupancy. That is a known problem of these particular boards and is related to the board layout in which the 40 MHz clock line has a capacitive coupling with the ASDBLR inputs. Details of the noise distribution across the channels are shown in figure 28. Most of the channels have noise at the level of 1%, but clock pickup affected channels have noise levels of up to 15%. Although that is a substantial noise level, it does not severely affect the physics performance.

A series of tests were performed to evaluate the change in TRT noise during the combined operation of the SCT and TRT. The first test aimed to see the effect of SCT frontend power on TRT noise occupancy. The noise occupancy differences for one of the TRT stacks (Stack 7) for sides A and C are shown in figure 29. Positive values indicate an increase in noise between the reference (when the SCT was off) and when the SCT was on. Negative values indicate a decrease in noise. All deviations are within standard noise behaviour.

Following the ATLAS grounding convention, all detectors must have an independent ground connection at one controlled point. In order to evaluate what happens if an uncontrolled ground short appears during installation in the pit, a special test was carried out. A worst case ground connection was artificially created between the analogue ground plane in the TRT and the SCT power return. A comparison of the TRT noise occupancy for this run with the reference one is shown in figure 30. No statistically significant effect was found during these tests.

A particular subject of interest was the effect of the SCT readout cycle on the TRT noise

---

[10] TRT barrel modules are stacked in layer with Type 1 modules forming the innermost layer, Type 2 modules the

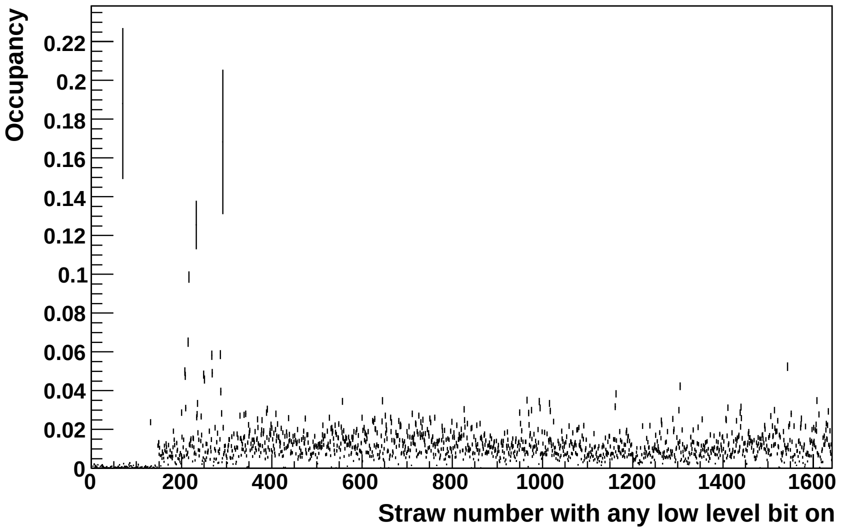

Figure 28. Noise occupancy distribution across the channels for one of the TRT Stacks (Stack 7 on Side A). Typical noise occupancy is about 1.3%.

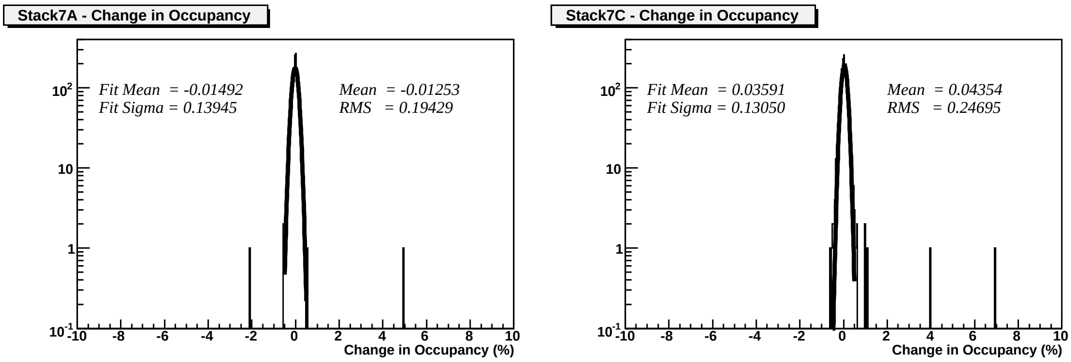

Figure 29. Comparing noise occupancy when the SCT is off with a run when SCT is on. The horizontal axis shows the difference of occupancy with SCT on minus occupancy with SCT off in percent. The vertical axis gives the number of straws.

occupancy. Two types of tests were performed. In the first, TRT noise measurements were made during SCT operation at a trigger rate of 50 kHz. In order to increase SCT frontend digital activity, the SCT threshold was set to 0.8 fC. No change in the TRT noise occupancy was found. Another test aimed to look at exactly what happens during the SCT readout cycle. The time at which the SCT frontend chips transmit their header words to the backend corresponds to the maximum amount of frontend digital activity. Data were taken using different TRT delays with respect to SCT trigger. Figure 31 shows the typical occupancy difference with respect to the reference run. Again, no noticeable change was observed.

---

middle layer, and Type 3 modules the outermost layer.

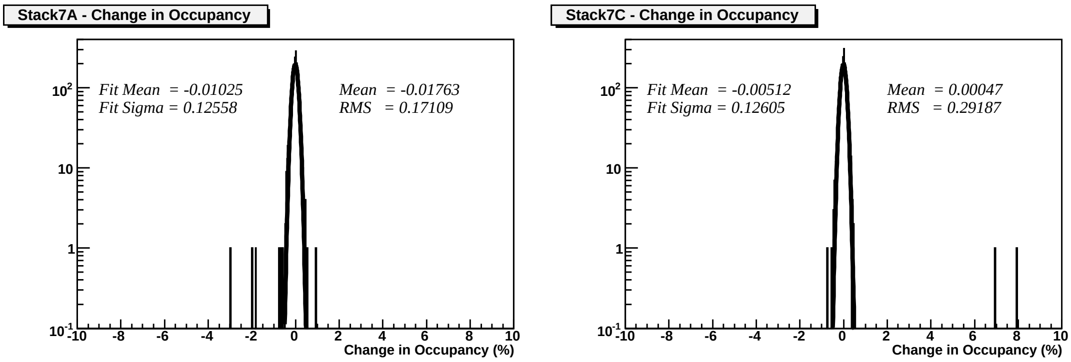

Figure 30. Comparison of the TRT noise occupancy when the TRT analogue ground plane is connected to the SCT power return with the TRT standalone noise occupancy.

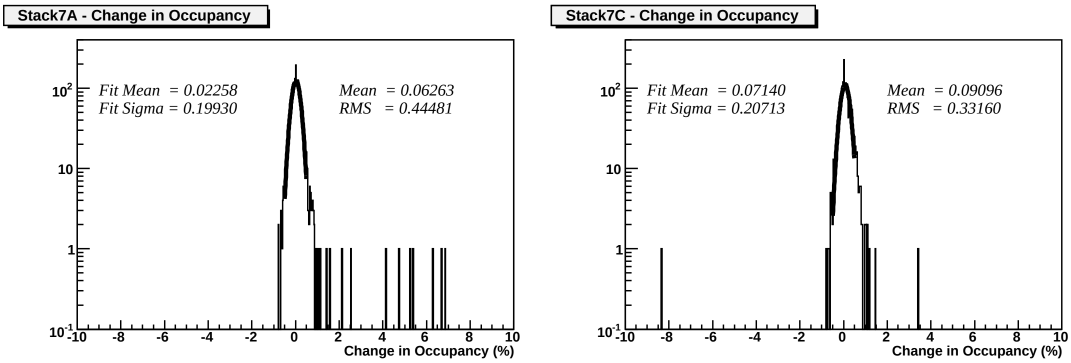

Figure 31. Comparison of the TRT noise occupancy during SCT readout cycle with the TRT standalone noise occupancy.

5. Tests with cosmic triggers

5.1 Alignment and calibration

5.1.1 Alignment of the SCT and TRT

The determination of the position of the detector elements in space is crucial in order to make full use of the intrinsic resolution of the tracking device. The relative alignment of the sensors in a module is given by the mounting precision during the module assembly [3], which used tolerances well below the sensor spatial resolution. The mounting precision of modules on disks and barrels is less well known compared to the intrinsic resolution. This would lead to a significant degeneration of the tracking performance and needs to be corrected in the alignment step.

The position of the detector elements can be determined with track based alignment algorithms, based on the optimization of hit residuals. A perfectly aligned detector returns a residual distribution centered around zero and with a width consistent with the quadratic sum of the intrinsic resolution and the uncertainty originating from the track fit. A misaligned detector setup leads to a off-centered residual distribution with an increased width originating from the additional misalignment uncertainty.

Track based alignment algorithms use the fact that the fit of the track trajectory is over-constrained and the deviations from the helix or the straight line in case of no magnetic field are minimized with respect to the translational and rotational degrees of freedom of the detector [50]. Any deviation from the description of a perfect trajectory will appear as a misalignment of the detector. Therefore the track selection processes for track based alignment use tracks with high momentum to avoid kinks in the trajectory originating from multiple coulomb scattering (MCS) effects. As described above, the test setup was not inside a magnetic field. The momentum of the various charged particles could not be determined and no selection criteria based on the momentum could be applied. The momentum spectrum of particles from cosmic rays is dominated by low momentum particles, which suffer substantially from multiple scattering. The width of the residual distribution, the quadratic sum of the intrinsic resolution, and the uncertainty from the track reconstruction, is therefore dominated by multiple scattering. In particular, the impact of misalignment effects on the residual width is small compared to the multiple scattering effects. The track fit algorithm normally applies the measured momentum to estimate the contribution from multiple scattering to the overall track position uncertainty. Since no momentum measurement is available, the uncertainty cannot be calculated and the multiple scattering contribution is set to zero. This leads to a significant underestimation of the uncertainty on the track position.

The track based alignment approaches are based on the minimization of hit residuals. This is a necessary, but not sufficient requirement. The vertical track topology of the charged particles originating from cosmic ray events can lead to degeneracies in the solution of the alignment, for example, a shearing of the detector in the YZ-plane cannot be recovered. In addition, vertical movements along the track trajectory of the two shells are not constrained. These deformations, so called *weak modes*, cannot be recovered by the alignment approaches. No track control sample with a different track topology was available to verify the quality of the alignment constants independently. Therefore the conclusion on the obtained alignment constants is only limited.

Each SCT module has six degrees of freedom: three translations and three rotations. The translation perpendicular to the strips is expected to be determined best. Overall for the SCT $6 \times 467 = 2802$ degrees of freedom have to be aligned. The TRT has no sensitivity along the wire, leading to five degrees of freedom per module times 12 TRT modules in the readout (overall 60 degrees of freedom).

Several internal alignment approaches were developed and applied to data taken with the barrel SCT and the barrel TRT. The tracks used for the alignment were reconstructed using the standard ATLAS reconstruction software framework ATHENA and the alignment algorithms were also implemented as a part of ATHENA.

5.1.2 Alignment of the SCT

Various alignment approaches were applied to align the SCT barrel in the SR1 cosmic setup [51 – 54]. All approaches are based on the optimization of hit residuals. Figure 32 shows the residual distribution for all modules located in a certain SCT layer obtained with the Global χ^2 approach [52]. In this approach each module is aligned for six degrees of freedom. Modules with fewer than 150 hits were kept stable. It is clearly visible that the residual distribution is distorted before the alignment corrections are applied. After the alignment the mean for all layers is centered around zero and the width of the residual distribution is reduced compared to the width obtained with the

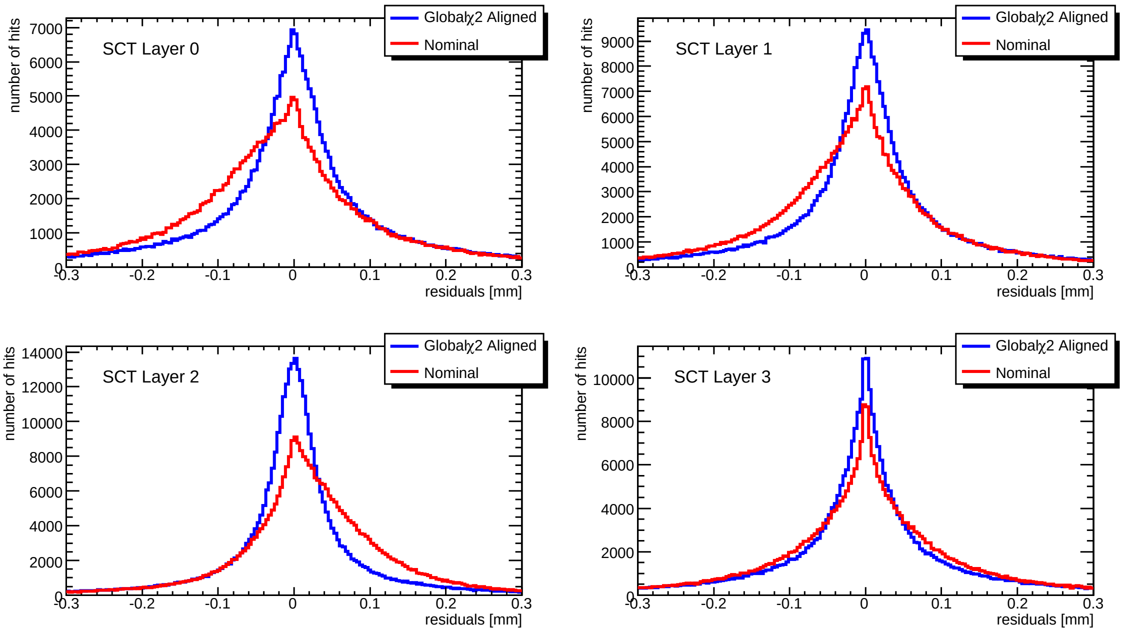

Figure 32. The SCT biased residuals for the different layers of the SCT are shown before (red) and after (blue) the alignment.

misaligned setup. The other alignment approaches returned similar results. As mentioned previously, the width of the residuals distributions is dominated by multiple scattering and, in particular, effects due to detector misalignments might not be noticeable. In addition, the contribution to the track uncertainty originating from the track fit is largely underestimated, since the contribution from multiple scattering is not calculated.

All alignment algorithms used an iterative approach to get a stable result. Figure 33 shows the residual quantities as a function of iteration. The mean as well as the resolution of the residual distribution converges to a stable number after three iterations. Convergence was reached when the movements of the detector were smaller than the corresponding statistical uncertainty. The initial shift of the mean was removed and the width of the resolution σ got significantly smaller. The width of the residuals varies between layers because the track error varies along the track, e.g., due to multiple scattering.

The magnitude of the shifts obtained in the local X direction (orthogonal to the strip direction) is generally of the order of 100 μm. The local Y alignment constants (along the strip direction) are of the order 600 μm.

5.1.3 Comparison of alignment results with the photogrammetry measurements

Due to the fact that no magnetic field was used during SR1 data taking all tracks coming from cosmic rays are straight lines. Thus, this setup was ideal to determine the relative rotations of the SCT detector barrels in ϕ. A similar measurement was performed analysing the photogrammetry data [56]. The first set of the three photogrammetry measurements, which was taken in November 2005 [55], was precise enough to determine relative barrel rotations. However, these measurements

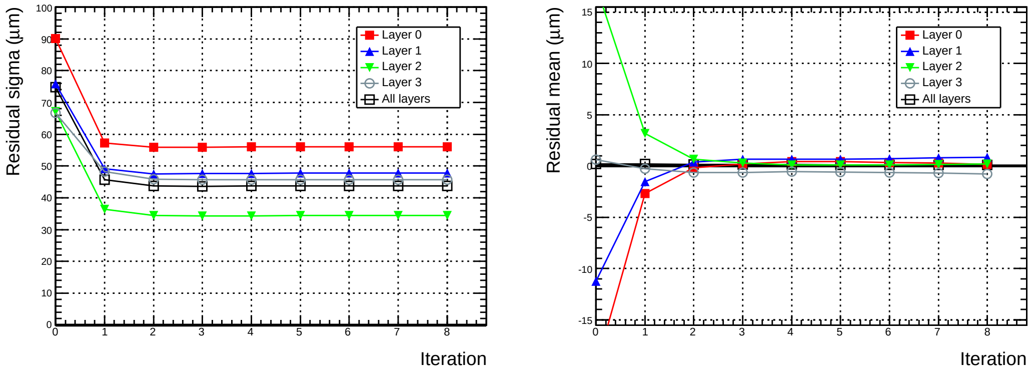

Figure 33. This figure shows the resolution σ of the biased residual distribution (left), and the mean (right), for the four different SCT layers and all layers combined obtained after each iteration.

were taken before the insertion of the SCT into the TRT. The change from the four point mounting on the temporary SCT support to the mounting of the SCT on rails inside the TRT may have led to significant global distortions of the SCT. This type of distortion may create systematic, radius-dependent barrel rotations.

Figure 34 shows the measurement of the photogrammetry data in comparison with the measurements performed by the three track based alignment algorithms. The track based algorithms determined the same relative barrel rotations within the errors of the measurement. The results from the photogrammetry differ from the alignment results in two of the layers. It is not quite clear whether this difference arises from actual barrel movements or from the fact that the systematic uncertainties of the photogrammetry measurements are not perfectly understood. However, the systematic deformations mentioned above may explain the difference.

Furthermore, the relative barrel shifts in the global Z direction were analysed. Again, it appears that all alignment algorithms determine the same systematic distortions within the uncertainties. Since all alignment algorithms used the same reconstructed tracks and hit residuals as input, a systematic bias in the reconstruction could also lead to a common systematic bias for all alignment approaches. Correlation for the ϕ and global-Z alignment could therefore lead to relative shifts in Z.

5.1.4 Relative alignment between the SCT and TRT

The relative misalignment between the barrel TRT and the barrel SCT is expected to have a larger impact on the track reconstruction than the misalignment of the internal components of these detectors. It is also possible that a large misalignment between the two detectors could affect the track finding efficiency leading to a poor convergence of the alignment procedure.

A survey measurement of the relative position of the four SCT layers and the TRT was performed “in situ” (see table 6). A special procedure was implemented to determine the relative SCT-TRT misplacement with tracks reconstructed from cosmic data. It proceeds as follows:

- TRT and SCT tracks are fitted separately and the SCT tracks are extrapolated to the first TRT straw layer;
- A 2D residual is formed from the difference in the track coordinates in the plane perpendicular to the straw layer surface (the TRT has no sensitivity along the wire direction);

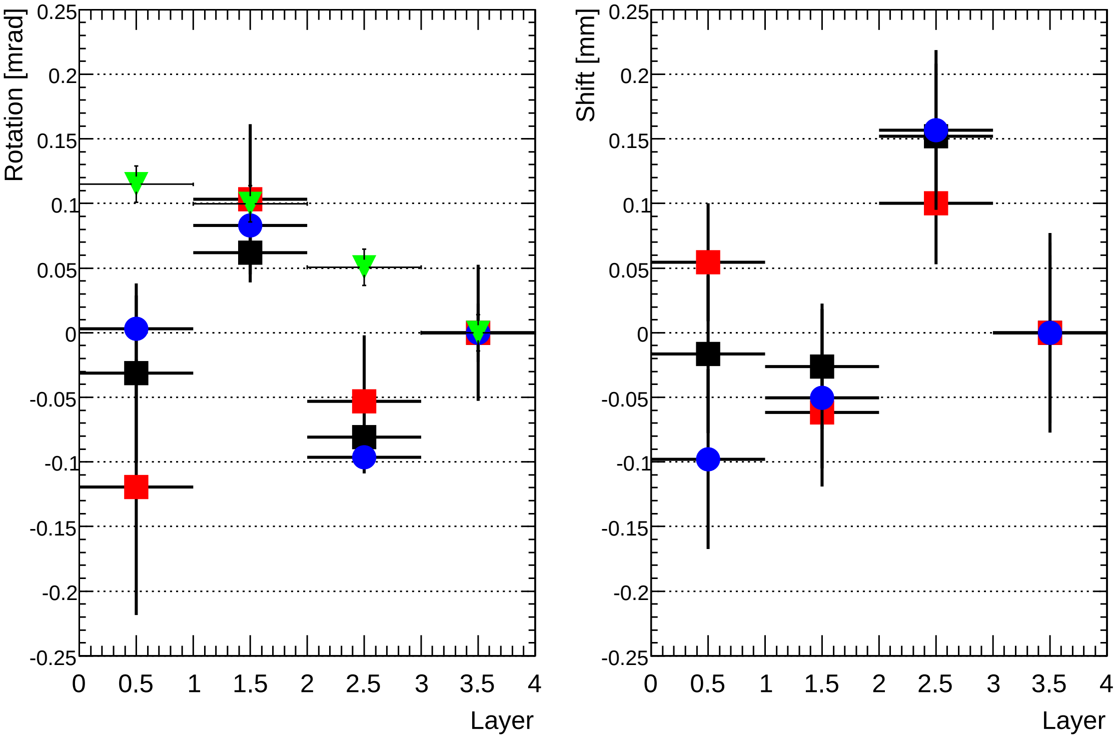

Figure 34. For each SCT layer the relative rotation of the whole SCT barrel in ϕ is shown in mrad (left) and the relative Z shift in mm (right). Photogrammetry measurement are represented by green triangles, Robust Alignment results by blue circles, Local χ^2 Alignment results by black squares, and Global χ^2 Alignment results by red squares. The alignment sets have been transformed into a common reference frame and normalised to layer 3.

Table 6. Relative translation and rotation between the SCT barrel and the TRT barrel as determined from the survey measurements.

Δx [mm]	Δy [mm]	$\Delta rotX$ [mrad]	$\Delta rotY$ [mrad]
-0.42	+0.33	+0.154	0.165

- A χ^2 is constructed and minimized with similar techniques used in the alignment algorithms. Because of the SR1 setup (tracks almost vertical and no TRT sensitivity along z) only the misplacement along x (Δx) and the rotations around the y (Δrot$Y$) and z (Δrot$Z$) axes could be calculated.

This alignment procedure was applied to tracks collected from two different runs, one at the beginning and one at the end of a stable period of data taking. The two resulting SCT-TRT misalignment values are consistent within their estimated uncertainties. Moreover, the track-based measurements are found to be consistent with the survey measurements mentioned before.

5.1.5 Alignment of the TRT

After correcting for the relative alignment between the barrel SCT and TRT detectors, an internal

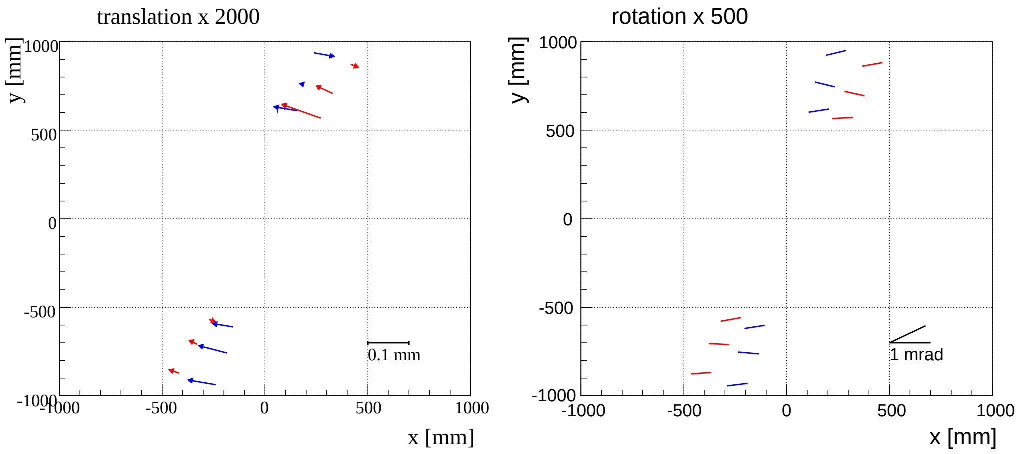

Figure 35. Measured translations (left) and rotations (right) of TRT modules. The direction and size of the arrows in the left plot represent the direction and size of the translations. The rotation of the module in the right plot is proportional to the angle of the bar with the horizontal axis.

alignment of the TRT modules is carried out. In contrast to the SCT internal alignment described in section 5.1.2, where only SCT tracks were used, the TRT alignment employs extended SCT-TRT tracks. Since TRT tracks do not provide information outside the *xy*-plane, SCT hits are needed to obtain the *z* coordinate of the track. Consequently, for a correct calculation of the TRT misalignment, the SCT modules need to be precisely aligned. A framework was developed to align TRT and SCT modules simultaneously and two of the approaches used in the SCT standalone alignment (section 5.1.2) have been implemented in the framework. The result of this procedure is an alignment that is consistent across both systems. The alignment constants obtained for the SCT are comparable, in terms of residuals, to the results from the other SCT alignment methods already presented. Therefore, we will only report the TRT results.

The alignment of the TRT was limited to only the two most sensitive degrees of freedom, namely the direction perpendicular to the wire in the straw layer plane (ΔX) and the rotation around the wire axis ($\Delta \mathrm{rot}Y$).

The limited statistics and the nearly parallel track trajectories did not allow us to perform the TRT module alignment for the other weakly constrained degrees of freedom. The convergence of the alignment constants after successive iterations was reasonable, with the residual distributions centered at zero after alignment. However, in contrast to the SCT case, the width of the TRT residual distributions only marginally improved, due to the fact that for the TRT the alignment corrections are small ($< 50\ \mu$m) with respect to the width of the residual distribution. In figure 35 the TRT module displacements returned by the alignment algorithm are shown graphically with the values scaled for clarity. As can be seen, layer 0 and layer 2 modules are rotated in the same direction while layer 1 modules are rotated in the opposite direction (both by approximately 300-400 μrad). Such a pattern is consistent with an elliptical distortion of the TRT (or possibly the SCT), but a conclusive interpretation cannot be obtained from the SR1 cosmic data.

A study of possible TRT module deformations was also carried out. TRT module deviations from the rigid body approximation are expected (caused by, for example, construction imperfections, or mechanical stress) and if they are larger than the detector resolution, a correction must be applied. In terms of alignment, they effectively produce a hit displacement depending on the hit position inside the module. Given the limited amount of available data, we limited our study to the residual dependence on the hit position along the straw axis. Because the measurement of this coordinate is not provided by the TRT, it was derived by extrapolating SCT tracks to the TRT straw layer under study (as a consequence, remaining alignment deviations in the SCT can also appear as module deformations in the TRT). For modules with larger statistics (layer 1 and layer 2) we actually observed significant deviations from zero. Some patterns are consistent with module twists, others show more complicated deformations. A final conclusion on the magnitude of such deformations and their impact on track reconstruction will require more extensive data sets from p-p collisions.

5.1.6 Alignment summary

Tracks reconstructed from cosmic ray events were used to determine the alignment of the barrel SCT, the barrel TRT, and the SCT with respect to the TRT. The calculated barrel alignment constants give a first indication as to the magnitude of the detector misalignments. The results for the alignment are limited by multiple scattering of low momentum tracks. In addition the vertical topology of the tracks from cosmic ray events leads to *weak modes* of the detector, which cannot be resolved by track based alignment algorithms.

The three SCT alignment algorithms return consistent results. The magnitude of the shifts in the local X direction is generally of the order 100 μm. The local Y alignment constants are of the order 600 μm. The comparison of the rotation around the global Z-coordinate between the track based alignment and photogrammetry measurements is not conclusive due to systematic uncertainties.

The alignment of the aligned SCT relative to the TRT is determined using tracks passing through both the SCT and the TRT. The alignment result is consistent with the survey measurement of the inner detector.

After the internal SCT alignment and the alignment of the SCT relative to the TRT an internal alignment of TRT modules is performed. For this, SCT tracks extended to the TRT are used. The various TRT modules move by about 50 μm and are rotated by about 300 to 400 μrad around the wire axis. Internal deformations of the TRT modules are studied, but no final conclusion is possible.

5.1.7 TRT drift time calibration

Drift time model. The TRT measures the drift time, the time between the LHC bunch clock and the arrival of the signal to the anode wire, in time-to-digit counts (TDC). A measured TDC value is a function of the position and orientation of the charged particle trajectory with respect to the drift cell. Since the TRT drift cells are symmetric around the wire axis, the drift time is only a function of the distance to the anode wire. The model used for calibration therefore reduces to:[11]

$$\mathrm{TDC}(r) \;=\; \alpha(t_{\mathrm{drift}}(r)+t_0). \tag{5.1}$$

---

[11] The propagation time and time-of-flight contributions were not taken into account.

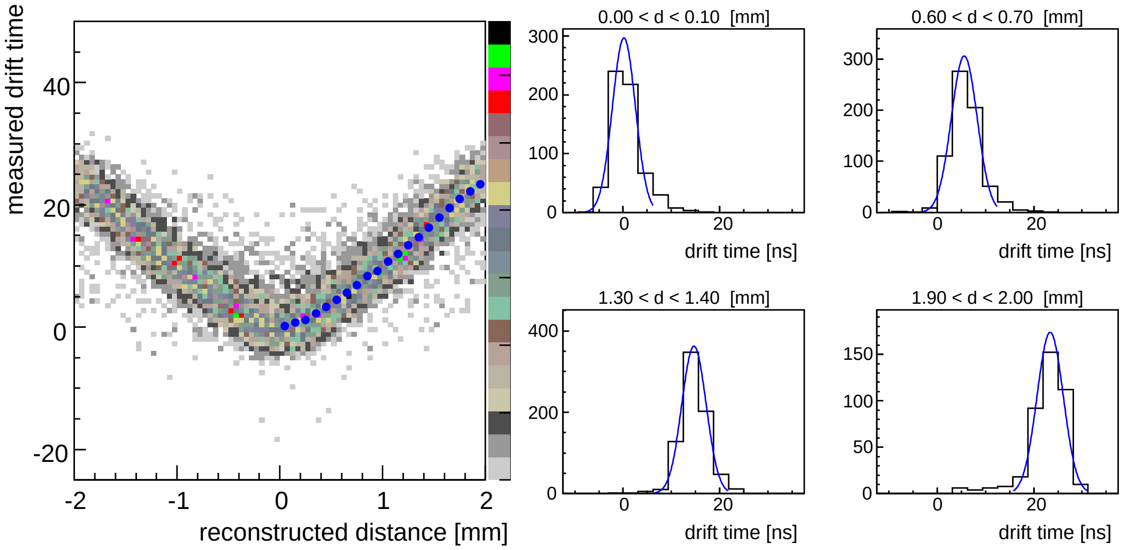

Figure 36. TRT barrel time-to-distance distribution (left) and the drift time distribution in 4 distance intervals (right). The smooth curves in the right figures represent the result of the fit with a Gaussian. The blue points in the left plot represent the result of the fitted mean for each distance bin.

where $\alpha = 8/25[ns^{-1}]$, r represents the distance to the anode wire, t_{drift} is the drift time, and t_0 is a channel dependent offset.

Drift time calibration procedure. The drift time calibration procedure uses reconstructed tracks to translate the TDC value into the best possible estimate of r. For each hit, the measured drift time is computed and the *rt* relation determined from the distribution shown in figure 36. The 2-D distribution in figure 36 is divided in 0.1 mm bins in r and 3.125 ns bins in t. In each r-bin the maximum of the drift time distribution is determined by fitting a single Gaussian to the 5 bins centered around the most occupied bin, in order to reduce sensitivity to the tails as shown in figure 36 (right).

The *rt* relation is then parametrized using a third degree polynomial. The t_0 offsets are determined from the average drift time residual of reconstructed hits, computed from the measured drift time and the inverse of the *rt* relation. The corrected t_0's are obtained by subtracting the average drift time residual. Since our method relies on reconstructed tracks while the track reconstruction itself relies on a proper calibration, the procedure depends on a reasonable starting point for both the *rt* relation and t_0. We have found that the procedure could be bootstrapped with a single constant t_0 and a simple linear *rt* relation. The procedure was robust against the choice of the initialization and converged typically in 2 iterations.

Results obtained with SR1 cosmics data

Barrel. Since no reliable momentum estimate is available, tracks are reconstructed without taking into account MCS effects. To reduce the effect of MCS, reconstructed tracks are split into their top and bottom segments. For each segment we require at least 20 TRT hits.

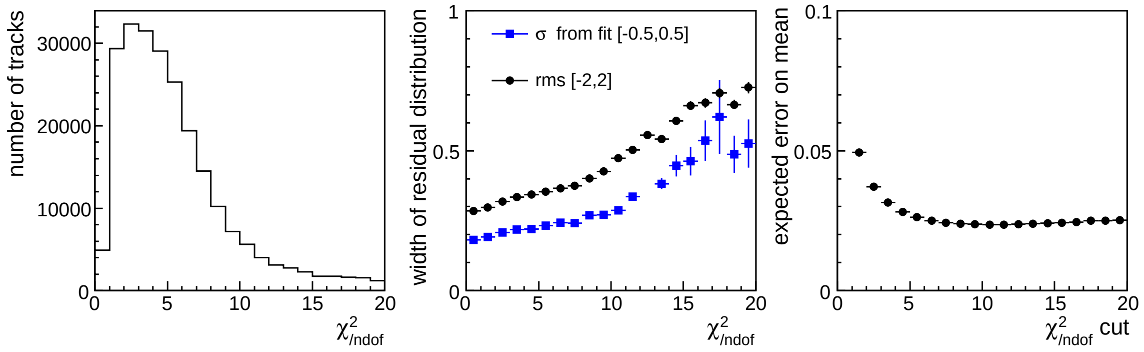

Figure 37. Distribution for χ^2/ndof (left), width of the unbiased residual distribution in bins of χ^2/ndof (centre), and estimate of the uncertainty on an estimate mean for a hypothetical set of 100 hits (right).

In the calibration procedure we require for each hit a time-over-threshold of at least 2×3.125 ns and a maximum time residual of 15 ns. The latter is chosen large, approximately 5 times the single hit resolution, to allow recovery from a poorly chosen starting value for t_0 in the first iteration. To improve the quality of the selected track segments, a cut is made on the χ^2/ndof of the track. To prevent a bias in the calibration the χ^2/ndof is first reduced by the contribution from the selected hit. The resulting χ^2/ndof distribution is shown in figure 37.

The centre plot in figure 37 shows the width of the unbiased residual distribution in bins χ^2/ndof. The width is measured both as an RMS on the interval ± 2 mm and as the σ of a Gaussian fit on the interval ± 0.5 mm. The latter result shows that a single hit resolution of around 200 μm is obtained.

To motivate the choice of a particular χ^2/ndof selection we calculate the uncertainty on the mean of the residual distribution as a function of the χ^2/ndof cut. The uncertainty is estimated as $\sigma(\text{mean}) = \text{RMS}/\sqrt{N-1}$. The rightmost plot in figure 37 shows the result, normalised for a hypothetical set of 100 hits. As one can see contribution from hits with $\chi^2/\text{ndof} > 10$ actually degrades the resolution on the mean.[12] Therefore only hits for which χ^2/ndof is smaller than 10 are selected in order to reach an optimal sensitivity for calibration. Although this may seem to be an unrealistically large value, it already rejects a significant fraction of the segments because multiple scattering effects are ignored.

For the cosmics data we use a single *rt* relation for all straws. The drift time offset t_0 is determined for each straw separately. The uncertainty in the t_0 is the RMS of the drift time residual distribution divided by the square root of the number of entries (minus 1). Since the RMS of the drittime residual distribution is itself proportional to the resolution, the fractional contribution of the uncertainty in t_0 to the hit resolution is about $\sqrt{1+1/N} - 1 \approx 1/2N$. To keep this contribution below 1% one would need about 50 hits per straw. For the calibration of the cosmics data we have required a minimum of 25 hits, based on considerations discussed below. For straws not fullfiling the above requirements, we use the average value of the t_0 of the corresponding TRT module as a compromise between the statistical and systematic uncertainties.

It is generally assumed that the time offsets of straws within one "DTMROC" unit (16 straws

---

[12] The reason that we *lose* sensitivity, even though we *add* information is that in the extraction of the mean we do not use the fact that the uncertainty varies with χ^2/ndof.

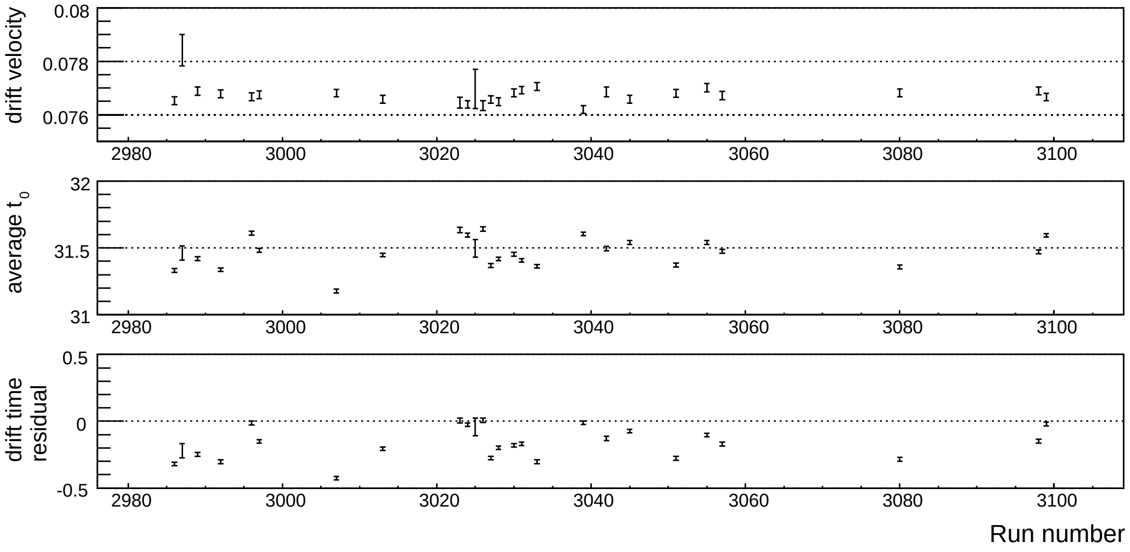

Figure 38. Drift velocity for $0.2 < |d| < 1.8$ (top), average straw t_0 (middle) and average drift time residuals with respect to the calibration of run 3099 (bottom) as a function of run number.

connected to one amplifier) are equal to within 0.5 ns. If this is the case, it would certainly make sense to combine the data from straws in a DTMROC. Unfortunately, the mapping to DTMROCs was not available within ATHENA during the analysis of the combined test data.

Calibration constants derived from a single run were used for the reconstruction of all data. To test the stability of the calibration the average drift velocity and the average drift time residuals as a function of the run number was studied. Results from these studies are shown in figure 38. From those results it is clear that the average drift time offset is stable to within ± 0.5 ns. For the cosmics data this is sufficiently small with respect to the hit resolution to justify the use of a single calibration.

Endcap. To achieve the best calibration of the TRT, good quality tracks are a very important ingredient. For the endcap setup, the tracks were of a worse quality compared to those in the barrel setup. The average number of hits per tracks in the endcap was about 6, compared to 20 in the barrel. In order to make the endcap tracks longer, the drift radius error was set to a higher value, about 240 μm. An immediate consequence is an increase in the rate of noisy hits as shown in figure 39.

To reduce the noise rate, only hits for which the time-over-threshold was within the interval 3×3.125 ns and 12×3.125 ns were used. To better enhance the track quality, the χ^2/ndof was required to have a maximum of 20, and the time residual to have a maximum of 25 ns.

For the endcap setup, no TRT trigger phase was measured. Therefore, the phase was determined from the tracks themselves. For each track, the average drift time residual of the measured drift time and the drift time from the track was calculated. The trigger phase was obtained by requiring this average to be 0.

Another issue was that in a fraction of events leading signal edges were missing due to large time offsets in some frontend boards, which were not timed in with respect to each other. Events

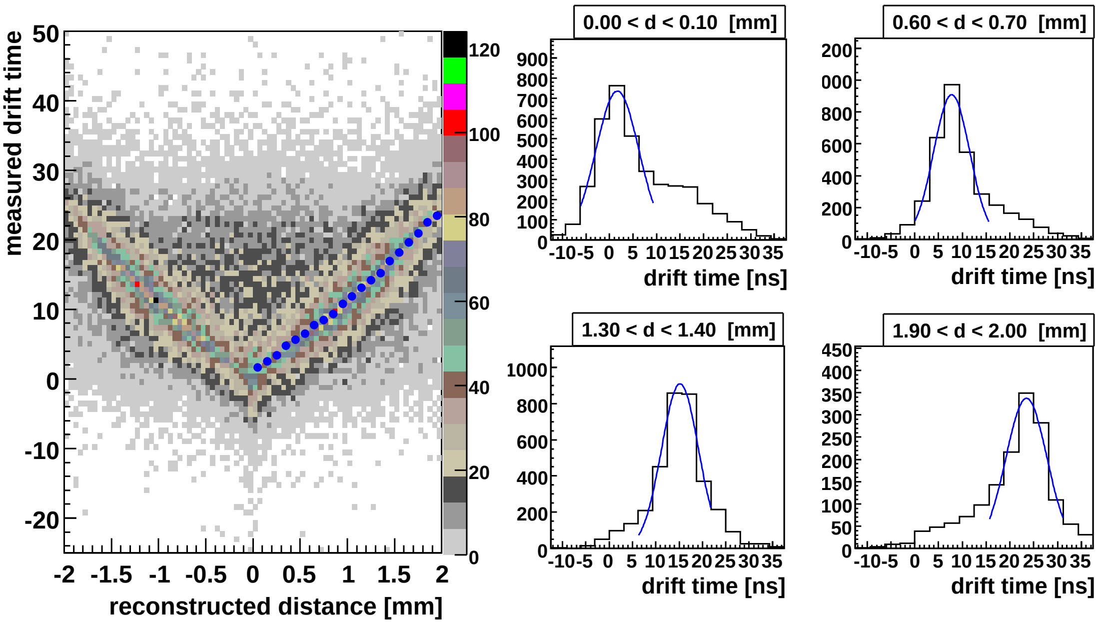

Figure 39. TRT endcap time-to-distance distribution (left) and the drift time distribution in 4 distance intervals (right). The smooth curves in the right figures represent the result of the fit with a Gauss. The blue points in the left plot represent the result of the fitted mean in each distance bin.

for which the leading edge was missing were disregarded.

Following the same iterative procedure as for the barrel, average drift time residuals of reconstructed hits were determined and used to correct for the t_0's. After two iterations, the obtained t_0's became stable, and the obtained residual of hits and reconstructed tracks was about 200 μm, as shown in figure 40.

5.2 Tracking performance

As mentioned in section 3.3.3, the CTB tracking package was the default tracker in the cosmics reconstruction. It was designed for scenarios where tracks do not point to the interaction point, and where the initial alignment and calibration is either very rough or not available at all. For example, it can find tracks in the TRT without using the drift time information at all. The output of the algorithm consists of several different track collections. There are collections for the full setup and for each individual subdetector (SCT, TRT). Furthermore there are separate collections for the upper and lower part of the setup. The results in this section are based on global tracks, i.e., tracks where the hits in the entire setup were used. Figure 41 gives an example of such a global reconstructed track. Figure 42 shows a shower in the upper TRT sector, reconstructed using only the TRT hits in that sector.

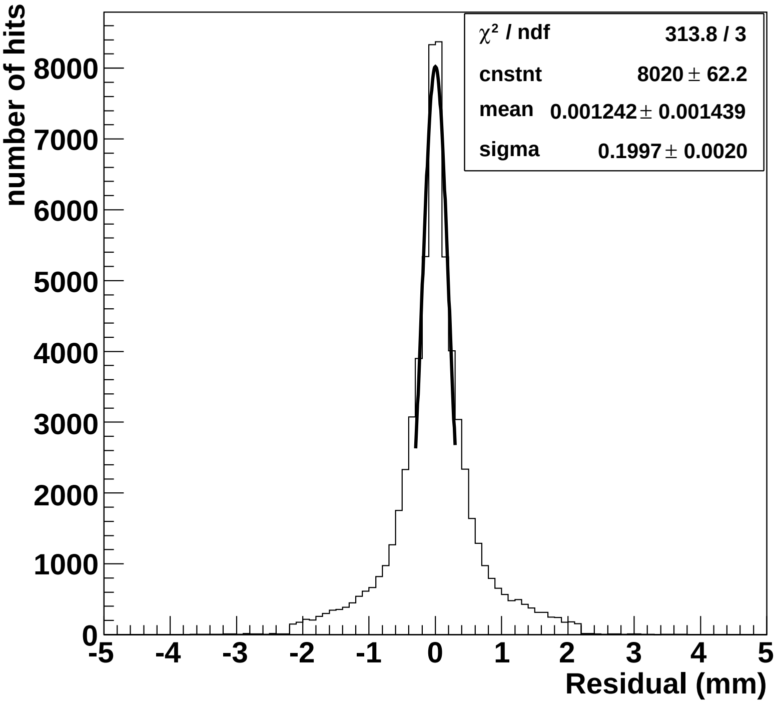

Figure 40. Residual of reconstructed hits obtained after two iterations.

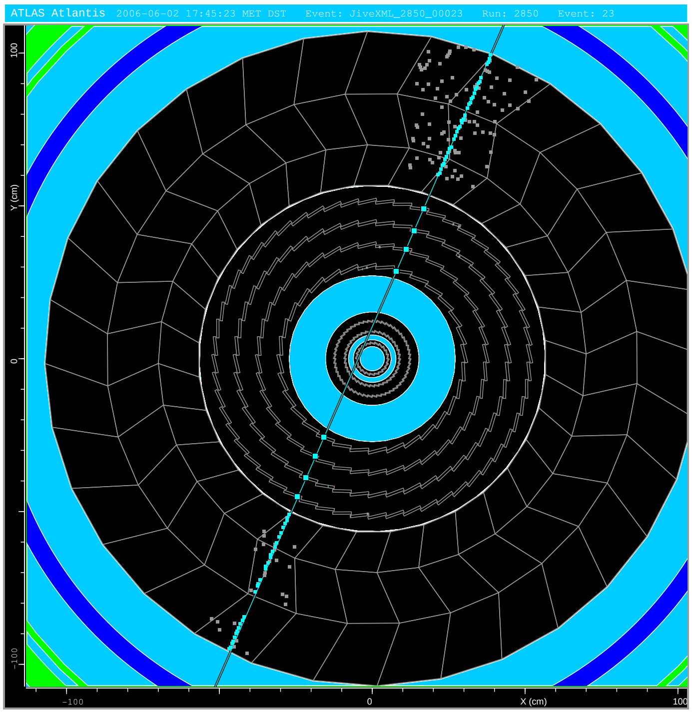

Figure 41. A reconstructed cosmic track with both SCT and TRT hits.

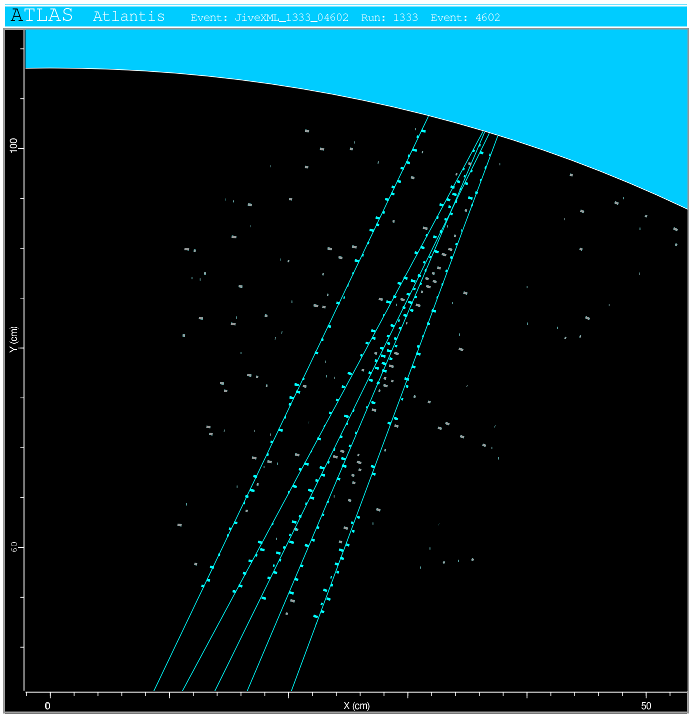

Figure 42. A cosmic shower with several tracks, reconstructed in the TRT.

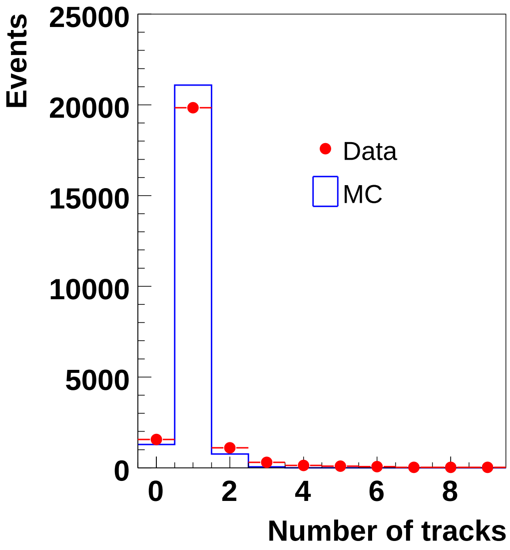

Figure 43. Number of reconstructed tracks, for real and simulated data.

The performance of the pattern recognition was monitored mainly using event displays, and the cuts were tuned accordingly. Figure 43 shows the number of reconstructed tracks for a given run and for a simulated data sample. The muons in the simulated data sample were generated with an energy between 200 MeV and 200 GeV. About 25% of the recorded events do not have any reconstructed tracks. Most of these events are caused by noise in the scintillator trigger setup, and

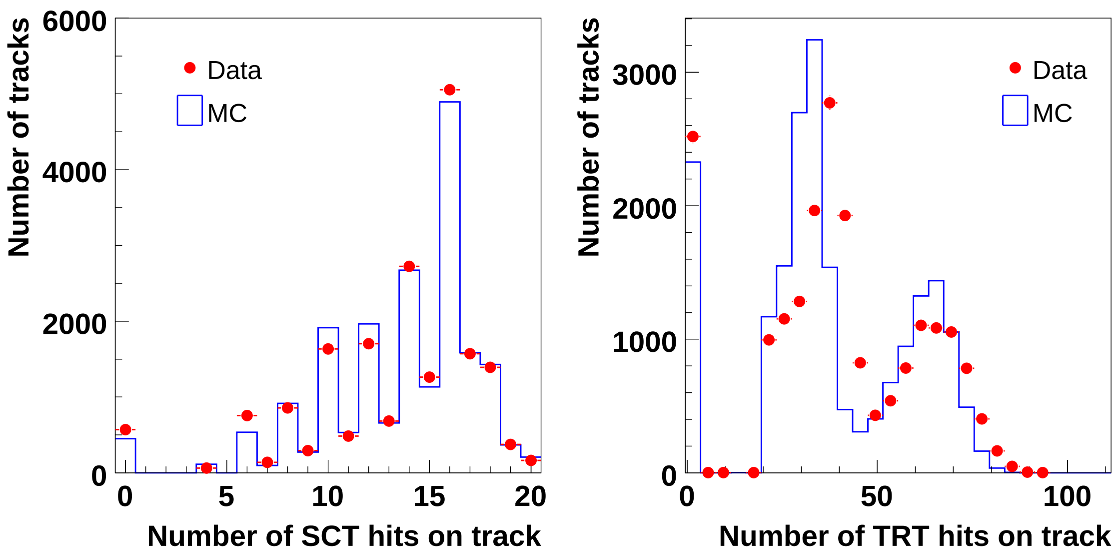

Figure 44. Number of hits on track, for real and simulated data.

can be recognized by an unphysical value of the computed time-of-flight between two scintillator planes. In the current analysis we keep only those events in which the measurement of the time-of-flight gives a physical result. After applying this cut, it can be seen in figure 43 that the simulation and the real data agree fairly well on the number of reconstructed tracks. Inspection with the event display shows that the events without a reconstructed track are either empty, or have a shower that produces so many hits that no reconstruction can be attempted.[13] Cosmic showers were not included in the simulated data, only single muons were considered.

Figure 44 shows the number of SCT and TRT hits on the reconstructed tracks. For this plot the input sample was restricted to events with only one reconstructed track. The number of SCT hits is almost always an even number, because each SCT module has two slides. The distribution of the number of TRT hits has two peaks, because one half of the lower TRT sector was not read out during data taking. Thus, tracks that pass through that region have half as many TRT hits compared to the tracks that pass through the active region. The number of TRT hits on track is slightly higher in real data than in the simulation. Apart from that, the agreement between data and simulation is reasonable.

5.3 SCT performance

The data collected with cosmic rays triggers can be used to check the performance of the SCT detectors in terms of efficiency and resolution. Results are only shown for the barrel data since the number of SCT hits associated with tracks in the endcap setup is too small to allow this kind of study. Tracks reconstructed taking only SCT hits as input are used in order to avoid any effect coming from TRT-SCT misalignments. The SCT alignment corrections obtained with the global χ^2 method are used unless otherwise specified since those led to better results. Comparisons with other alignment corrections and with simulation data are also shown.

---

[13] CTB tracking skips the event if there are more than 120 space points in the SCT, or more than 500 hits in the TRT.

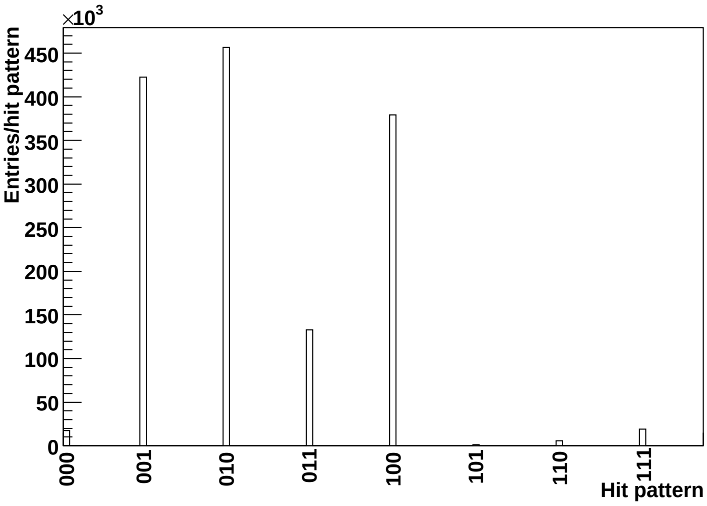

Figure 45. SCT hit pattern.

5.3.1 Timing

The SCT was run in the expanded mode in the cosmic runs, which provides time information for the triggered time bin as well as the preceding and following bins. Figure 45 shows the distribution of the hit patterns for a given run. The 010 hit pattern is dominant, indicating that the trigger is timed well with respect to the SCT modules. The 20 ns shaping time of the ABCD3TA chip will also give rise to hits in adjacent time bins as the pulse duration above threshold can be longer than the 25ns bunch-crossing time window. Hit pattern 001 comes from cases where the hit is registered in the next time bin due to a muon arriving late in the clock cycle. The majority of hits in each event are noise hits, and thus not correlated with the trigger. Notice that there are also some hits with the hit pattern 000. As the readout chip should only output hits from fired channels, this is not a valid hit pattern. Three modules showed this phenomenon in the tests at SR1, on a whole module, on a chip, and on a single channel, respectively.

5.3.2 Efficiency

The efficiency of a given SCT module side was computed using the following method. For each reconstructed track in an event that remains after a quality cut, the algorithm removed any hits located on the SCT barrel layer under investigation, or the i^{th} layer. A track refit was then performed excluding these hits. From the perigee parameters of this new track, an extrapolation to the i^{th} layer was performed to obtain the intersection point or "predicted position" of a hit on a module. If this intersection point was within the sensitive area of the module it was included in the denominator of the efficiency calculation. If a SCT cluster was found to be located within a set distance from the predicted position, an entry was made for the numerator.

Various track quality cuts and fiduciality requirements were made before a hit prediction entered the denominator of the efficiency calculation:

- the track must have 10 or more SCT hits
- the track fit must have a χ^2/ndof ≤ 24

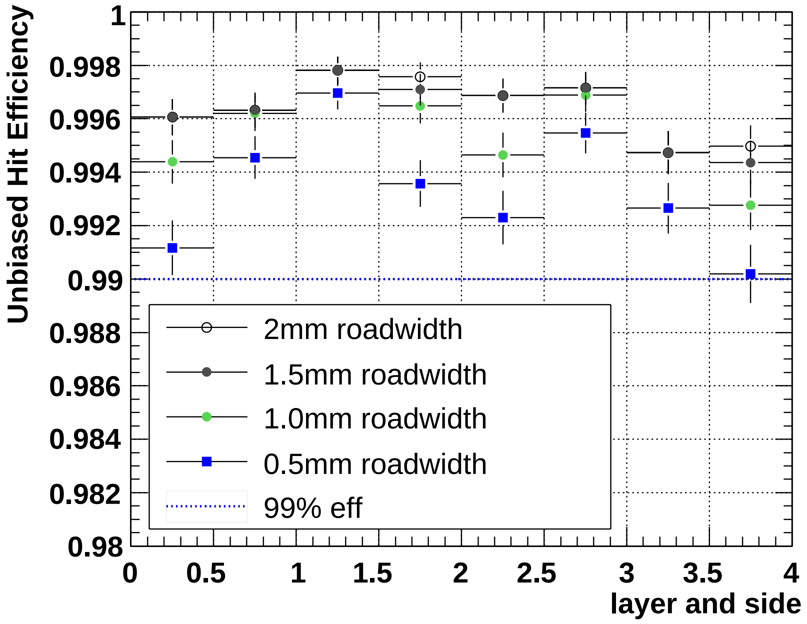

Figure 46. The hit efficiency for the different barrel layers and sides from simulated cosmic data with p_T greater than 200 MeV. Also shown is the specification efficiency of 99% (dashed blue line).

- the track must have an incidence angle on the module of less than 20 degrees in the azimuthal direction
- the track intersection point on the module must be at least 2 mm from the bond gap and 1.5 mm from the edges of the module
- the track intersection point must be at least 1.5 mm from any masked strips or chips

In order for a hit to be entered into the numerator of the efficiency calculation, in addition to the above requirements, a hit must be found within a certain road width around the predicted hit position. By default, and unless specified otherwise, this road width was 2 mm.

In order to choose a proper value for the cut applied to the distance from the predicted track position and the cluster position, the simulation was used. Due to the lack of magnetic field, this distance can be quite large for tracks corresponding to low momentum cosmic rays. Figure 46 shows the average efficiency per SCT layer, for different distance cuts, for all simulated particles. In order to neglect MCS effects, a cut of 2 mm was then chosen to compute efficiencies from real data. The result obtained in this case is shown in figure 47, where after alignment the unbiased hit efficiency in all barrel layers is measured to be within specifications, i.e., greater than 99%.

Since the cosmic trigger is not synchronized with the readout clock, the collected data can also be used to study the dependence of the SCT efficiency with the arrival time of the particle with respect to the readout time. This difference in time was measured and since the SCT is recording the information of three consecutive bunch crossings, the measurement can be done over a time range of 75 ns. Figure 48 shows the SCT efficiency obtained in the barrel section as a function of the arrival time of the particle. The efficiency remains high for a range of 4 ns, compared to

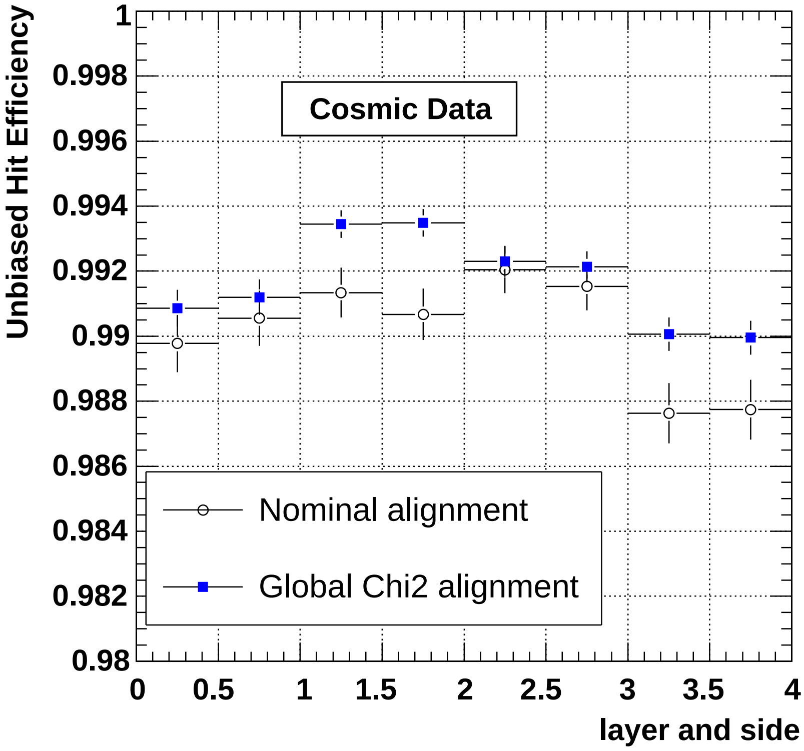

Figure 47. The unbiased hit efficiency measured for the different barrel layers and sides from cosmic data, before and after alignment.

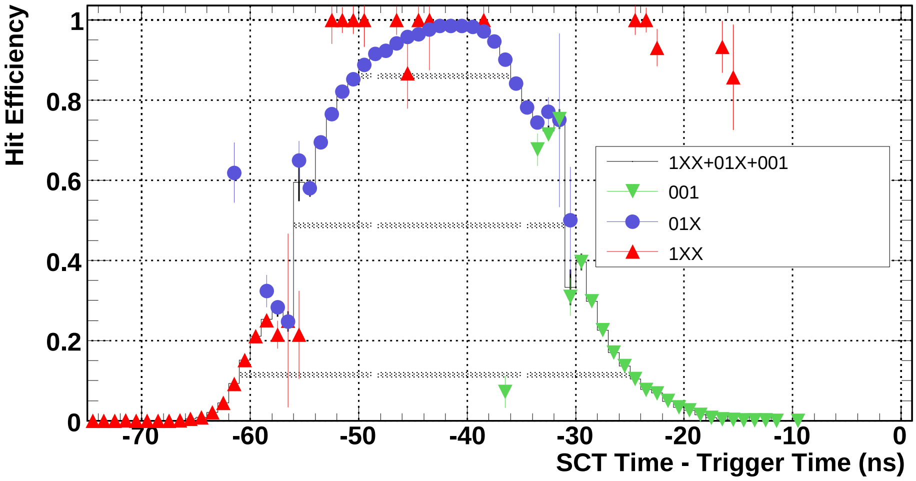

Figure 48. The hit efficiency measured as a function of time between the SCT RDO hit and the scintillator trigger. A road width of 2 mm and global χ^2 alignment corrections are used. The SCT time was 0 ns if the SCT RDO hit pattern was 1XX, 25 ns if 01X, and 50 ns if 001.

approximately 20 ns from the test beam studies [57], due to the time-of-flight of the cosmic rays not being taken into account.

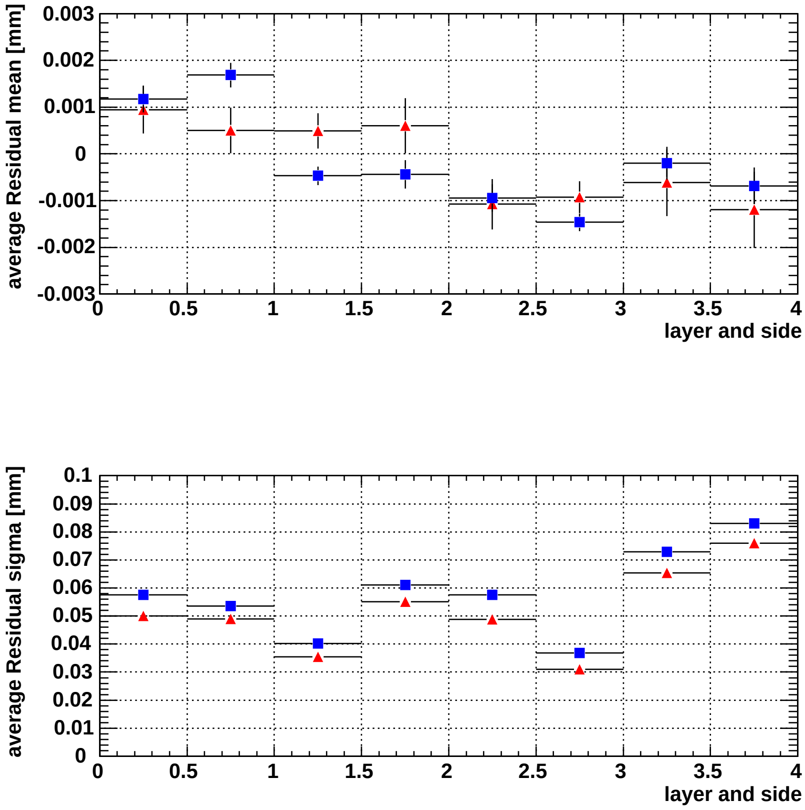

Figure 49. The unbiased residual means for the different layers and sides of the SCT modules for simulation (triangle) and data using global χ^2 alignment (squares). A road width of 2 mm is used.

5.3.3 SCT resolution

The SCT detector resolution can be extracted from the σ of the SCT residual distribution of a given module side after subtracting the track prediction and alignment corrections uncertainties. However, as mentioned above, the track uncertainty is not well estimated for the case of low momentum particles. Figure 49 shows the mean and σ of the unbiased residuals measured for data (using global χ^2 alignment constants) and Monte Carlo simulation. For both the data and simulation the measured residuals are much larger than the expected detector resolution of 23 μm due to the effect of multiple scattering.

Figure 50 shows for simulated data the σ of the SCT residual and pull distribution as a function of the true particle energy. The σ of the residual distribution increases for low energy tracks and for this case the σ of the residual pull distribution is no longer 1 due to the already mentioned wrong track uncertainty estimation. For high momentum tracks, a σ of around 28 μm is obtained. After subtracting in quadrature the track uncertainty contribution (which is estimated to be around 16 μm), a value of 23 μm is obtained in agreement with the intrinsic detector resolution.

In order to determine the detector resolution from the data, the σ of the residual distribution as a function of the unbiased track χ^2 (i.e., removing the contribution to the χ^2 of the hit under evaluation) was measured, for side 1 of modules in layer 2. These modules were chosen to maximise statistics, and minimize track errors. The result obtained is shown in figure 51 for real and

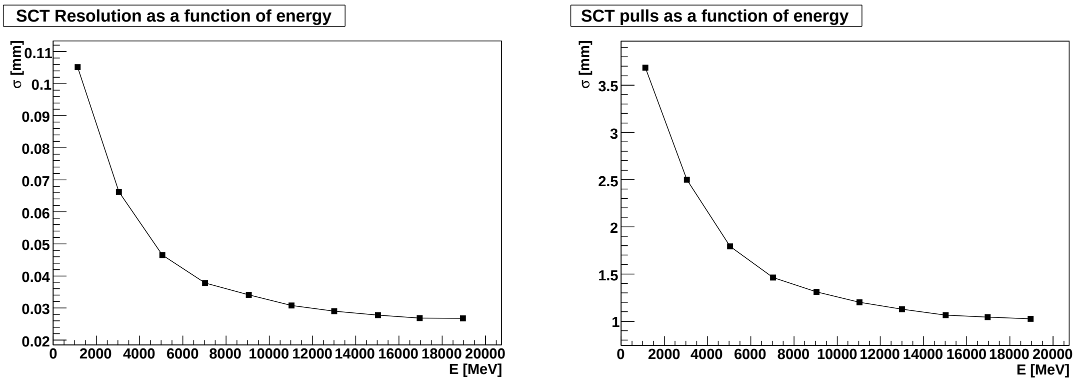

Figure 50. σ of SCT unbiased residuals (left) and pull distributions (right) as a function of true particle energy.

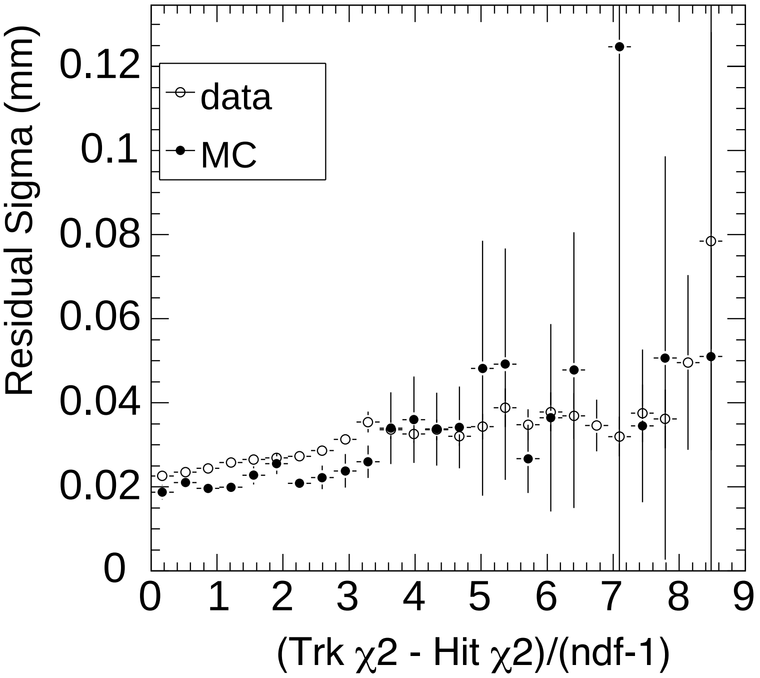

Figure 51. Width of the SCT unbiased residuals, as a function of the unbiased track χ^2 per number of degrees of freedom, for real and simulated cosmic data.

simulated data. When the χ^2 tends to zero, the contribution of low momentum tracks should be negligible. A σ of 24 ± 1 μm (20 ± 2 μm) is obtained for real (simulated) data for tracks with a χ^2 per degrees of freedom of less than 1. For these tracks the contribution to the residual from track uncertainty is negligable. Alignment uncertainties have not been considered resulting in slightly larger residuals in real data than in simulation. The low measured residuals are due to the large number of double clusters present in both data and simulation. Approximately one in three of the clusters in the SCT is a two hit cluster, in both data and simulation. This means that most tracks intercepting the module near the edge of the strip will produce two strip clusters. This effectively reduces the resolution of the one-strip cluster measurement.

5.4 TRT performance

5.4.1 TRT efficiency

The data collected in the SR1 test were also used to study the efficiency of the TRT straw tubes. Because of the limited statistics in the endcap, this study was only performed for the barrel.

It is important to note that, given the lack of track momentum information, an accurate measurement of the straw efficiency with cosmic data is difficult. Multiple scattering effects cannot be accounted for and hence there is a high uncertainty on the relative position of the passing particle with respect to the straw tubes. On the other hand, knowing whether a particle passes through the active region of a straw or not, is essential in determining its efficiency.

For this reason particular care was devoted to selection of tracks for this study in order to reduce the uncertainties resulting from multiple scattering. The detector geometry was corrected using the procedure described in section 5.1.5 for simultaneously aligning the SCT and TRT.

The track selection proceeded as follows:

- Full SCT+TRT tracks were reconstructed and, to suppress events generated by cosmic showers, only events with a single track were selected,
- SCT track segments from the top and bottom sectors were combined and the resulting SCT tracks were required to be of high quality ($\chi^2/\mathrm{ndof} < 5$),
- SCT tracks were extrapolated to the TRT. The distance between the extrapolated track intersection at the last straw layer (corresponding to the maximum lever arm) and the closest hit in the same straw layer was required to be less than 0.3 mm.

Monte Carlo studies have shown that this selection procedure reduces the presence of tracks at the low end of the momentum spectrum. These tracks are most affected by multiple scattering. Most importantly, no requirements were made on the quality of the TRT segments themselves, in particular no cuts were applied to the χ^2 of the TRT (or SCT+TRT) tracks. In this way the bias on the efficiency induced by the track selection is kept to a minimum for layers other than the last straw layer.

For each straw the efficiency was defined as the ratio between the number of "expected" hits (i.e., the number of tracks passing closer than a certain distance R to the straw wire) and the total number of recorded hits. In figure 52 the distribution of the straw efficiencies (calculated for $R = 2$ mm, the straw radius) is shown. To reduce statistical fluctuations only straws with at least 40 expected hits were considered. The mean of the efficiency distribution is approximately 93%.

Due to the statisical nature of the ionization process, the efficiency of a straw tube depends on the path length of the track inside the straw. Straws with a track passing close to the edge are expected to be less efficient than straws having tracks passing well inside their volume. In figure 53 the efficiency profile as a function of the track distance R to the wire is shown. The efficiency is very close to one if the tracks pass well inside the straw ($R \lesssim 1.7$ mm) while it drops for tracks close to the straw boundary. The shape of the efficiency profile for distances close to the tube boundary is determined by properties of the ionization gas and by the track extrapolation uncertainties. A non-zero efficiency for R significantly outside the straw radius is almost exclusively due to noise.

2008 JINST 3 P08003

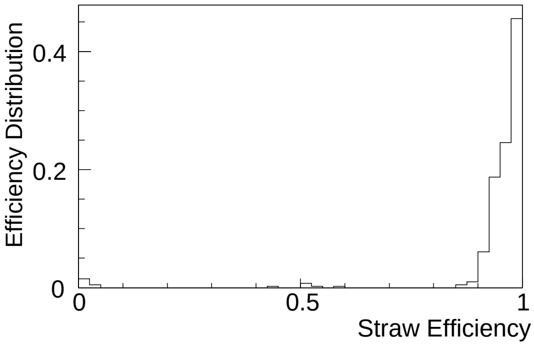

Figure 52. Efficiency distribution for straws having at least 40 "expected" hits for a distance $R < 2$ mm.

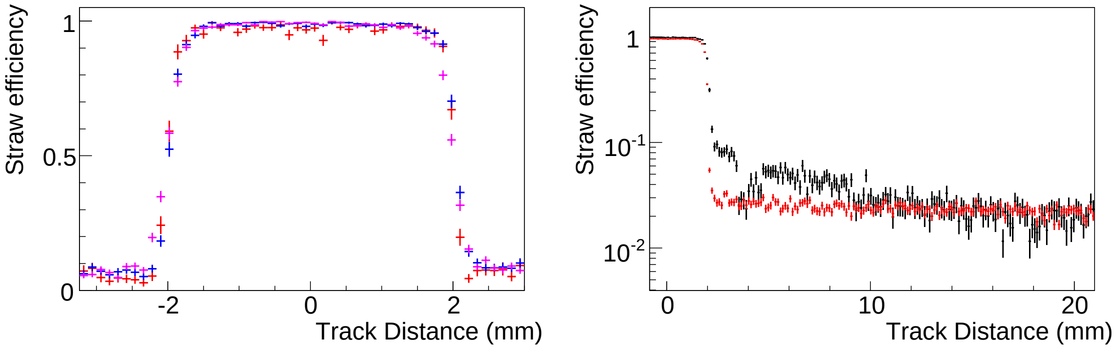

Figure 53. Left: Straw efficiency profile as a function of the track-wire distance R in real data. The different distributions denote the TRT module types (inner, middle, and outer). Right: Same distribution as in the left plot, shown on a logarithmic scale and for extended R values. Red is simulation, black is real data.

A random noise throughout the detector is expected to contribute to the efficiency independent of the track distance R to the straw. However, in real data an R-dependent noise is observed. As is clear from the right plot in figure 53, the efficiency for straws with a track outside their physical volume ($R \gtrsim 2\,\text{mm}$) but close to the straw ($R \lesssim 10\,\text{mm}$) is higher than that expected from random noise. This can be attributed to channel cross-talk, where a high signal amplitude registered in one straw induces a noise signal on neighboring straws, in particular to straws connected to the same readout chip or HV pad. This effect has been already observed in TRT prototypes in test beam data [59]. The peculiar structure observed in real data (efficiency dip at $R \sim 3.7\,\text{mm}$) is generated by the arrangement of the straws inside the TRT modules and by the straw geometric grouping of readout chips/HV pad. As can be noticed from the efficiency profile obtained with Monte Carlo events, such cross-talk effects are not included in the current version of the TRT simulation. However the simulation correctly reproduces the magnitude of the random noise, which from this study is shown to be of the order of 2% (in agreement with that quoted in section 4.2).

5.4.2 TRT resolution

As in the case of the SCT, the hit resolution of the TRT can be extracted by subtracting the track uncertainty from the width of the residual distribution, in quadrature. Due to the large number of

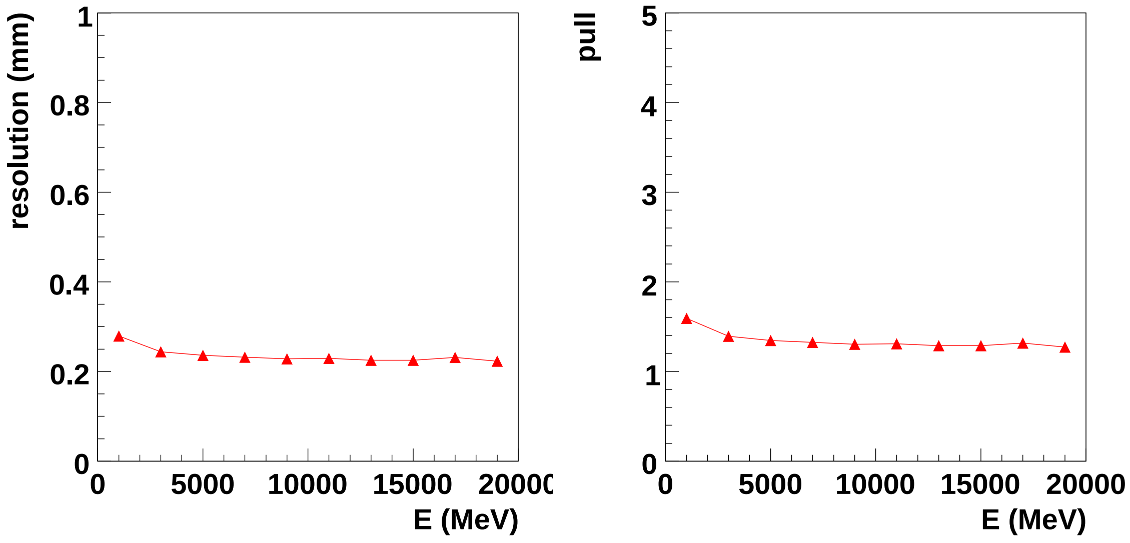

Figure 54. Width of the TRT unbiased residuals and pulls, as a function of energy, for simulated tracks.

hits on a TRT track, the calculated track uncertainty is fairly small compared to the hit resolution. The contribution from multiple scattering to the residuals is also relatively small, since the TRT hit resolution is a factor 10 higher than the SCT hit resolution. Thus, the width of the residual distribution is a good measure for the TRT hit resolution.

Figure 54 shows the widths of the residual and pull distributions as a function of energy, for simulated tracks in the upper half of the TRT. The plots are nearly flat except at the lowest energy bin, showing that the effect of multiple scattering is indeed limited. It should be noted though that the tails increase significantly at low momentum.[14] The hit resolution assumed in the track fit is 170 microns, which explains why the pulls are always larger than 1 since the actual hit resolution is close to 200 microns.

Figure 55 shows the residual distribution for real and simulated tracks in the upper half of the TRT, and the width of the residual distributions per module type (inner, middle and outer). For the distributions the input data sample was restricted to events where the SCT track has a reduced χ^2 smaller than 2, in order to remove low energy tracks from the sample. The small dependence of the residual width on the module type is due to the uncertainty of the predicted track position, which is smallest near the middle of the track. It is seen that the TRT performance is slightly better in real data than in the simulation. It should be remembered that the TRT resolution shown above was obtained with an Argon-based gas mixture. In ATLAS, where a Xenon-based gas mixture will be used, the expected resolution is of the order of 130 microns [46].

6. Conclusions

The combined operation of the ATLAS Semiconductor Tracker (SCT) and Transition Radiation Tracker prior to their installation in ATLAS were investigated. This test concluded the integration

---

[14] Tails are not taken into account here, only the core of the distributions is fitted.

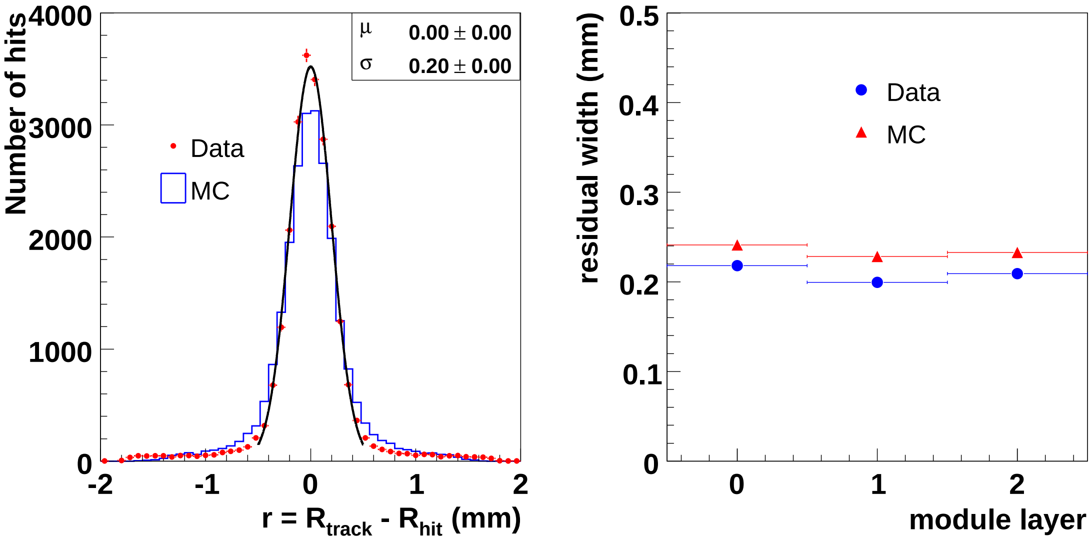

Figure 55. Comparison of the real and simulated TRT unbiased hit residuals.

process of these two tracking subdetectors and provided the first opportunity to test the combined tracking of SCT and TRT with cosmic rays in a large test stand at the surface integration facility. The four months combined operation of the SCT and TRT allowed the commissioning and thorough testing of the hardware for detector supply, control, and readout systems for the SCT and TRT in a final detector configuration. The experience of this operation led to numerous improvements in the detector control, calibration, and physics readout software.

The noise performance of SCT and TRT in the final detector configuration was tested. The tests showed on the SCT a noise occupancy of 4.7×10^{-5} and equivalent noise charge of about 1650 electrons for warm operation with hybrid temperatures approximately 25 °C above their final cold operation temperature in the experiment. These results are consistent with previous assembly test results on single barrels or disks and individual modules during production, showing that the simultaneous operation of four barrels (nine disks) did not lead to a noise increase. The noise of the TRT barrel and endcap was investigated through a series of test runs with the SCT off and with the SCT operated synchronously with the TRT. The tests showed no increase of noise on the TRT through a series of tests with SCT in on and off states. The frontend electronics noise of SCT and TRT during the active readout cycle of the respective other subdetector was tested and the absence of cross-talk between SCT and TRT in the combined test was confirmed.

During the combined tests of barrel and endcap large samples of cosmic ray events were collected. Those events were used to commission the online monitoring software and offline track reconstruction software chain, which will be used for LHC collisions. The online monitoring was operated at the event filter level as well as standalone. Reconstructing the cosmic tracks in SCT and TRT, individually and combined, allowed the successful testing of raw data processing, track reconstruction, and detector alignment methods with real data for the first time. This has led to the extraction of first preliminary results for basic tracking performance parameters. A single plane efficiency of 99% and spatial resolution matching expectations from simulation for the SCT were found. The TRT drift time resolution of $\approx$200 μm agrees with the expected value for an argon-based gas mixture. Similarly, the measured straw efficiency is in agreement with expectations.

Acknowledgments

We are greatly indebted to all the technical staff who worked on the integration and testing of the Inner Detector from the ATLAS SCT and TRT Institutes. We acknowledge the support of the funding authorities of the collaborating institutes including the Spanish National Programme for Particle Physics; the Research Council of Norway; the Science and Technology Facilities Council of the United Kingdom; the Polish Ministry of Education and Science; the German Ministry of Science; the Swiss National Science Foundation; the State Secretariat for Education and Research and the Canton of Geneva; the Slovenian Research Agency and the Ministry of Higher Education, Science and Technology of the Republic of Slovenia; the Ministry of Education, Culture, Sports, Science and Technology of Japan; the Japan Society for the Promotion of Science; the Civil Research and Development Foundation and the Office of High Energy Physics of the United States Department of Energy; the United States National Science Foundation; the Australian Research Council (ARC) and Department of Education, Science and Training (DEST); the Dutch Foundation for Fundamental Research on Matter (FOM) and the Netherlands Organisation for Scientific Research (NWO); the Ministry of Education, Youth and Sports of the Czech Republic; the National Science Council, Taiwan; the Swedish Research Council; the European Union (DGXII), the International Science Foundation; the Knut and Alice Wallenberg Foundation; the International Science and Technology Centre; the Natural Science and Engineering Research Council of Canada; the Ministry of Education and Science of the Russian Federation; the Academy of Science of the Russian Federation; the International Association for the Promotion of Cooperation with Scientists from the new Independent States of the former Soviet Union; the Turkish Atomic Energy Authority.

References

[1] ATLAS collaboration, *ATLAS: technical proposal for a general-purpose pp experiment at the Large Hadron Collider at CERN*, CERN-LHCC-94-43.

[2] ATLAS collaboration, *ATLAS Inner Detector Technical Design Report. Volume 1 and 2*, CERN-LHCC-97-016, CERN-LHCC-97-017.

[3] A. Abdesselam et al., *The barrel modules of the ATLAS semiconductor tracker*, *Nucl. Instrum. Meth.* **A 568** (2006) 642.

[4] A. Abdesselam et al., *The ATLAS semiconductor tracker end-cap module*, *Nucl. Instrum. Meth.* **A 575** (2007) 353.

[5] A. Ahmad et al., *The Silicon microstrip sensors of the ATLAS semiconductor tracker*, *Nucl. Instrum. Meth.* **A 578** (2007) 98.

[6] F. Campabadal et al., *Design and performance of the ABCD3TA ASIC for readout of silicon strip detectors in the ATLAS semiconductor tracker*, *Nucl. Instrum. Meth.* **A 552** (2005) 292.

[7] E. Abat et al., *The ATLAS TRT Barrel Detector*, 2008 *JINST* **3** P02014.

[8] E. Abat et al., *The End Caps of the ATLAS Transition Radiation Tracker*, in preparation.

[9] E. Abat et al., *The ATLAS TRT Electronic*, 2008 *JINST* **3** P06007.

[10] S. Terada et al., *Design and development of a work robot to place ATLAS SCT modules onto barrel cylinders*, *Nucl. Instrum. Meth.* **A541** (2005) 144.

[11] G. Viehhauser, *Macro-assembly of the ATLAS Barrel SCT*, *IEEE Nucl. Sci. Symp. Conf. Rec.* **2** (2004) 1188.

[12] A. Abdesselam et al., *The Detector Control System of the ATLAS SemiConductor Tracker during Macro-Assembly and Integration*, 2008 *JINST* **3** P02007.

[13] CAN in Automation (CiA), http://www.can-cia.de/.

[14] PVSS-II, ETM Austria, http://www.pvss.com/.

[15] http://dim.web.cern.ch/dim/.

[16] P.A. Coe, D.F. Howell and R.B. Nickerson, *Frequency scanning interferometry in ATLAS: remote, multiple, simultaneous and precise distance measurements in a hostile environment*, *Meas. Sci. Technol.* **15** (2004) 2175;
S.M. Gibson, *The ATLAS SCT alignment system and a comparative study of misalignment at CDF and ATLAS*, D.Phil. Thesis, Oxford (2004), CERN-THESIS-2007-080.

[17] A. Abdesselam et al., *The Integration and Engineering of the ATLAS Semiconductor Tracker Barrel*, submitted to JINST.

[18] A. Sfyrla et al., *The Detector Control System for the ATLAS Semiconductor Tracker Assembly Phase*, *IEEE Trans. Nucl. Sci.* **52** (2005) 938.

[19] http://itcobe.web.cern.ch/itcobe/Projects/Framework/.

[20] ATLAS Embedded Local Monitor Board, http://www.nikhef.nl/pub/departments/ct/po/html/ELMB128/ELMB22.pdf.

[21] A.J. Barr et al., *The Data Acquisition and Calibration System for the ATLAS Semiconductor Tracker*, 2008 *JINST* **3** P01003.

[22] A. Abdesselam et al., *Engineering for the ATLAS SemiConductor Tracker (SCT) End-cap*, 2008 *JINST* **3** P05002.

[23] ATLAS collaboration, *ATLAS high-level trigger, data-acquisition and controls : Technical Design Report*, CERN-LHCC-2003-022.

[24] B.C. LeGeyt and J. Valls, *XTRTUsersGuide*, http://valls.web.cern.ch/valls/ATLAS_TRT/Files%20TRT/xtrt.htm

[25] T. Vickey, *A read-out driver for silicon detectors in ATLAS*, *Proceedings of 12th Workshop on Electronics for LHC and Future Experiments, LECC2006*, Valencia Spain (2006), http://cdsweb.cern.ch/record/1027436.

[26] Amplifier-Shaper-Discriminator-BLR Integrated Circuit, http://www.hep.upenn.edu/atlas/asdblr/.

[27] F. Anghinolfi et al., *DSM-DTMROC: Project Specification*, http://www.hep.upenn.edu/atlas/dtmroc/dsm_dtmroc/DSM_DTMROC_Specs_v1_12.pdf.

[28] ATLAS collaboration, *ATLAS computing: Technical Design Report*, ATLAS-TDR-017, CERN-LHCC-2005-022.

[29] S. Agostinelli et al., *GEANT4 — a simulation toolkit*, *Nucl. Instrum. Meth.* **A 506** (2003) 250.

[30] J. Allison et al., *GEANT4 developments and applications*, *IEEE Trans. Nucl. Sci.* **53** (2006) 270.

[31] O.C. Allkofer et al., *The absolute cosmic ray muon spectrum at sea level*, *Phys. Lett.* **B 36** (1971) 425.

[32] A. Dar, *Atmospheric neutrinos, astrophysical neutrinos and proton decay experiments*, *Phys. Rev. Lett.* **51** (1983) 227.

[33] T. Cornelissen, *Track fitting in the ATLAS experiment*, PhD Thesis, University of Amsterdam (2006), CERN-THESIS-2006-072.

[34] T.H. Kittelmann and E.B. Klinkby, *A Study of TRT Noise in 2004 Test Beam Data*, ATL-INDET-PUB-2008-010;
T.H. Kittelmann, *Modelling of Noise and Straw to Straw Variations in the ATLAS Transition Radiation Tracker*, ATL-INDET-PUB-2008-009.

[35] F. Åkesson et al., *ATLAS Tracking Event Data Model*, ATL-SOFT-PUB-2006-004.

[36] F. Åkesson et al., *ATLAS Inner Detector Event Data Model*, ATL-SOFT-PUB-2007-006.

[37] ATLAS Event Display Atlantis, http://www.hep.ucl.ac.uk/atlas/atlantis/.

[38] E.T. Ray, *Learning XML*, O'Reilly (2003) [ISBN: 0-596-00420-6].

[39] D. Tidwell, *XSLT*, O'Reilly (2001) [ISBN: 0-596-00053-7].

[40] S. Kolos et al., *Online Monitoring software framework in the ATLAS experiment*, *Proceeding of Conference for Computing in High-Energy and Nuclear Physics (CHEP2003)*, La Jolla, California U.S.A. (2003), ATL-DAQ-2003-005.

[41] W. Vandelli et al., *Stategies and Tools for ATLAS on-line monitoring*, *Proceeding of Conference for Computing in High-Energy and Nuclear Physics (CHEP2003)*, Mumbai, India (2006).

[42] R. Brun and F. Rademaker, *ROOT — An Object Oriented Data Analysis Framework*, *Nucl. Instum. Meth.* **A 389** (1997) 81, also in *Proceedings AIHENP'96 Workshop*, Lausanne Switzerland (1996); see also http://root.cern.ch/.

[43] F.P. Zema et al., *The GNAM Monitoring system and the OHP histogram presenter for ATLAS*, 14th *IEEE-NPS Real Time Conference 2005*, Stockholm, Sweden (2005).

[44] Trolltech ASA Sandakerveien 116, Oslo, Norway, http://trolltech.com/.

[45] M. White, *Searching for Supersymmetry with the ATLAS Detector*, PhD Thesis, University of Cambridge (2006), CERN-THESIS-2008-052.

[46] E. Abat et al., *The ATLAS Transition Radiation Tracker (TRT) proportional drift tube: design and performance*, 2008 *JINST* **3** P02013.

[47] P.W. Phillips, *Functional testing of the ATLAS SCT barrels*, *Nucl. Instrum. Meth.* **A 570** (2007) 230.

[48] S.O. Rice, *Mathematical Analysis of Random Noise*, *Bell System Technical Journal* **23** (1944) 282.

[49] ATLAS SCT collaboration, V.A. Mitsou, *Production performance of the ATLAS semiconductor tracker readout system*, *IEEE Trans. Nucl. Sci.* **53** (2006) 729.

[50] S. Blusk et al., *Proceedings of the first LHC Detector Alignment Workshop*, Geneva Switzerland (2006), CERN-2007-004.

[51] F. Heinemann, *Robust Track Based Alignment of the ATLAS Silicon Detectors and Assessing Parton Distribution Uncertainties in Drell-Yann Processes*, D.Phil. Thesis, University of Oxford (2007), CERN-THESIS-2007-075.

[52] P. Bruckman et al., *Global χ^2 approach to the Alignment of the ATLAS Silicon Tracking Detectors*, ATL-INDET-PUB-2005-002.

[53] A. Bocci and W. Hulsbergen, *TRT Alignment For SR1 Cosmics and Beyond*, ATL-INDET-PUB-2007-009;
T. Golling, , ATL-INDET-PUB-2006-001.

[54] O.K. Øye, *Preparing the ATLAS experiment, SemiConductor Tracker commissioning and simulation studies of SUSY models*, Thesis, University of Bergen (2006).

[55] D. Mergelkuhl, A. Wiart, *ATLAS - SCT Barrel Detector Photogrammetric Measurement of SCT Barrel, FSI and Pixel JIG*, EDMS document ATL-IS-UR-0004 id 681215 (2005).

[56] E. Dobson, S.M. Gibson, F. Heinemann and M. Karagoz Unel, *Study of a twisted ATLAS SCT Barrel deformation as revealed by a photogrammetry survey*, ATL-INDET-PUB-2008-011.

[57] F. Campabadal et al., *Beam tests of ATLAS SCT silicon strip detector modules*, *Nucl. Instrum. Meth.* **A 538** (2005) 384.

[58] H. Pernegger, *Integration and test of the ATLAS semiconductor tracker*, *Nucl. Instrum. Meth.* **A 572** (2007) 108.

[59] ATLAS TRT collaboration, T. Akesson et al., *ATLAS Transition Radiation Tracker test-beam results*, *Nucl. Instrum. Meth.* **A 522** (2004) 50.